MNRAS **000**, 000–000 (0000) Preprint 1 February 2018 Compiled using MNRAS LATEX style file v3.0

Resolving the Disc-Halo Degeneracy I: A Look at NGC 628

S. Aniyan[1,2]★, K. C. Freeman[1], M. Arnaboldi[2], O. E. Gerhard[3], L. Coccato[2], M. Fabricius[3], K. Kuijken[4], M. Merrifield[5] & A. A. Ponomareva[1,6]

[1]*Research School of Astronomy & Astrophysics, Australian National University, Canberra, ACT 2611, Australia*
[2]*European Southern Observatory, Karl-Schwarzschild-Strasse 2, D-85748 Garching, Germany*
[3]*Max-Planck-Institut für Extraterrestrische Physik, Giessenbachstrasse, 85741 Garching, Germany*
[4]*Leiden Observatory, Leiden University, Niels Bohrweg 2, NL-2333 CA Leiden, the Netherlands*
[5]*School of Physics and Astronomy, University of Nottingham, University Park, Nottingham, NG7 2RD, UK*
[6]*Kapteyn Astronomical Institute, University of Groningen, Postbus 800, NL-9700 AV Groningen, The Netherlands*

1 February 2018

ABSTRACT

The decomposition of the rotation curve of galaxies into contribution from the disc and dark halo remains uncertain and depends on the adopted mass to light ratio (M/L) of the disc. Given the vertical velocity dispersion of stars and disc scale height, the disc surface mass density and hence the M/L can be estimated. We address a conceptual problem with previous measurements of the scale height and dispersion. When using this method, the dispersion and scale height must refer to the same population of stars. The scale height is obtained from near-IR studies of edge-on galaxies and is weighted towards older kinematically hotter stars, whereas the dispersion obtained from integrated light in the optical bands includes stars of all ages. We aim to extract the dispersion for the hotter stars, so that it can then be used with the correct scale height to obtain the disc surface mass density. We use a sample of planetary nebulae (PNe) as dynamical tracers in the face-on galaxy NGC 628. We extract two different dispersions from its velocity histogram – representing the older and younger PNe. We also present complementary stellar absorption spectra in the inner regions of this galaxy and use a direct pixel fitting technique to extract the two components. Our analysis concludes that previous studies, which do not take account of the young disc, underestimate the disc surface mass density by a factor of ~2. This is sufficient to make a maximal disc for NGC 628 appear like a submaximal disc.

Key words: Galaxies: kinematics and dynamics – Galaxies: evolution – Galaxies: spiral – dark matter

1 INTRODUCTION

The 21 cm rotation curve of galaxies flatten at large radii, indicating the presence of dark matter in these galaxies. The rotation curves can be decomposed into contributions from the stellar and gas discs, plus the dark halo, and in principle allow us to estimate the parameters of the dark halo. The decomposition of these rotation curves into contributions from the disc and the dark halo depends strongly, however, on the adopted mass-to-light ratio (M/L) of the stellar disc (Van Albada et al. 1985). Choosing different M/L can result in a maximal disc or a submaximal disc, with very different dark halo contributions, both of which can fit the observed rotation curves equally well. Thus, the M/L is critical to obtain the parameters of the dark haloes of disc galaxies, such as their scale densities and scale lengths. These halo parameters are cosmologically significant, because the densities and scale radii of dark haloes follow well-defined scaling laws and can therefore be used to measure the redshift of assembly of haloes of different masses (Macciò et al. 2013; Kormendy & Freeman 2016).

Several techniques have been used to break the disc-halo degeneracy but they all present challenges. One such technique is the adoption of the maximum-disc hypothesis (Van Albada et al. 1985). This method involves adopting a M/L such that there is maximum contribution from the disc without exceeding the observed rotation curve. However, there is still argument about whether this hypothesis is correct. Another technique used to estimate the M/L is from stellar population synthesis models. However, this method involves several significant assumptions about the star formation and chemical enrichment histories and the initial stellar mass function, and it needs an accurate account of late phases of stellar evolution (Maraston

★ Email: suryashree.aniyan@anu.edu.au

2005; Conroy et al. 2009). The M/L obtained using these methods (in the K-band) have typical uncertainties of ~ 0.3 dex (see for e.g. Conroy 2013; Courteau et al. 2014), enough to allow a maximal or sub-maximal solution in most mass modeling decompositions.

One of the more direct methods to break the disc-halo degeneracy uses the vertical velocity dispersion of tracers in the discs to measure the surface mass density of the disc (e.g. Van der Kruit & Freeman 1984, Bottema et al. 1987, Herrmann et al. 2008, Bershady et al. 2010a). Using the 1D Jeans equation in the vertical direction, the vertical luminosity-weighted velocity dispersion σ_z (integrated vertically through the disc) and the vertical exponential disc scale height h_z together give the surface mass density Σ of the disc via the relation:

$$\Sigma = f\sigma_z^2/Gh_z \quad (1)$$

where G is the gravitational constant and f is a geometric factor, known as the vertical structure constant, that depends weakly on the adopted vertical structure of the disc. For example, for an isothermal disc with $\rho(z) \propto \mathrm{sech}^2(z/2h_z)$, the factor $f = f_{iso} = 1/2\pi$, whereas $f = f_{exp} = 2/3\pi$ for a vertically exponential disc with $\rho(z) \propto \exp(-z/h_z)$ (Van der Kruit & Freeman 2011). Van der Kruit (1988) advocated for an intermediate case where $\rho(z) \propto \mathrm{sech}(z/h_z)$, for which $f = f_{int} = 2/\pi^2$. Thus, having adopted a vertical structure for the stellar disc, we need two observables to estimate the surface mass density of the disc: the scale height and the vertical velocity dispersion. The surface brightness of the disc and the surface mass density (Σ from equation 1) together give the M/L of the disc, which is needed to break the disc-halo degeneracy.

The scale height h_z of the thin disc is typically about 300 pc (see for e.g. Gilmore & Reid 1983), but cannot be measured directly for face-on galaxies. Studies of edge-on disc galaxies show a correlation between the scale height and indicators of the galaxies' mass scale, such as the absolute magnitude and the circular velocity. Yoachim & Dalcanton (2006) show the correlation of the scale heights of the thin and thick disc with circular velocity of edge-on disc galaxies using R-band surface photometry. Similarly, Kregel et al. (2005) used I-band surface photometry of edge-on disc galaxies to derive correlations between the scale height and intrinsic properties of the galaxy such as its central surface brightness. We can, therefore, estimate the scale height statistically using other known features of the galaxy.

The other parameter, the vertical stellar velocity dispersion σ_z of the disc, can be measured in relatively face-on galaxies from:

- spectra of the integrated light of the disc.
- the velocity distribution of a population of stellar tracers (such as planetary nebulae).

Using the integrated light to measure σ_z is challenging because high resolution spectra of low surface brightness discs are required to measure the small velocity dispersions (e.g. for the old disc near the sun, Aniyan et al. (2016) find $\sigma_z \sim 20$ km s^{-1}). Another challenge comes from the fact that near face-on galaxies are rare, so dynamical analyses are required in galaxies with larger inclinations to extract the vertical component σ_z from the observed line-of-sight velocity dispersion (LOSVD) σ_{LOS}. NGC 628 is one of the few galaxies (the only one in our sample), which is so nearly face-on that the in-plane components of the stellar motion makes a negligible contribution to the LOSVD. Van der Kruit & Freeman (1984), Bottema et al. (1987) and Bershady et al. (2010a) have used this method and find that the disc M/L is relatively low and the discs are submaximal.

The DiskMass Survey (DMS; Bershady et al. 2010a) used integral-field spectroscopy to measure the stellar kinematics of the discs of near face-on galaxies observed with the SparsePak and PPak instruments. The DMS measured stellar kinematics for 46 galaxies and calculated their vertical velocity dispersions from the absorption line spectra of the integrated disc light. They then combined these dispersions with the estimated scale heights to calculate the surface mass density of the disc (using equation 1). Bershady et al. (2011) find that the dynamical stellar M/L obtained from the surface mass density is about 3 times lower than the M/L from the maximum disc hypothesis and conclude that discs are submaximal.

Herrmann et al. (2008) and Herrmann & Ciardullo (2009a,b) observed 5 near-face-on spirals (including our target galaxy NGC 628) using PNe as tracers. The advantage of using PNe as tracers over integrated light work is that it enables one to extend the analysis to the outer regions of the disc. Herrmann & Ciardullo (2009b) find that 4 of their discs appear to have a constant M/L out to ~ 3 optical scale lengths. Beyond this radius, σ_z flattens out and remains constant with radius. Herrmann & Ciardullo (2009b) suggest that this behaviour could be due to an increase in the disc mass-to-light ratio, an increase in the contribution of the thick disc, and/or heating of the thin disc by halo substructure. They also find a correlation between disc maximality and whether the galaxy is an early or late type spiral. They note that the later-type (Scd) systems appear to be clearly submaximal, with surface mass densities less than a quarter of that needed to reproduce the central rotation curves, whereas in earlier (Sc) galaxies (like NGC 628), this discrepancy is smaller, but still present; only the early-type Sab system M94 has evidence for a maximal disc (Herrmann & Ciardullo 2009b).

An important conceptual problem has, however, been overlooked in the earlier studies described above. Equation 1 comes from the vertical Jeans equation for an equilibrium disc. It is therefore essential that the vertical disc scale height h_z and the vertical velocity dispersion σ_z should refer to the same population of stars.

The red and near-infrared measurements of the scale heights of edge-on disc galaxies are dominated by the red giants of the older, kinematically hotter population. The dust layer near the Galactic plane further weights the determination of the scale height to the older kinematically hotter population: e.g. De Grijs et al. (1997). On the other hand, the velocity dispersion σ_z is usually measured from integrated light spectra near the Mg b lines ($\sim 5150 - 5200$ Å), since this region has many absorption lines and the sky is relatively dark. The CaII triplet region at ~ 8500 Å is also a potential region of interest with several strong absorption features. However, there are many bright sky emission lines in this region, which makes the analysis more difficult. The CaII triplet wavelength regions are also affected by Paschen lines from young hot stars and are not dominated by the red giants alone (see Figure 6 and associated discussion in Iodice et al. 2015). The discs of the gas-rich galaxies for which good HI rotation data are available usually have a continuing history of star formation and therefore include a population of young (ages < 2 Gyr), kinematically cold stars among a population of older, kinematically hotter stars. The red giants of this mixed young + old population provide most of the absorption

line signal that is used for deriving velocity dispersions from the integrated light spectra of galactic discs.

Therefore, in equation 1, we should be using the velocity dispersion of the older disc stars in combination with the scale heights of this same population for an accurate determination of the surface mass density (Jeans 1915). In practice, because of limited signal-to-noise ratios for the integrated light spectra of the discs, integrated light measurements of the disc velocity dispersions usually adopt a single kinematical population for the velocity dispersion whereas, ideally, the dispersion of the older stars should be extracted from the composite observed spectrum of the younger and older stars.

Adopting a single kinematical population for a composite kinematical population gives a velocity dispersion that is smaller than the velocity dispersion of the old disc giants (for which the scale height was measured), and hence underestimates the surface density of the disc. A maximal disc will then appear submaximal. This problem potentially affects the usual dynamical tracers of the disc surface density in external galaxies, like red giants and planetary nebulae, which have progenitors covering a wide range of ages. It therefore affects most of the previous studies. It is consistent with the discovery by Herrmann & Ciardullo (2009b), mentioned above, that the later-type (Scd) systems appear to be clearly submaximal, because these later-type systems are potentially the most affected by the contribution of the younger planetary nebulae to the velocity dispersion (see however Courteau et al. 2014 and Courteau & Dutton 2015). A recent study of the K-giants in the V-band in the solar neighbourhood by Aniyan et al. (2016) showed that the young stars contribute significantly to the total light and that the velocity dispersion derived assuming a single population of tracers (red giants) leads to the disc surface mass density being underestimated by a factor ~ 2.

Our goal in this paper is to use the kinematics and scale height of the older stars as consistent tracers to estimate the total surface density of the disc (older stars + younger stars + gas). The distribution of the older stars will be affected by the gravitational field of the thinner layer of younger stars and gas. Their dynamical contribution is often neglected in estimates of the disc surface density. If we assume that the layer of younger objects and gas is very thin, and take the velocity distribution of older stars as isothermal, then there is an exact solution for the density distribution of the older stars (see Appendix A). Their density distribution is a modified version of the familiar $\mathrm{sech}^2(z/2h_z)$ relation for the simple isothermal, and Equation 1 becomes:

$$\Sigma_T = \Sigma_D + \Sigma_{C,*} + \Sigma_{C,gas} = \sigma_z^2/(2\pi G h_z) \qquad (2)$$

where Σ_T is the total surface density of the disc, Σ_D is the surface density of the older stellar component which we are using as the dynamical tracer (its scale height is h_z and its integrated vertical velocity dispersion is σ_z). $\Sigma_{C,*}$ and $\Sigma_{C,gas}$ are the surface densities of the cold thin layers of young stars and gas respectively. An independent measurement of $\Sigma_{C,gas}$ is available from 21 cm and mm radio observations. We will see later (Table 6) that the contributions of the cold layers to the total surface density can be significant.

In this paper, we present our observations of our most face-on galaxy NGC 628 (M74) to extract a two component velocity dispersion for the motion of the hot and cold disc component independently. We combine velocity dispersion data from two sources: (1) an absorption line study of the integrated disc light using spectra from the VIRUS-W IFU instrument on the 107-inch telescope at McDonald Observatory, and (2) the velocity distribution of planetary nebulae observed using the planetary nebula spectrograph (PN.S) on the William Herschel Telescope. Section 2 describes the observations and data reduction for VIRUS-W, and section 3 summarises the same for the PN.S. Section 4 discusses the photometric properties and derives scale height of NGC 628 and section 5 briefly summarises the adopted parameters that goes into our analysis in the calculation of the surface mass density of the disc. Section 6 discusses our analysis to derive the surface mass density of the cold gas in this galaxy and section 7 details the analysis involved in the extraction of a double Gaussian model from our data. Section 8 discusses the vertical dispersion profile of the hot and cold stellar components, and section 9 describes the calculation of the stellar surface mass density. Section 10 explains the rotation curve decomposition using the calculated surface mass densities. Section 11 lists our conclusions and scope for future work. In the Appendix, we discuss the dynamical effect of the cold disc component on the hot component.

2 VIRUS-W SPECTROGRAPH

The VIRUS-W is an optical-fibre-based Integral Field Unit (IFU) spectrograph built by the University Observatory of the Ludwig-Maximilians University, Munich and the Max-Planck Institute for Extraterrestrial Physics, and used on the 2.7m Harlan J. Smith Telescope at the McDonald Observatory in Texas. The IFU has 267 fibres, each 150 μ m-core optical fibers with a fill factor of 1/3. With a beam of f/3.65, the core diameter corresponds to 3.2″ on sky, and the instrument has a large field of view of 105″ × 55″ (Fabricius et al. 2012). We use the high resolution mode of the instrument which has a spectral resolving power of R $\sim$ 8700 or an average velocity resolution of about 14.7 km s^{-1} (gaussian sigma of the PSF). The spectral coverage is 4802 – 5470 Å. The instrument is ideally suited for the study of the absorption features in the Mgb region ($\sim$ 5175 Å). We summed the spectra over the IFU, excluding those affected by foreground stars, to produce summed spectra of high signal-to-noise ratio (SNR) at two mean radii. The high SNR allows us to measure velocity dispersions somewhat lower than the velocity resolution (sigma) of the instrument.

2.1 Observations

NGC 628 is a large nearby galaxy, much larger than the field of the IFU. It was observed in October 2014. We were able to observe several fields around the galaxy with a luminosity weighted radius of about 78″. This corresponds to about 1 scale length in the R-band (Fathi et al. 2007; Möllenhoff 2004). We positioned the IFU along the major and minor axis as well as at intermediate position angles. Our IFU positions on the galaxy are shown in Figure 1. The distribution of fields around the galaxy allows us to separate the contributions to the line of sight velocity dispersion from the vertical and in-plane components of the stellar motions in the disc. Since the fields cover a large radial extent on the galaxy, we decided to split the data into two radial bins, at luminosity-weighted radii of 62″ and 109″ respectively.

The position and exposure time at each position is given in

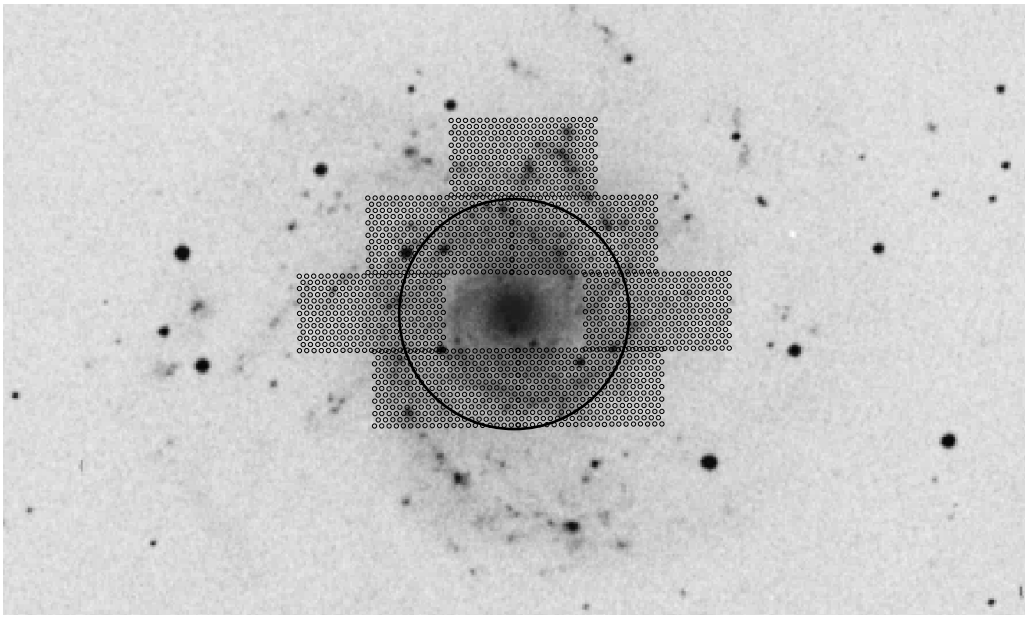

Figure 1. The positions of the VIRUS-W IFU fields overlaid on a DSS image of NGC 628. The position of the 267 fibres in each field are also shown. The circle at 85″ shows where we separated our data into the inner and outer radial bin.

Table 1. Each of the galaxy exposures were preceded and followed by a sky exposure of equal time. We repeated this sky -> galaxy -> sky sequence at least thrice at each field, as indicated in column 3 of Table 1. This enabled very good sky subtraction using the automated pipeline developed for VIRUS-W.

RA (J2000)	Dec (J2000)	Exposure Time (s)
1:36:49.00	+15:47:02.7	3 × 800
1:36:34.36	+15:47:02.1	3 × 800
1:36:45.19	+15:47:02.1	3 × 800
1:36:37.85	+15:46:06.5	3 × 800
1:36:45.46	+15:48:00.0	3 × 800
1:36:38.10	+15:47:59.1	3 × 800
1:36:41.16	+15:48:56.9	5 × 800

Table 1. Coordinates and exposure times for the IFU fields in NGC 628.

2.2 Data Reduction and Extraction of Spectrum

The raw data were reduced using the automated pipeline 'CURE' which was orginally developed for HETDEX, but later adapted for VIRUS-W data reductions. The pipeline uses the biases and dome flats obtained during observation to debias and flat field correct the raw data. The pipeline then uses the observed arc frames for the wavelength calibration of the images. The final step is extraction of the spectrum from each fibre and then subtracting the sky. The sky frames preceding and succeeding the galaxy image are averaged and scaled to match the exposure time of the galaxy frame, which is then subtracted from the galaxy image. The data were reduced in log-wavelength space. The velocity step of the spectrum is ~ 11 km s^{-1}. As a check on the stability of the instrument we independently measured the dispersion of a few arc lines. Our measured values agree with the dispersions quoted in Fabricius et al. (2012) with $\sigma \sim 14$ km s^{-1} near the Mgb region. As an added check, we combined all of our sky images to produce a 2D sky image with very high counts. We then measured the wavelengths of some known sky emission lines in the 1D spectrum from one of the fibres in this 2D image and compared them with the Osterbrock et al. (1996) wavelengths. This comparison is shown in Table 2. Since the positions of the emission lines in this spectrum match the known values, we cross-correlated the other 266 fibre spectra with this spectrum to see if there are any significant shifts in the wavelength solution. The shifts obtained from the correlation peak are all < 2 km s^{-1}. Thus the VIRUS-W is a very stable instrument and the errors in the wavelength system make a negligible contribution to the error budget.

The sky subtracted images from the reduction pipeline were combined and the spectra from each fibre in each field were summed to get a single spectrum at each of our two radial bins. The spectrum from each fibre was corrected for variations in systematic velocity over the IFU before they were summed together. This is explained in detail in section 7.1.

Measured Wavelength (Å)	Osterbrock Wavelength (Å)
5202.89	5202.98
5238.81	5238.75
5255.97	5256.08

Table 2. Comparison between the measured wavelengths of the sky lines from one of the fibres of our combined sky spectrum and the values from Osterbrock et al. (1996). This fibre was then cross-correlated with the other fibres to check for any significant wavelength shifts. The shifts were all < 2 km s^{-1}, indicating that errors in the wavelength system make a negligible contribution to the error budget.

3 PLANETARY NEBULA SPECTROGRAPH

Planetary nebulae (PNe) are part of the post-main-sequence evolution of most stars with masses in the range 0.8 to 8 $M_\odot$. Up to 15% of the flux from the central stars of PNe is reprocessed

into the [OIII] emission line at 5007 Å (Dopita et al. 1992). These objects are plentiful in stellar populations with ages between 0.1 and 10 Gyr. The above properties make PNe useful probes of the internal kinematics of galaxies. They can be detected in galaxies out to many Mpc. They are easier to detect at large galactocentric radii where the background continuum is fainter, and are therefore an important complement to integrated light absorption-line studies.

The planetary nebula spectrograph (PN.S) is an imaging spectrograph designed for efficient observation of extragalactic PNe, and is used for the present project (Douglas et al. 2007). It operates on the 4.2 m William Herschel Telescope at La Palma, and has a field of view of 10.4×11.3 arcmin^2. The PN.S has a 'left' and 'right' arm in which the light is dispersed in opposite directions. Combining these two counter-dispersed images allows the PNe to be detected and their radial velocities to be measured in a single observation. The PN.S also has an undispersed Hα imaging arm which can help to distinguish HII regions and background Lyα emitters from the PNe.

The PN.S is used by the PN.S collaboration, so far mainly on early-type galaxies (Coccato et al. 2009; Cortesi et al. 2013) plus a study of PNe in M31 (Merrett et al. 2006). Arnaboldi et al. (2017) describe a new survey of nearby face-on disc galaxies, aimed at measuring the internal kinematics of these discs, and illustrate the analysis of the new PN.S data for the prototypical galaxy NGC 628. The present paper presents the first results derived from these measurements in an attempt to break the disc-halo degeneracy.

3.1 Observations, Data Reduction, and Velocity Extraction

The data for NGC 628 were acquired over two nights during a 4 night observing run in September 2014. The weather during the run was excellent, with typical seeing being $\sim 1''$. We obtained 14 images centred on the centre of the galaxy, each with an exposure time of 1800s. At the redshift of NGC 628, the wavelength of the [OIII] emission is near 5018 Å.

A detailed description of the data reduction can be found in Douglas et al. (2007) and Arnaboldi et al. (2017). The automated reduction procedure debiases and flat-field-corrects the raw images from the left and right arms, using bias frames and flats obtained during the observing run. Cosmic rays are removed using a custom-built routine in the pipeline. The wavelength calibration of the dispersed images was improved for this project by implementing a higher-order polynomial fit to the arc line calibration images taken during the observing run. After wavelength calibration, the 14 left and right arm images were stacked to create the final dispersed galaxy images.

Simultaneously with the [OIII] imaging, NGC 628 was also observed in Hα, using the Hα narrow band filter on the undispersed Hα arm of the PN.S. The Hα arm and the reduction of these data are described in Arnaboldi et al. (2017).

3.2 Identification of Sources

Identification of PNe in late type galaxies brings in a new set of challenges, due mainly to contamination from HII regions. HII regions can also have strong [OIII] emission, and it is important to distinguish them from true PNe candidates.

Arnaboldi et al. (2017) describes the extraction of [OIII] emitters in the stacked left and right arm images for NGC 628. After removing extended sources, we were left with a catalogue of 716 spatially unresolved [OIII] sources. From the measured positions of these sources on the left and right images, astrometric positions and LOS velocities were derived simultaneously.

We converted our instrumental magnitudes to the m_{5007} magnitude scale used by Herrmann & Ciardullo (2009b), using our spectrophotometric calibration. This is accurate to within 0.05 mag. This allows us to directly compare our results to the values in Herrmann & Ciardullo (2009b). From here on, we shall only be using these m_{5007} values. The bright luminosity cut-off for PNe in this galaxy is expected to be $m_{5007} = 24.73$ (see Figure 2).

Our sample of 716 identified sources is still a mixture of spatially unresolved HII regions and PNe, since both can have strong [OIII] emissions. In the companion paper, Arnaboldi et al. (2017), we detail how we separated the spatially unresolved HII regions from PNe in the disc of NGC 628 using an [OIII]/Hα color-magnitude cut that accounts for the apparent [OIII] magnitude of the bright cut-off in the PNLF and the large [OIII]/Hα emission line ratio of bright PNe.

The line-of-sight velocity distributions of the HII regions and the PNe have different second moments (σ_{LOS}) in different radial bins. The σ_{LOS} for the PNe correlates with m_{5007}. There is a kinematically cold population near the PNLF bright cut off, and then the velocity dispersion increases towards fainter magnitudes. This correlation is reminiscent of the age-magnitude-(vertical velocity dispersion) relation of the K-giant stars in the solar neighbourhood as shown by Aniyan et al. (2016) (also see Figure 10 in this paper).

Another possible source of contaminants in the emission line sample are historical supernovae. According to the IAU Central Bureau for Astronomical Telegrams (CBAT) List of Supernovae website (http : //www.cbat.eps.harvard.edu/lists/Supernovae.html), there are three known historical supernovae in NGC 628. None of these objects made it into our PNe sample. An [OIII] emission line source was found at a distance of $1.6''$ from SN 2002ap. However, on applying our colour-magnitude cut, this object was classified as an HII region. We, therefore, conclude that these contaminants are removed from our PNe sample by the colour-magnitude cut as well.

Figure 2 shows the luminosity function, including all 716 sources, and indicates the position of the bright luminosity cut-off for the PNe. The colour-magnitude cut on our 716 emission objects left us with about 400 objects. The LOS velocities for this sample are then used to calculate the velocity dispersions for the hot and cold PNe components.

3.3 Velocity errors

Space and wavelength information are closely related in an imaging spectrograph like the PN.S (see section 3.2). The left and right PN.S images are registered on the best quality image, which had the best seeing etc, so there is some correlation between the frames. In order to get an empirical estimate of the radial velocity measuring errors associated with each PN, we divided our 14 left and right images into two sets and then independently identified the unresolved [OIII] sources in each set. We had to split our sample into a set of 8 images and 7 images, since the 'reference image' used to stack the other images was common to both sets. We assume the radial velocity errors depend only on the total counts, not on the number of frames and

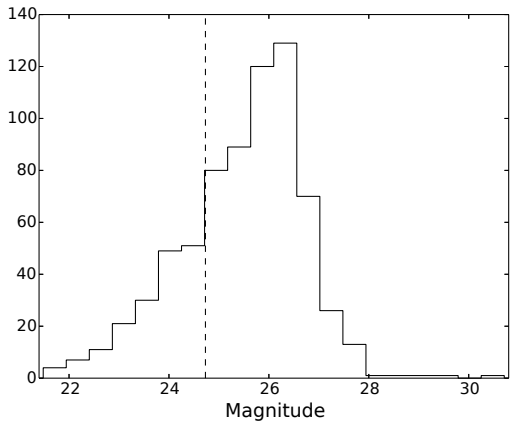

Figure 2. The luminosity function for all spatially unresolved [OIII] emitters identified in the combined left and right images of the PN.S. The dashed line shows the expected bright luminosity cut-off for PNe. We include only objects fainter than this value in our analysis. Objects brighter than the cut-off are mostly obvious bright HII regions.

that the velocity error of a single measurement at each count level, for all 14 frames, is the (rms of the difference between two velocity measurements at that count level)/ $\sqrt{2}$, if there was no correlation between different images. However, since we had one image in common between the two sets, we carried out monte carlo simulations on the two image sets and the combined final image and found that the typical radial velocity error of a single measurement at each magnitude in the final image is (1/1.805) times the rms velocity difference between the two image sets at the same magnitude. Figure 3 shows the error expected for a single measurement from the whole set of 14 images, as a function of the m_{5007} magnitude. Objects used in the subsequent analysis are those to the right of the vertical dashed line, which marks our bright cut-off. Most of these objects have estimated radial velocity errors between about 4 and 9 km s^{-1}.

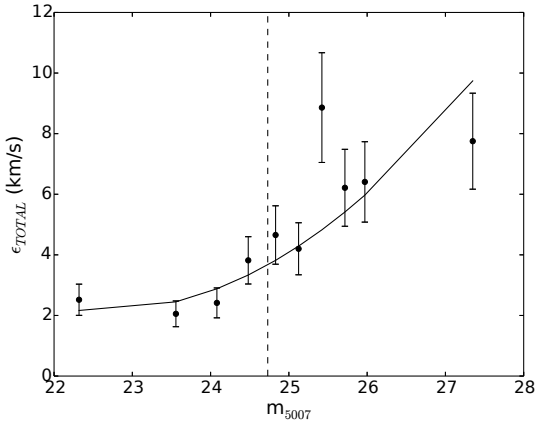

Figure 3. The measuring error for our sample of objects as a function of apparent magnitude. The magnitude system is the same as in Herrmann & Ciardullo (2009b). The dashed line shows the bright luminosity cut-off for this galaxy. Only the objects fainter than this magnitude were used in our analysis. The solid curve is the best fit to the data.

4 PHOTOMETRIC PROPERTIES AND SCALE HEIGHT

We use BVRI surface brightness profiles from Möllenhoff (2004), consistent with the Herrmann & Ciardullo (2009b) analysis. Möllenhoff (2004) tested their fit procedures extensively with artificial galaxies, including photon noise and seeing convolution. The statistical errors were found to be very small. The relevant errors were the systematic errors like the non-correct sky-subtraction, non-uniformness of the sky, errors in the determination of the seeing point-spread-function (Möllenhoff 2004). To estimate the error contributions of these effects, artificial galaxy images with typical sky levels, shot noise and seeing convolution were fitted with their 2-dimensional models. The sky level and the PSF were artificially set to different, slightly wrong values and the effect in the resulting photometric parameters was studied. They conclude that the errors due to inaccurate sky levels or PSF determinations are ~ 5% for the basic photometric parameters i.e the central flux density and the scale lengths (Möllenhoff 2004). We will adopt this error estimate in our analysis.

Determining the scale height for a face-on disc like NGC 628 is challenging. We need to make use of previous studies of edge-on discs that find correlations between the scale height and other properties of the galaxy such as its circular velocity (Yoachim & Dalcanton 2006) or its I-band scale length (Kregel et al. 2002). Since NGC 628 is so nearly face-on, it is difficult to measure its circular velocity V_c directly. We attempted to make an independent estimate of the scale height, using the absolute magnitude of NGC 628 to estimate its circular velocity and hence the scale height. We used HI data for NGC 628 from the THINGS survey to determine V_c = 180 ± 9 km s^{-1}. Our analysis for determining the rotation curve is detailed later in section 10. Yoachim & Dalcanton (2006) find the scale heights h_z of the thin disc and circular velocities of edge-on galaxies (see Figure 9 in Yoachim & Dalcanton 2006) follow the relation $h_z = 305(V_c(\mathrm{km\ s^{-1}})/100)^{0.9}$ pc. This study took the vertical density distribution to be isothermal. We use this relation to estimate h_z = 518 ± 23 pc, which is much higher than the scale height of the MW ~ 300 pc. Yoachim & Dalcanton (2006) mention that for massive galaxies with large circular velocities (V_c > 170 km s^{-1}), their derived value for the scale height of the thin disc is larger than that for the MW. This could be because these galaxies have more prominent dust lanes, which may substantially obscure our view of the thin disc and lead to an overestimate of its scale height. Since the method described in Yoachim & Dalcanton (2006) is known to be uncertain for large dusty galaxies, we attempt to derive the scale height via alternate methods.

Herrmann & Ciardullo (2009b) reason that the scale height for NGC 628 should be in the range 300 – 500 pc based on the h_z values obtained based on correlations of scale height with Hubble type (De Grijs & van der Kruit 1996), scale length (Kregel et al. 2002), and K-band central surface brightness of the galaxy (Bizyaev & Mitronova 2002). They further argue that for the thin stellar disc to be stable against axisymmetric perturbations, it should satisfy the Toomre (1964) criterion: $\sigma_R > 3.36G\Sigma/k$, where σ_R is the radial component of the dispersion, G is the gravitational constant, Σ is the surface mass density of the disc, and k is the epicycle frequency. Factoring these constraints into their analysis, they claim that h_z = 400 ± 80 pc is a reasonable estimate of the scale height of NGC 628. However, disc stabil-

ity arguments are not very well-established and have significant uncertainties associated with them.

Kregel et al. (2002) studied edge-on galaxies in the I-band and found correlations between the scale height and the I-band scale lengths. Using the redder I-band photometry minimises the effect of dust in the galaxy, while at the same time minimising the effects of PAHs that are a problem in the NIR wavelengths. Bershady et al. (2010b) fit the Kregel et al. (2002) data and find the relation: $\log(h_R/h_z) = 0.367 \log(h_R/\mathrm{kpc}) + 0.708 \pm 0.095$. Using this relation for NGC 628, and adopting the I-band $h_R = 73.4 \pm 3.7''$ from Möllenhoff (2004) and distance = 8.6±0.3 Mpc (Herrmann et al. 2008), we get $h_z = 397.6 \pm 88.3$ pc.

However, we could not access the surface brightness profile data from Möllenhoff (2004). We only had the central surface brightness and scale length of the fit to the data in the various bands. In order to verify that the scale lengths from Möllenhoff (2004) was reasonable, we decided to check the 3.6 μm surface brightness profile for NGC 628 from the S4G survey (Muñoz-Mateos et al. 2013; Salo et al. 2015). Figure 4 shows the surface brightness profile of NGC 628 at 3.6 μm. It is clear from the figure that NGC 628 has a pure exponential disc with the scale length $h_{3.6} = 69.34''$ (Salo et al. 2015). The 3.6 μm scale length agrees fairly well with the I-band scale length from Möllenhoff (2004). The red and green lines in Figure 4 are the fits to the bulge and disc respectively. While the total bulge light contributes only 6.5% to the total light of the galaxy, the bulge light dominates within the central 1.5 kpc and, therefore, it needs to be taken into account in the mass modelling.

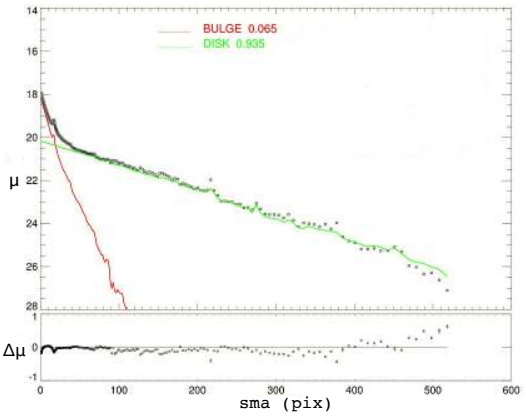

Figure 4. 3.6 μm surface brightness profile from the S4G survey (Muñoz-Mateos et al. 2013; Salo et al. 2015). The y-axis shows the surface brightness profile (in AB magnitude) and the x-axis is the distance along the semi-major axis (with a pixel scale of 0.75 arcsec/pixel). The bottom panel shows the residuals between the data and the fit. The red and green lines are the fits to the bulge and exponential disc respectively. The bulge contributes only 6.5% of the total light in this galaxy.

The relation from Kregel et al. (2002) uses the I-band scale length. Having accurately determined the $h_{3.6}$ from Salo et al. (2015), we use the relation from Ponomareva (2017) between the scale lengths in i-band and 3.6 μm band, calibrated for a sample of 20 disc galaxies. This relation is shown in Figure 5. This gives us the scale length in i-band via the relation: $log(h_i) = 0.9log(h_{3.6}) + 0.19 \pm 0.05$. This gives us the scale length in the SDSS i-band as $70.3 \pm 8.1''$, which is close to the I-band scale length from Möllenhoff (2004). Using this value for the i-band scale length, gives us a scale height $h_z = 386.9 \pm 89.6$ pc.

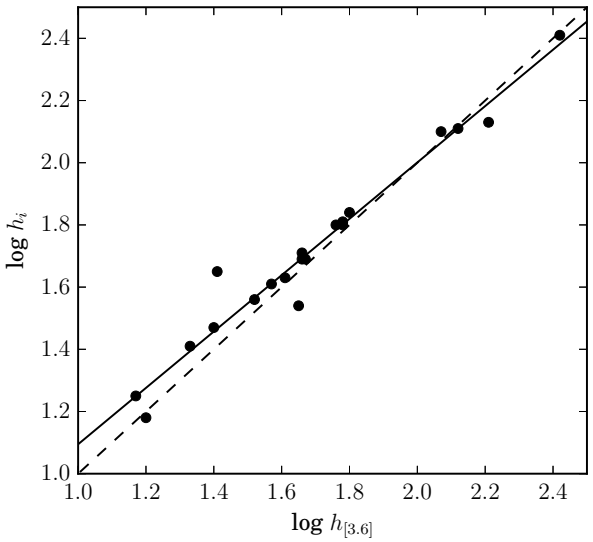

Figure 5. Relationship between the SDSS i-band scale length and the 3.6 μm scale length from Ponomareva (2017). The solid line is a linear fit to the data. The dashed line is a line with slope = 1.

The scale height obtained using the Möllenhoff (2004) photometry is remarkably close to the scale height estimate got using the 3.6 μm photometry. We will therefore use the Möllenhoff (2004) photometry in all further analysis, and adopt the scale height value as $h_z = 397.6 \pm 88.3$ pc.

5 ADOPTED PARAMETERS

In order to proceed with the calculation of the surface mass densities and the subsequent M/L of the disc, we need to establish the values that we will adopt for certain parameters. These parameters are obtained from previous literature values and are listed in Table 3.

The stellar velocity ellipsoid parameter, σ_z/σ_R, is rather uncertain for external galaxies. However, it is important to adopt a value for this parameter in order to convert our observed line-of-sight velocity dispersions to the vertical velocity dispersion. Solar neighbourhood studies have estimated this parameter to be between 0.5 – 0.7 (see Wielen 1977;Woolley et al. 1977; Bienaymé 1999; Dehnen & Binney 1998). Van der Kruit & de Grijs (1999) studied a sample of edge-on spiral galaxies and estimated their typical σ_z/σ_R. This analysis involves several dynamical assumptions and scaling arguments. They do not find any trend in σ_z/σ_R as a function of morphological type or rotational velocity of the galaxy. Shapiro et al. (2003) studied six nearby spiral galaxies and combined their data with the results from Van der Kruit & de Grijs (1999). They find a marginal trend of a declining σ_z/σ_R with Hubble type. However, these results have significant errors. For later type spirals, it can be argued that the σ_z/σ_R doesn't show any trend, and seem to have a constant value of ≈ 0.6 albeit with large uncertainties (see Figure 5 in Shapiro et al. 2003). We, therefore, adopt the σ_z/σ_R to be 0.60 ± 0.15 (uncertainty at 25%) for this galaxy. This is similar to the value adopted by the DMS team (Bershady et al. 2010b). It is interesting to note that the error on this stellar velocity ellipsoid parameter has a negligible effect on the total er-

ror budget for a galaxy as face-on as NGC 628 (see Figure 5 in Bershady et al. 2010b).

Parameters	Value/ Description	Data source
Inclination	8.5° ± 0.2°	Walter et al. (2008)
Distance	8.6 ± 0.3 Mpc	Herrmann et al. (2008)
Scale length (I-band)	73.4 ± 3.7″	Möllenhoff (2004)
Scale height	397.6 ± 88.3 pc	Kregel et al. (2002)
σ_z/σ_R	0.60 ± 0.15	
Photometry	BVRI bands	Möllenhoff (2004)
Photometry	3.6 μm band	Salo et al. (2015)

Table 3. The parameters for NGC 628 adopted from the literature and used in our analysis.

The inclination was determined via kinematic fit to the HI data from the THINGS survey (Walter et al. 2008). This procedure is detailed in section 10.

6 SURFACE MASS DENSITIES OF THE COLD GAS

As mentioned in section 1, our velocity dispersion analysis gives the total surface density of the disc, including the gas. We do however need the surface density of the cold gas to derive the separate surface densities of the hot and cold stellar components (see Table 6), because these components have different flattenings which should, for completeness, be included when computing their contributions to the rotation curve. We derived the HI surface density profile using the THINGS HI data for NGC 628 (Walter et al. 2008). We created an integrated column-density HI map by summing the primary beam-corrected channels of the clean data cube. The radial surface density profile was then derived by averaging the pixel values in the concentric ellipses projected on to the HI map. We will use the same radial sampling, position and inclination for obtaining the rotation curve (see section 10.1).

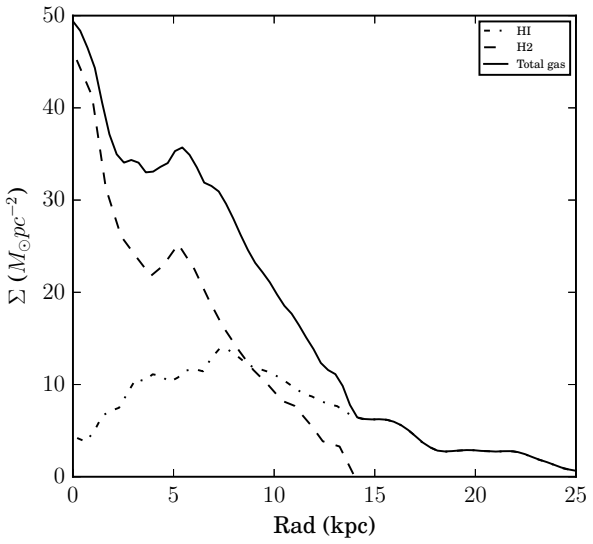

Figure 6. Surface mass density of the cold gas in NGC 628. The HI density profile from Walter et al. (2008) is shown as the dot dashed line and the H2 profile derived using the CO profile from Leroy et al. (2009) is shown as the long dashed curve. The surface density profile of the total gas is shown as the solid curve.

The resulting pixel values were converted from flux density units [Jy/beam] to column densities [atoms cm^{-2}], using equation 5 in Ponomareva et al. (2016). The resulting HI surface density profile is shown in Figure 6 in the dot dashed line. We adopted the error on the surface density as the difference between surface density profiles of the approaching and receding sides of the galaxy.

We derived the H2 surface density profile by using the CO profile from the HERACLES survey (Leroy et al. 2009). We then converted the CO intensities into H2 surface densities following the method outlined in Leroy et al. (2009). The resulting H2 profile is shown in Figure 6 as the long dashed curve. The error on the H2 densities were obtained from the HERACLES error maps for NGC 628.

The HI and H2 surface mass density profiles gives us the total gas surface mass density in this galaxy. This is shown as the solid line in Figure 6. All profiles were de-projected so as to be face-on and were corrected for the presence of helium and metals.

7 EXTRACTING VELOCITY DISPERSIONS OF THE HOT AND COLD COMPONENTS

7.1 Stellar Absorption Spectra

7.1.1 Removing Galactic Rotation

For the VIRUS-W data, the automated pipeline 'CURE' returns a two dimensional FITS image, where each row represents a fibre spectrum and the x-axis is the wavelength dimension. Our goal is to measure the line of sight velocity dispersion (σ_{LOS}) without including the effects of galactic rotation across the field of the IFU. One option for removing galactic rotation would be to model the rotation field over the IFU using the observed rotation curve. Alternatively, we could use the local observed HI velocity at the position of each of the IFU fibres, and we have chosen this option. We used the 21 cm HI data from the THINGS survey (Walter et al. 2008). We assume that the spectrum from each fibre is shifted in velocity by the local HI velocity. Although this procedure removes the galactic rotation and any large scale streaming motions across the field of the IFU, it will however introduce an additional small component of velocity dispersion to the apparent stellar velocity dispersion. This is because the motion of the gas is not purely circular and we will need to correct for its (small) effect on the derived stellar dispersion.

Initially, we made a double Gaussian analysis to derive the velocity dispersion for the hot and cold components of the disc. To get sufficient SNR for this double Gaussian analysis, we sum up all the shifted spectra (one from each fibre) over the IFU field, to get a single spectrum (at each radial bin). IFU fibres that fell on stars in the field are excluded from the sum. We used the penalized pixel-fitting code pPXF developed by Cappellari & Emsellem (2004) (see also Coccato et al. 2011; Cappellari 2017) to get the mean velocity and velocity dispersion of the two components. This code uses a list of stellar templates to directly fit the spectrum in pixel space to recover the line of sight velocity distribution (LOSVD). pPXF can fit up to six higher moments to describe the LOSVD. It has options to fit either 1 or 2 LOSVD to the given spectrum, each with up to 6 moments. We used stars of different spectral types observed with VIRUS-W as our list of stellar templates. This avoids any problems of reso-

lution mismatch between the stellar templates and the galaxy spectrum. pPXF then finds a best-fit spectrum to the galaxy spectrum, which is a linear combination of different stellar templates. We assume the two components of the LOSVD to be Gaussian for this nearly face-on galaxy, and therefore retrieved only the first and second moment parameters from pPXF.

The final summed spectra used in our analysis have an SNR of 79 and 62 per wavelength pixel for the spectrum from the inner and outer radial bins respectively (each wavelength pixel is ~ 0.19 Å). These SNR values are empirical estimates obtained by taking into consideration the contribution of the galaxy and sky shot noise and the readout noise of the detector. The VIRUS-W instrument has a wavelength-dependent resolution, offering the highest resolution R $\sim$ 9000, around the Mgb region ($\lambda \sim 5160$ Å). Therefore, we only used the region between wavelengths of about 5050 – 5300 Å in our analysis, since it has the highest resolution and avoids the emission lines at lower wavelengths. The [NI] doublet emission lines from the interstellar medium of the galaxy can be seen at ~ 5200 Å (see Figure 7). These are not residual sky lines: they appear at the redshift of the galaxy.

7.1.2 *Measuring the LOSVD*

As explained in section 7.1.1, we did a double Gaussian fit to the data, fitting for two moments for each component. In this case, pPXF returns the velocity and the line-of-sight (LOS) dispersions for the two component and for the single component fit. Adding more parameters to the model invariably improves the fit to the data. We therefore need to quantitatively decide whether the 2 Gaussian or single Gaussian model is a more appropriate fit to the data. To do this, we used the Bayesian Information Criterion (BIC; Schwarz 1978), which is calculated using the relation:

$$\mathrm{BIC} = -2 \cdot \ln \hat{L} + k \cdot \ln(n), \tag{3}$$

where $\hat{L}$ is the maximized value of the likelihood function of the model, n is the number of data points or equivalently the sample size and k is the number of free parameters to be estimated. Under the assumption that the model errors are independent and are Gaussian, equation 3 becomes:

$$\mathrm{BIC} = n \cdot \ln(RSS/n) + k \cdot \ln(n) \tag{4}$$

where RSS is the residual sum of squares.

The BIC penalises the model with the larger number of fitted parameters and, between 2 models, the model with the lower BIC value is preferred. The values of the BIC for our VIRUS-W spectra are tabulated in Table 4. Since the model with the lower value of BIC is preferred, the two component fit is preferred over the single component fits in both radial bins.

We then attempted to carry out a triple Gaussian fit to the data, to check if we have any contribution from the thick disc. However, we could not get a third component in our fit when the data were divided into two radial bins. The degeneracy between the hot thin disc and the thick disc component, led to errors that were unacceptably large. We were able to get a third component with a dispersion consistent with a thick disc component if we only considered one radial bin and summed up the data from all the fibres. However, this third component may just be an artefact of the gradient of the velocity dispersion, since we are summing up the data over such a large radial extent. The information criterion that we used to judge the best model also rejects the three component fit. Therefore, we conclude that there is no significant thick disc contribution present in our data.

pPXF found an excellent fit to our spectrum for the two-component case, as shown in Figure 7. It returns the adopted spectra of the individual components, and the 2 spectra that it returns are consistent with the spectra of red giants. The mean contributions of the cold and hot disc components to the total light are 36% and 64% respectively. Figure 8 compares the two components found by pPXF in the inner radial bin. These are a linear combination of unbroadened stellar spectra, identified by pPXF as the best fit to our galaxy spectrum. The colder component with the smaller dispersion (in red in Figure 8) are also weaker lined as compared to the hotter component. This shows that the colder component is in fact the younger of the two components.

As mentioned earlier, since we used the THINGS HI data to remove rotation across the fields, we need to correct these two dispersion values for the contribution from the scatter of the HI velocities about the mean smooth HI flow over the field of the IFU. This correction was determined by fitting a plane function $V = ax + by + c$ to the HI velocities at the (x, y) location of the individual VIRUS-W fibres at each IFU pointing. The rms scatter of the HI velocities about this plane is 2.5 km s^{-1}. We note that this is the rms scatter of the mean HI velocities from fibre to fibre, which is not the same as the HI velocity dispersion. Correcting for this scatter changes the observed dispersions by only a very small amount. Table 4 shows our results after subtracting this value quadratically from the pPXF results.

The errors on the σ_{LOS} are computed from monte carlo simulations. This was done by running 1000 iterations where, in each iteration, random Gaussian noise appropriate to the observed SN of the IFU data was added to the best fit spectrum originally returned by pPXF. pPXF was run again on the new spectrum produced in each iteration. The errors are the standard deviations of the distribution of values obtained over 1000 iterations. The errors on σ_z presented in Table 4 take into account the errors on the inclination, σ_z/σ_R value, as well as the monte carlo errors on σ_{LOS}. The errors on the LOS dispersions are the dominant source of errors.

Mean Radius (arcsec)	2 component Model				1 Component Model		
	$\sigma_{z,cold}$ (km s^{-1})	$\sigma_{z,hot}$ (km s^{-1})	χ^2_{red}	BIC	σ_z (km s^{-1})	χ^2_{red}	BIC
62	16.7 ± 3.6	55.4 ± 6.4	0.95	17923	31.9 ± 1.1	1.04	18107
109	15.2 ± 3.8	50.9 ± 8.9	1.11	19021	25.1 ± 1.2	1.15	19064

Table 4. The single and double Gaussian fit from pPXF. For each component, the Table gives the vertical velocity dispersion σ_z for each of the components; see section 7.1.3. Dispersions have been corrected for the contribution from the HI velocity dispersion. An estimate of the reduced χ^2 and the Bayesian Information Criterion parameter BIC defined in equation (3) is also given.

7.1.3 *Extracting the Vertical Velocity Dispersion*

The vertical component of the stellar velocity dispersion σ_z was calculated from the line of sight component σ_{LOS} by first calculating the azimuthal angle (θ) to each fibre. The angle θ is measured in the plane of the galaxy, from the line of nodes. Then the LOS dispersion is given by:

$$\sigma^2_{LOS} = \sigma^2_\theta \cos^2\theta . \sin^2 i + \sigma^2_R \sin^2\theta . \sin^2 i + \sigma^2_z \cos^2 i + \sigma^2_{meas} \tag{5}$$

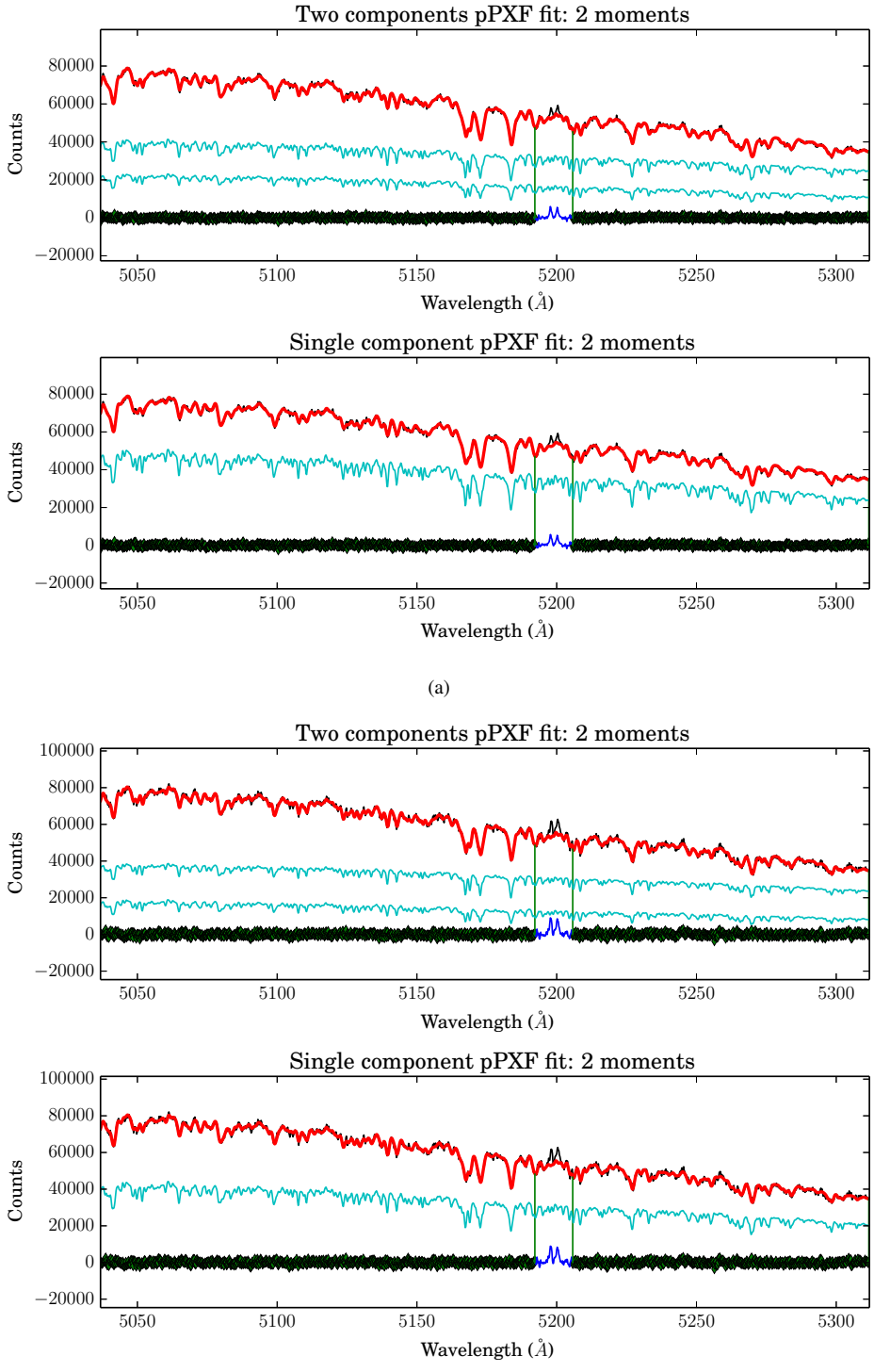

Figure 7. The pPXF fit results in (a) the inner radial bin at a luminosity weighted distance of 62″ and (b) the outer bin at a luminosity weighted distance of 109″. The upper panel shows the 2 component fit to the data whereas the lower panel shows a single component fit. Only the high resolution Mgb region of the spectrum was used for the fit. The galaxy spectrum is in black and the best fit from pPXF is in red. The cyan spectra are the two and one component spectra that pPXF found. The cyan spectra have been shifted vertically so as to be clearly visible. The residuals are shown in dark green. The [NI] doublet emission lines from the galaxy at ~ 5200 Å have been omitted from the fit.

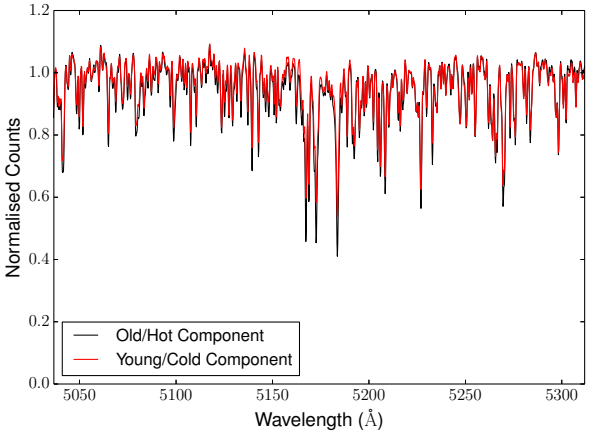

Figure 8. The two components found by pPXF in the inner radial bin of NGC 628. The spectrum in red represents the cold component, which is weaker lined than the hot component in black. The colder component found by pPXF is thus younger than the hotter component.

where σ_R, σ_θ and σ_z are the three components of the dispersion in the radial, azimuthal and vertical direction, σ_{meas} are the measurement errors on the velocity and i is the inclination of the galaxy ($i = 0$ is face-on). This galaxy is too face-on to solve independently for the in-plane velocity dispersion components. We wish to remove the small contribution that the planar components make to the LOS distribution, so we adopt $\sigma_R = \sigma_\theta$ for $R < 80''$ where we take the rotation curve to be close to solid body. This is a fair assumption, based on an examination of the THINGS HI velocities along the galaxy's kinematic major axis. We also adopt the σ_z/σ_R ratio to be 0.60 ± 0.15 (see Table 3), which is consistent with the value used by Bershady et al. (2010b) and the value found in the solar neighbourhood. Equation 5 then gives σ_z in terms of σ_{LOS}. Since NGC 628 is almost face-on, the σ_{LOS} and σ_z values are almost the same.

Our choice to remove the rotation and streaming across the IFU fields by using the local HI velocities introduced a small additional broadening of the LOS velocity distribution, as described above. This small broadening (~ 2.5 km s^{-1}) was quadratically subtracted from the dispersion values returned by pPXF. Our results for the stellar σ_z values are presented in Table 4. The errors are the 1σ errors from monte carlo simulations (as explained in section 7.1.2).

7.2 Planetary Nebulae

7.2.1 Removing Galactic Rotation

As in the analysis of the IFU integrated light absorption spectra, we again need to remove the effects of galactic rotation from the PNe velocity field. We used the THINGS HI data as before, and obtained the HI velocity at the position of all our PNe from the THINGS first moment data. There appeared to be a small systematic offset ~ 15 km s^{-1} between our PNe velocities and the THINGS HI data. We calculated this offset by cross-correlating the two data sets and determining the velocity of the correlation peak. This offset was then subtracted from the PNe velocities. The local HI velocities were then subtracted from these offset-corrected PNe velocities.

These velocities, corrected for the offset and with the galactic rotation removed are henceforth denoted v_{LOS}. They are the velocities that are used in our analysis to calculate the velocity dispersions. As for the IFU data (section 7.1.3), the radius and azimuthal angle (θ) of the PNe in the plane of the galaxy were calculated, and the v_{LOS} data were then radially binned into 3 bins, each with about 130 PNe. As explained in section 3.3, we applied a colour-magnitude cut using the [OIII] and Hα magnitudes, to separate out the contamination from likely HII regions. Figure 9 shows the v_{LOS} vs θ plots in each radial bin before and after the HI velocities were subtracted off.

7.2.2 Extracting the LOSVD

In each radial bin, we remove a few 3σ outliers, consistent with the analysis by Herrmann & Ciardullo (2009b), who clipped their sample of PNe to remove high-velocity contaminants from their sample. These outliers could be halo PNe or thick disc objects, and should be removed from our sample. Only a small number of objects in each radial bin have velocities $> 3\sigma$. A maximum likelihood estimator (MLE) routine written in python was then used to calculate the LOS velocity dispersions and the subsequent σ_z in each radial bin.

The first iteration in this routine estimates σ_{LOS} for the two components. The routine maximises the likelihood for the two-component probability distribution function given by:

$$P(\mu_1, \sigma_1, \mu_2, \sigma_2) = \frac{1}{\sqrt{2\pi}}\left[\frac{N}{\sigma_1}\exp\left(-\frac{(v_{LOS}-\mu_1)^2}{2\sigma_1^2}\right) + \frac{1-N}{\sigma_2}\exp\left(-\frac{(v_{LOS}-\mu_2)^2}{2\sigma_2^2}\right)\right] \quad (6)$$

In equation 6, μ_1 and μ_2 are the mean LOS velocities and σ_1 and σ_2 are the LOS dispersions of the cold and hot component respectively. N is the fraction of the cold tracers in the data.

7.2.3 Extracting the Vertical Velocity Dispersion

In order to calculate the surface mass density using equation 1, we need the vertical velocity dispersion of the hot component and the scale height of the same component. For NGC 628, which is a near face-on system, the σ_z value will be very close to the σ_{LOS} values. To determine this value, we again use an MLE method. Two parameters are passed to the function in this stage: σ_{z1} and σ_{z2} which are the vertical velocity dispersions of the cold and hot components respectively. The σ_{LOS} values obtained using the method described above are passed to the routine as initial guesses, since the σ_z will be very close to the value of σ_{LOS} for this galaxy. We assume $f = \sigma_z/\sigma_R = 0.60 \pm 0.15$ and use inclination $i = 8.5° \pm 0.2°$ (see Table 3). The PN.S data are all at radii $> 80''$ where the rotation curve is flat, and we use the epicyclic approximation: $\sigma_R = \sqrt{2}\sigma_\theta$, where σ_R and σ_θ are the in-plane dispersions in the radial and azimuthal directions. Now there is only one unknown σ_z, which we need to calculate.

Once the initial guesses are passed to the routine, it calculates the expected σ_{LOS} for the hot and cold component at each azimuthal angle (θ) using the relation:

$$\sigma^2_{LOS\,1} = \frac{\sigma^2_{z1}f^2}{2}\cos^2\theta.\sin^2 i + \sigma^2_{z1}f^2\sin^2\theta.\sin^2 i + \sigma^2_{z1}\cos^2 i$$

$$\sigma^2_{LOS\,2} = \frac{\sigma^2_{z2}f^2}{2}\cos^2\theta.\sin^2 i + \sigma^2_{z2}f^2\sin^2\theta.\sin^2 i + \sigma^2_{z2}\cos^2 i$$

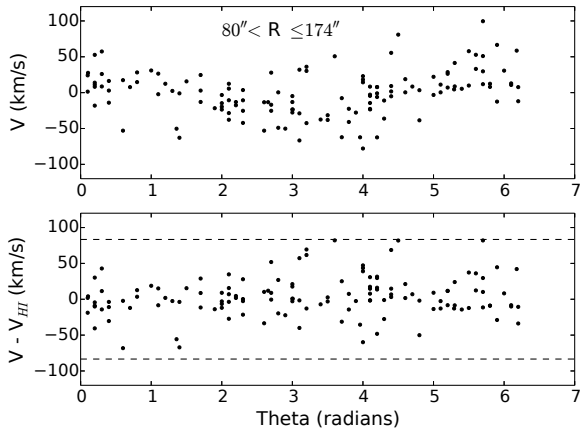

(a)

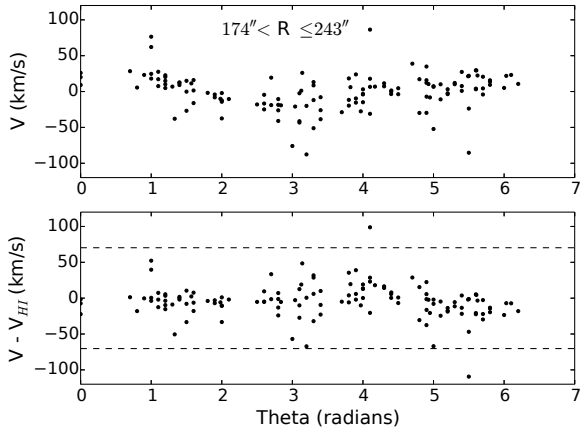

(b)

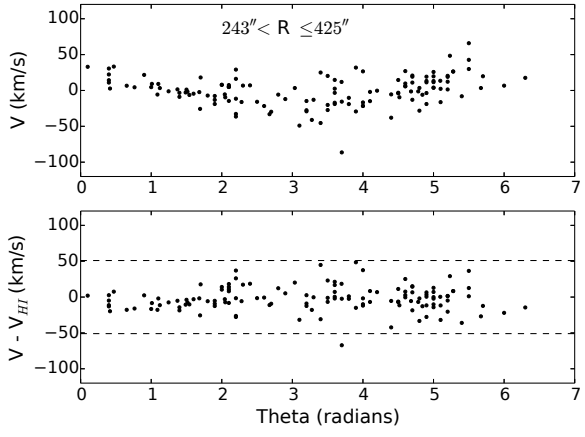

(c)

Figure 9. Velocity vs azimuthal angle plots in 3 radial bins, each with about 130 PNe. The angle θ is in the plane of the galaxy and measured from the line of nodes. The top panels show the velocity before correcting for galactic rotation and the bottom panels show the velocities after the THINGS HI velocities have been subtracted off. A few objects with velocity $> 3\sigma$ were removed from the sample. The objects within the dashed lines are the ones that were included in our sample for analysis. Each panel shows a cold population of spatially unresolved emission line objects, plus a hotter population whose velocity dispersion appears to decrease with galactic radius.

The subscript 1 and 2 refers to the components of the cold and hot populations respectively. The code then proceeds to calculate the probability of a particular v_{LOS} to be present at that azimuthal angle via the analytic equation:

$$P = \frac{N}{\sigma_{LOS1}\sqrt{2\pi}} \exp\left(\frac{-(v_{LOS} - \mu_1 \cos\theta.\sin i)^2}{2\sigma^2_{LOS1}}\right) + \frac{1-N}{\sigma_{LOS2}\sqrt{2\pi}} \exp\left(\frac{-(v_{LOS} - \mu_2 \cos\theta.\sin i)^2}{2\sigma^2_{LOS2}}\right) \quad (7)$$

In equation 7, N is the value of the fraction of the cold population returned by the routine that calculated σ_{LOS} described earlier. μ_1 and μ_2 were fixed at 0 km s^{-1} in our analysis. We tried to leave the two means as parameters to be estimated by the code, but since NGC 628 has such a low inclination, these parameters would not converge. It is difficult to get an estimate of the asymmetric drift in such a face-on galaxy. So we assumed that the mean of the cold PNe were at the same velocity as the gas, at 0 km s^{-1}. We did try changing the mean of the hot PNe up to an asymmetric drift of 5 km s^{-1} but this did not cause any significant changes in the σ_z values. Equation 7 is then maximised to return the best fit values for σ_z for the hot and cold population of PNe. The 1σ errors σ_z are calculated similar to the method used in the analysis of the VIRUS-W data. We carried out our monte carlo error estimation by using the double Gaussian distribution found by our MLE code, to pull out about 130 random velocities (i.e same number of objects as in each of our bins). The errors on the inclination and σ_z/σ_R were also incorporated as Gaussian distributions in the simulation. We then used this new sample to calculate the σ_z of the hot and cold component using our MLE routines. This whole process was repeated 1000 times, recording the dispersions returned in each iteration. The 1σ error is then the standard deviation of the distribution of the dispersions returned from these 1000 iterations.

The parameters returned from the MLE routine that does the double Gaussian decomposition is given in Table 5. Figure 10 shows the σ_z vs radius for NGC 628. The data points at a radius of 62″ and 109″ come from the VIRUS-W spectra in the inner field. Similar to the VIRUS-W analysis, we need to correct the dispersions for the PNe, because of the scatter in the the local THINGS HI velocity which we used to remove the galactic rotation. This correction was done as for the IFU data analysis by quadratically subtracting this small dispersion (~ 2.5 km s^{-1}) from the values of the dispersions returned by the MLE routine. We also need to correct the measured dispersions for the measuring errors of the individual PNe, as shown in Figure 3. The rms measuring error in each radial bin is about 6 km s^{-1}. The formal variance of the corrected cold dispersion value at a radius of 208″ is negative. Hence we show its 90% confidence upper limit in Figure 10 and Table 5.

The PNe population selected by the colour-magnitude cut (see section 3.2) includes a population of kinematically cold sources. If this cold component had not been present, Herrmann & Ciardullo (2009b) would probably have measured larger velocity dispersions and higher surface mass densities. From the analysis of the cold and hot PNe population, as well as the identified HII regions (Arnaboldi et al. 2017), the PNe near the bright cut-off of the PNLF are kinematically colder than the HII regions at the same m_{5007} magnitude, with $\sigma_{HII}/\sigma_{PNe} \sim 2$. Thus, these cold bright PNe are unlikely to be contaminant HII regions, since the LOS velocity distributions of the two classes of objects are so different. Work done by Miller Berto-

lami (2016) suggests that PNe from massive progenitors evolve very fast. Thus massive progenitors, i.e. young massive stars, produce bright PNe that are still kinematically very cold.

8 VERTICAL VELOCITY DISPERSION PROFILE

Figure 10 shows the results obtained from the integrated light VIRUS-W data (points at R = 62″ and 109″) and the planetary nebulae from the PN.S data (3 outer points) in each radial bin. At each radius, we show our one component dispersion, and then the hot and cold thin disc dispersion from our double Gaussian fit. The dispersions obtained from Herrmann & Ciardullo (2009b) are also plotted for comparison.

The black square markers in Figure 10 show the radial dependence of the dispersion for the hotter old component of the stars and PNe, measured as described in the previous section. If the total surface density of the disc follows an exponential decline with radius, and the scale height of the old disc is constant with radius (as we are assuming), then we expect the vertical velocity dispersion to fall with radius, following $\sigma_z(R) = \sigma_z(0)\exp(-R/2h_{\rm dyn})$, where $h_{\rm dyn}$ is the scale length for the total (old + young stars + gas) surface mass density of the disc. We note that the photometric scale length varies with the photometric band, and $h_{\rm dyn}$ need not be equal to any of the photometric scale lengths. A fit of the above equation for $\sigma_z(R)$ gives the mass scale length h_{dyn}, which is also the scale length that should be used for calculating the rotation curve of the exponential disc (see section 10). Our fit of $\sigma_z(R)$ is shown as the solid curve in Figure 10: we find that the central velocity dispersion of the old disc population is $\sigma_z(0) = 73.6 \pm 9.8$ km s^{-1} and the mass scale length $h_{dyn} = 92.7'' \pm 13.1''$, with significant covariance. The mass scale length is somewhat longer than the I-band scale length (Table 3), presumably because of the substantial contribution of the gas to the surface density at larger radii (see Table 6).

Figure 10 shows in red the PNe velocity dispersions derived for this galaxy by Herrmann & Ciardullo (2009b). Our one-component PNe velocity dispersions agree well with their results. We note that the difference between the one component dispersions and our hot component dispersions decreases with radius and is quite small for our outermost radial bin. This is consistent with the BIC values shown for the outer radial bin, which does not favour the two component model in the outer bin. The one component value for the last bin is also closer to our exponential disc curve than the two component value.

Mean Radius (arcsec)	2 component Model			1 Component Model	
	$\sigma_{z,cold}$ (km s^{-1})	$\sigma_{z,hot}$ (km s^{-1})	BIC	σ_z (km s^{-1})	BIC
132	4.6 ± 1.6	33.8 ± 3.3	1269	26.5 ± 1.8	1272
208	$\leqslant$ 6.7 ± 0.4	22.6 ± 2.1	1160	18.6 ± 1.3	1164
293	6.2 ± 1.7	17.5 ± 2.6	1124	14.5 ± 1.0	1118

Table 5. The σ_z values calculated from the PN.S data. We give the 90% confidence upper limit for the cold dispersion in the second radial bin (see section 4.2.3 for details). The lower BIC values of the two component fit (except in the outermost radial bin) make it the preferred model over the one component model.

Having calculated the σ_z in each radial bin in NGC 628, we can now proceed to calculate the surface mass density Σ of the disc using equation 2.

We now compare our results for the surface density of the disc, using a two-component (hot and cold) disc model, with the single-component analysis of Herrmann & Ciardullo (2009b). Herrmann & Ciardullo (2009b) adopted an intermediate vertical density distribution for their disc, with the geometric factor f in equation 1 to be equal to $1/1.705\pi$. We adopt an isothermal model as described in Appendix A. A simple isothermal model with no additional cold layer has the $sech^2(z/2h_z)$ vertical density distribution. This distribution is exponential at large z and flat near $z = 0$. In the presence of a significant cold layer, the $sech^2$ distribution is offset from zero, as shown in equation A7. For very small values, the offset parameter $b \sim \Sigma_C/\Sigma_T$ (this is true for our two inner radii). With a realistic surface density of kinematically cold gas and stars, the vertical distribution in equation A7 becomes close to exponential throughout. This effect is demonstrated in Figure 11 where we adopt an offset parameter of 0.5 and compare the sech^2 distribution with and without taking into account this offset. The offset distribution is close to an exponential beyond a height of $\sim$ 200 pc. This compares well with the study by Wainscoat et al. (1989) who found that the vertical surface brightness distribution of edge-on spirals in the NIR is close to exponential.

Using our scale height value $h_z = 397.6 \pm 88.3$ pc (see Table 3), which is almost the same as the value adopted by Herrmann & Ciardullo (2009b), and our $\sigma_z(0) = 73.6 \pm 9.8$ km s^{-1} for the hot component, our total central surface mass density is $\Sigma(0) = 505 \pm 175$ M$_\odot$ pc^{-2}. This is a factor of 1.7× larger than the value calculated by Herrmann & Ciardullo (2009b). Note that we use an isothermal model of the vertical distribution as opposed to the intermediate model dopted by Herrmann & Ciardullo (2009b). Using the central surface brightness and scale lengths from Möllenhoff (2004) and Salo et al. (2015), we calculate the central luminosity of NGC 628 in units of L$_\odot$pc^{-2}. This is corrected for foreground extinction using Schlafly & Finkbeiner (2011) dust maps. Our central surface mass density divided by the calculated central luminosity gives the central M/L in various photometric bands. The M/L in the R band is found to be 2.0 ± 0.7, about 1.4× larger than the value of 1.4 ± 0.3 obtained by Herrmann & Ciardullo (2009b). Photometric errors of 5% have been included in the error estimate (Möllenhoff 2004; Muñoz-Mateos et al. 2013).

9 STELLAR SURFACE MASS DENSITY

9.1 Isothermal model including cold component

The equilibrium of the hot disc is determined by its own gravitational field plus the gravitational field of the cold layer (gas and young stars) which we can consider as external fields. The presence of these external fields changes the vertical structure of the old disc and affects the derived surface density and M/L values for the old disc. We discuss this in more detail in Appendix A. We therefore use equation 2: $\sigma_z^2 = 2\pi G h_z \Sigma_T = 2\pi G h_z(\Sigma_C + \Sigma_D)$ to determine the surface mass density of the disc. We use the old disc population as a tracer of Σ_T, which is the parameter that determines the baryonic rotation curve.

The thin cold layer comprises gas and young stars, which we write as $\Sigma_C = \Sigma_{C,\rm gas} + \Sigma_{C,*}$ where $\Sigma_{C,\rm gas}$ is known directly from radio observations of the THINGS survey (Walter et al. 2008) and the HERACLES survey (Leroy et al. 2009) as discussed in section 6. The stellar contribution $\Sigma_{C,*}$ is not known directly from our data. In the following section, we estimate the

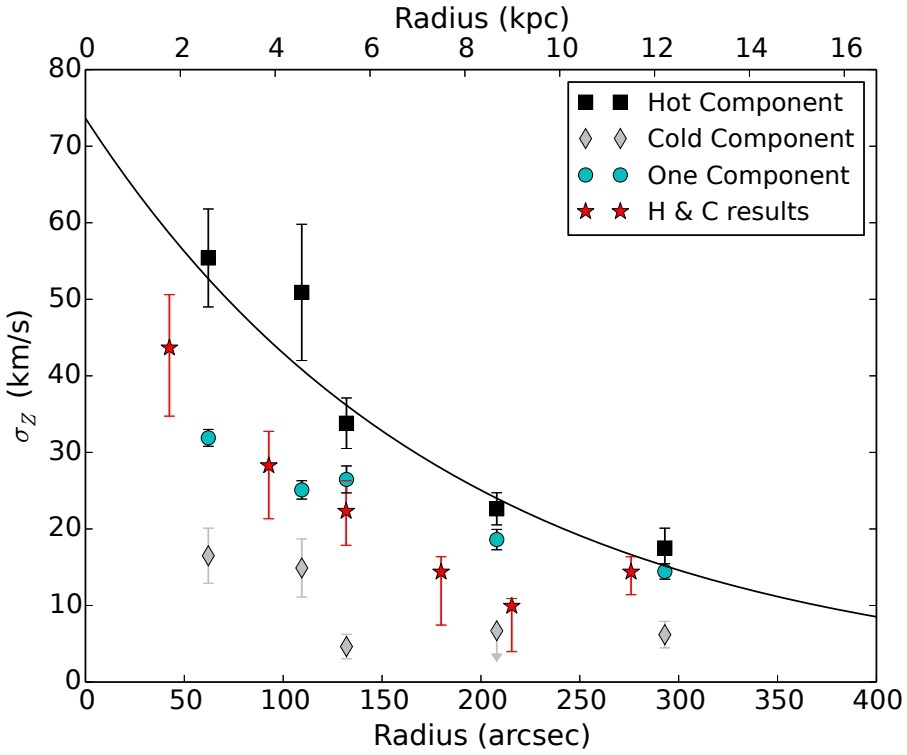

Figure 10. The σ_z per radial bin in NGC 628. The black and grey markers indicate the hot and cold velocity dispersions respectively from our two component fits, the cyan markers are our single-component values, and the points in red are the Herrmann & Ciardullo (2009b) PNe data. The data points at $R = 62''$ and $109''$ were obtained for integrated light spectra from VIRUS-W and the outer data points are for PNe from PN.S. The solid line denotes an exponential with twice the galaxy's dynamical scale length, fit to the hot component. Our data have been corrected for the HI velocity dispersion and PNe velocity errors (see section 4.2.3 for more details). The errors bars are the 1σ errors obtained from monte carlo simulations.

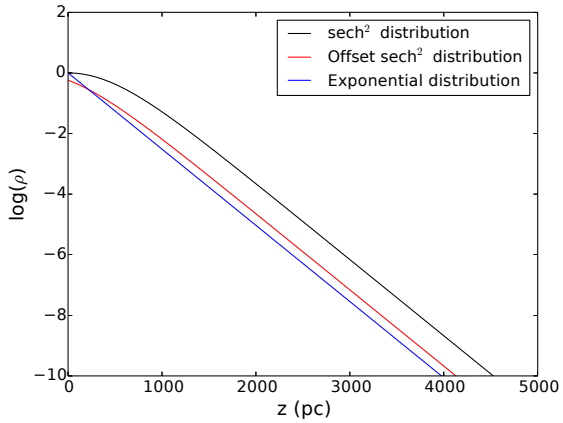

Figure 11. An illustration of a sech^2 distribution (in red) with an offset parameter of 0.5, taking into account the contribution from the cold layer of gas and young stars. It is identical to an exponential profile (shown in blue) beyond z ~ 200 pc. A sech^2 distribution without any offset is shown in black for comparison.

effect of the cold gas layer at the five radii in NGC 628 (2.6 kpc to 12.2 kpc) where we have velocity dispersion data.

From equation A10 in the appendix, the velocity dispersion of the isothermal sheet is $\sigma_z^2 = 2\pi G h_z(\Sigma_C + \Sigma_D)$. The adopted scale height $h_z = 398 \pm 88$ pc (see section 4). If h_z is constant with radius, the radial variation of σ_z^2 will follow the total surface density rather than the surface density of the isothermal sheet. In NGC 628, the gas fraction of the total surface density is significant at larger radii (Table 6).

9.1.1 The surface density of the cold stellar sheet

Our goal is to calculate the rotation curve contribution from the baryons in the disc. Assuming that the disc is a hot isothermal stellar layer Σ_D plus a thin young cold layer Σ_C, we measure the total surface density $\Sigma_T = \Sigma_C + \Sigma_D$. The cold layer Σ_C is made up partly of the gas sheet and partly of the thin young stellar disc. The cold stellar layer is thin, and the hot stellar layer is thicker, and their shape affects the calculated rotation curve. This is a second order effect, but it would be useful to know both of the stellar surface densities Σ_D and $\Sigma_{C,*}$.

The velocity dispersion analysis gives the total surface density

$$\Sigma_T = \Sigma_D + \Sigma_{C,\mathrm{gas}} + \Sigma_{C,*}$$

of the disc. We can make an estimate of the ratio of cold to hot stellar contributions $\Sigma_{C,*}/\Sigma_D$ from our IFU study in the inner parts of NGC 628 which gives the fraction of light that comes from the two stellar components. Their M/L ratios need to be estimated from stellar population synthesis. In the outer regions, the PNe analysis gives the fraction of cold emission-line objects, but deriving the fractional mass of the underlying cold stellar population is uncertain because (a) of possible contamination of the sample by HII regions, and (b) the young PNe have

more massive progenitors, and the lifetimes in the PNe phase are very strongly dependent on their progenitor masses (e.g. Miller Bertolami 2016).

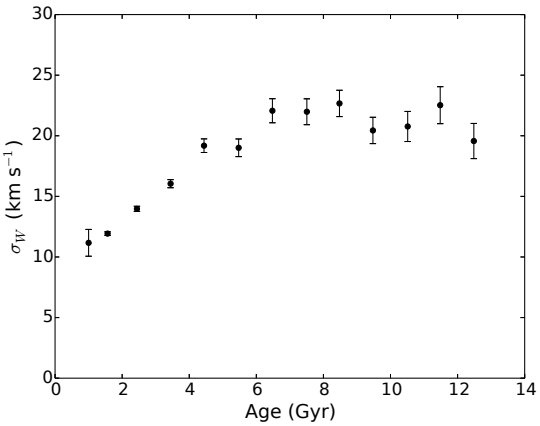

Figure 12. Vertical velocity dispersion σ_W *vs* stellar age for the solar neighbourhood, for stars with [Fe/H] > −0.3; data from Casagrande et al. (2011).

Our IFU study analysed the integrated light spectrum as the sum of two velocity components (hot and cold, or young and old), without specifying the age range of either component. The age range is needed to calculate their M/L ratios, and we estimate the age ranges from the observed age-velocity dispersion relation (AVR) in the solar neighbourhood. Figure 12 shows the vertical velocity dispersion σ_W *vs* age for the solar neighbourhood Casagrande et al. (2011) stars from the Geneva Copenhagen survey. In order to exclude most thick disc stars, Figure 12 includes only stars with [Fe/H] > −0.3. The dispersion rises from about 10 km s^{-1} for ages < 1 Gyr to about 20 km s^{-1} at 4 Gyr and then remains approximately constant. If the AVR in NGC 628 has a similar shape, then the cold stellar component would be made up of stars younger than about 3 Gyr.

The (cold, hot) component contributions to the integrated light spectrum shown in Figure 7 (close to the V-band) are given as percentages L_C/L_D in the first two rows of Table 6. From Bruzual & Charlot (2003), we compute the expected $(M/L)_V$ ratios for populations younger and older than 3 Gyr, assuming a disc age of 12 Gyr and a star formation rate that decays with time like $\exp(-t/\tau)$. For $\tau > 3$ Gyr, the M/L ratios for the young and old populations vary with τ almost in lockstep, and the ratio $F_C = \Sigma_{C,*}/\Sigma_D$ is about 0.12, almost independent of τ. The surface densities of the stellar disc components are then

$$\Sigma_D = \frac{\Sigma_T - \Sigma_{C,\mathrm{gas}}}{1 + F_C} \quad \text{and} \quad \Sigma_{C,*} = F_C\,\Sigma_D. \tag{8}$$

In the first two rows of Table 6, we use values of F_C derived from the (cold, hot) component contributions to the integrated light spectrum as described above. In the following rows, where the velocity dispersions come from PNe, we adopt the mean value of 0.12 for F_C from the integrated light spectra. Table 6 gives F_C, Σ_D, $\Sigma_{C,*}$ and finally the $(M/L)_V$ ratio for the stellar component at each radius i.e $(\Sigma_D + \Sigma_{c,*})$/L. We can compare the observed values of $(M/L)_V$ with those calculated from the Bruzual & Charlot (2003) models. The calculated $(M/L)_V$ is in the range 2.3 to 2.9 for the star formation rate parameter $\tau > 3$ Gyr, in fair agreement with our values in Table 6 for the stellar disc of NGC 628. The weighted mean of our $(M/L)_{3.6}$ values from Table 6 is 0.75 ± 0.18. This value is similar to the disc stellar $(M/L)_{3.6} \sim 0.6$ obtained from population synthesis studies (Meidt et al. 2014; Norris et al. 2014).

10 ROTATION CURVE DECOMPOSITION

10.1 Observed HI rotation curve

Obtaining the rotation curve of a near-face-on galaxy, such as NGC 628, is challenging. The uncertainty associated with the inclination is substantial and is the main contributor to the error budget of the rotational velocity. Therefore, we approach this task in several steps. First, we estimate an approximate value for the average inclination angle by placing this galaxy on the 3.6 μm Tully-Fisher relation from Ponomareva et al. (2017). This gives us an initial guess of the inclination angle = 9°.

We then use the HI data for NGC 628 from the THINGS survey (Walter et al. 2008) to get the rotation curve for this galaxy. After smoothing and masking the original data cube, we constructed a velocity field by fitting a Gauss-Hermite polynomial to the velocity profiles. This velocity field is corrected for the skewness of the profiles, in order to remove non-circular motions, using the technique described in Ponomareva et al. (2016). We then derive the rotation curve from the velocity field by fitting a tilted-ring model (Begeman 1989), using the Groningen Imaging Processing System (Gipsy, Van der Hulst et al. 1992). During the tilted ring modelling, we account for the outer warp of the disc, which can be clearly seen in the upper panel in Figure 13 (see Mulcahy et al. 2017). We find the average inclination across all radii to be 8.5° ± 0.2° (Figure 13, middle panel). We derive the rotation curve of the galaxy by keeping the inclination fixed at this value. The resulting rotation curve is presented in the bottom panel of Figure 13, with red and blue curves indicating the receding and approaching sides of the galaxy respectively. We adopt the difference between the receding and approaching sides as the 1σ error in the measured rotational velocity. The full error in the rotational velocity was calculated by also taking into account the uncertainty in the inclination.

We now proceed to calculate the contribution to the observed rotation curve from the gas. An integrated column–density HI map was created by summing the primary beam-corrected channels of the clean data cube. The radial surface density profile is then derived by averaging the pixel values in the concentric ellipses projected on to the HI map. We use the same radial sampling, position and inclination as those for the rotation curve derivation.

The column density profile was then corrected for the presence of helium and metals by multiplying the measured densities by 1.4. The Gipsy task ROTMOD was used to compute the corresponding rotation curve assuming an infinitely thin exponential gas disc. In addition to the atomic gas, we also adopt the CO data from Leroy et al. (2009) to derive the rotational velocity for the molecular gas (see section 6 for details).

10.2 Stellar Distribution

One of the largest sources of uncertainty for the mass modelling is the stellar disc mass, which usually depends on the adopted

Instrument	R	Colour	σ_z	Σ_T	$\Sigma_{C,\mathrm{gas}}$	b	L_C/L_D	F_C	Σ_D	$\Sigma_{C,*}$	$(M/L)_B$	$(M/L)_V$	$(M/L)_R$	$(M/L)_I$	$(M/L)_{3.6}$
	(kpc)	B-I	(km s^{-1})	($M_\odot$ pc^{-2})	($M_\odot$ pc^{-2})				($M_\odot$ pc^{-2})	($M_\odot$ pc^{-2})					
(1)	(2)	(3)	(4)	(5)	(6)	(7)	(8)	(9)	(10)	(11)	(12)	(13)	(14)	(15)	(16)
VIRUS-W	2.6	1.82	55.4 ± 6.4	286 ± 92	34 ± 3	0.22 ± 0.09	44/56	0.13	223 ± 82	29 ± 11	2.5 ± 0.9	2.3 ± 0.9	2.3 ± 0.9	1.9 ± 0.7	0.8 ± 0.3
VIRUS-W	4.5	1.70	50.9 ± 8.9	241 ± 100	34 ± 3	0.23 ± 0.11	40/60	0.11	187 ± 90	21 ± 10	3.5 ± 1.7	3.3 ± 1.6	3.5 ± 1.7	2.9 ± 1.4	1.2 ± 0.6
PN.S	5.5	1.64	33.8 ± 3.3	106 ± 31	36 ± 3	0.44 ± 0.16	42/58	0.12	63 ± 28	8 ± 3	1.5 ± 0.7	1.5 ± 0.7	1.6 ± 0.7	1.4 ± 0.6	0.6 ± 0.3
PN.S	8.7	1.44	22.6 ± 2.1	48 ± 14	25 ± 3	0.68 ± 0.29	42/58	0.12	21 ± 13	3 ± 2	1.2 ± 0.7	1.2 ± 0.8	1.4 ± 0.9	1.3 ± 0.8	0.6 ± 0.4
PN.S	12.2	1.22	17.5 ± 2.6	29 ± 11	14 ± 2	0.64 ± 0.32	42/58	0.12	13 ± 10	2 ± 1	2.0 ± 1.5	2.3 ± 1.7	2.8 ± 2.2	2.6 ± 2.0	1.3 ± 0.9

Table 6. Parameters for NGC 628 at the five radii where the velocity dispersion of the hot disc was measured (inner two radii from integrated light, outer three from PNe). All surface densities are in units of $M_\odot$ pc^{-2}. The columns are (1) instruments used, (2) radius, (3) B - I colour from Möllenhoff (2004) (4) vertical velocity dispersion σ_z of the hot disc, (5) total surface density Σ_T from equation A10 in the appendix, (6) observed surface density $\Sigma_{C,\mathrm{gas}}$ of the gas layer from the THINGS & HERACLES survey, (7) the offset parameter b from equation A5 in the appendix, (8) ratio of luminosities of cold and hot layers from the integrated spectra in rows 1 and 2, and adopting the mean of rows 1 and 2 in rows 3 to 5, (9) the ratio F_C of the stellar surface densities of the cold and hot layers, (10) the surface density Σ_D of the hot layer from equations 8, (11) the stellar surface density $\Sigma_{C,*}$ of the cold stellar layer, (12) – (16) the foreground extinction corrected M/L ratio of the total stellar component in BVRI bands from Möllenhoff (2004) and the 3.6 μm band from Salo et al. (2015).

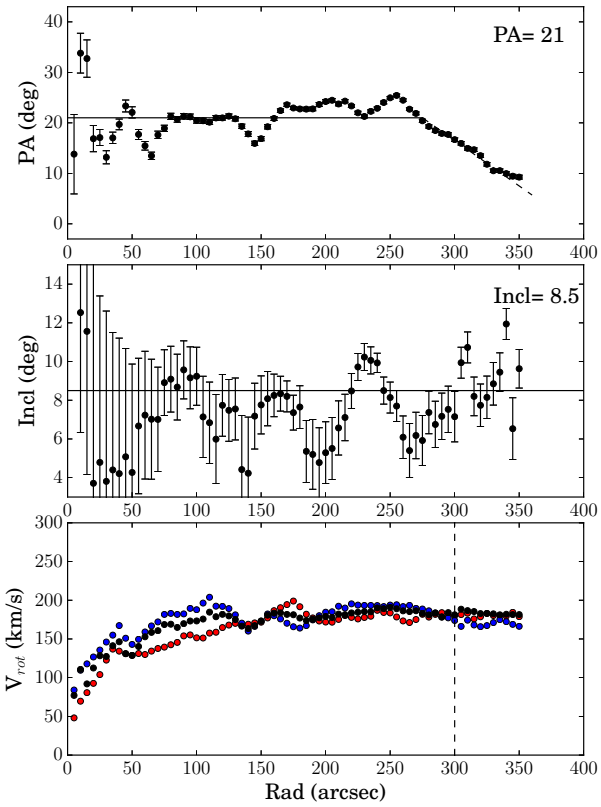

Figure 13. The results of the tilted-ring modelling for NGC 628. Upper panel: position angle as a function of radius. The outer warp is modelled beyond 250″. Middle panel: inclination angle as a function of radius. The mean value of 8° is adopted for our analysis. Bottom panel: observed HI rotation curve is shown in black. The red and blue curves show the velocity of the receding and approaching sides of the galaxy respectively. The dashed vertical line indicates the optical radius.

M/L. However, for NGC 628 we have measured the surface density of the stellar component directly. We measured the dynamical scale length for the total surface mass density Σ_T (see section 8). This included the cold and hot stellar disc as well as the gas disc. However, we do not have a handle on the scale height of the total baryonic disc component represented by Σ_T. The adopted scale height of 398 pc is for the old disc component. The scale height of Σ_T will be some combination of the scale heights of the cold and hot component. In order to test the effect of various scale heights on the rotation curve decomposition, we adopted a range of scale heights from 100 – 400 pc. Figure 14 shows the effect of the scale heights on the rotation curve of the baryonic component.

As discussed in section 4, a small bulge component is present in NGC 628 (Muñoz-Mateos et al. 2013). While the total bulge light contributes only 6.5% to the total light of the galaxy, the bulge light dominates within the central 1.5 kpc and, therefore, we need to include it in our mass modelling. We convert the 3.6 μm bulge surface brightness from Salo et al. (2015) into the surface mass density using the stellar M/L for 3.6 μm = 0.6 (Meidt et al. 2012; Querejeta et al. 2015; Röck et al. 2015) and $M_{\odot}(3.6\ \mu m) = 3.24$ mag (Oh et al. 2008). We model the bulge using the same Gipsy task ROTMOD assuming a spherical potential. The rotation curves of all the baryonic components were modelled with the same sampling as was used for the derivation of the observed rotation curve.

Figure 14 shows the observed rotation curve in black. The dashed curves in various colours are the bulge + the central total surface mass density with a dynamical scale length (h_{dyn} = 92.7″) fit as an exponential disc with varying scale heights. We note that a difference of 100 pc in scale height only changes the peak of the rotational velocity of the baryonic component (V_{max}) by 1 km s^{-1}. Thus the adopted scale height has a negligible effect on the rotation curve decomposition.

10.3 Mass modelling

The total rotational velocity of a spiral galaxy can be calculated using the relation:

$$V_{tot}^2 = V_{bar}^2 + V_{halo}^2, \quad (9)$$

where V_{bar} is the circular velocity associated with the gravitational field of the total baryonic content: cold disc+hot disc+gas, and V_{halo} is the circular velocity for the dark halo. As the observed HI rotation curve (V_{obs}) traces the total gravitational potential of a galaxy, we can derive the rotation curve of the dark matter halo by fitting various parameters until V_{tot} matches V_{obs} as closely as possible. Moreover, for this galaxy, we have an independently measured surface density distribution for the stellar disc components, so we do not have the usual unconstrained stellar M/L. This allows us to fix the baryonic rotation curve and only fit the rotation curve of the dark matter halo. This breaks the usual disc-halo degeneracy and allows us to test the maximality of the disc directly.

For our analysis we use two models of the dark matter rotation curves: spherical pISO (pseudo isothermal) and NFW-halo. The pISO halo has a central core and is parameterised by its central density (ρ_0) and the radius of the core (R_c). Its rotation curve is given by:

$$V_{DM}^{pISO}(R) = \sqrt{4\pi G\rho_0 R_C^2\Big[1 - \frac{R_C}{R}tan^{-1}\Big(\frac{R}{R_C}\Big)\Big]} \quad (10)$$

The NFW halo (Navarro et al. 1997) is parameterised by its mass (M_{200}) within the viral radius (R_{200}) and its concentration (c). Its rotation curve is given by:

$$V_{DM}^{NFW}(R) = V_{200}\Big[\frac{ln(1+cx) - cx/(1+cx)}{x[ln(1+c) - c/(1+c)]}\Big]^{1/2} \quad (11)$$

where $x = R/R_{200}$ and V_{200} is the circular velocity at R_{200}.

Equations 10 and 11 describe the circular velocity distribution of the dark halo as it is now, modelled by the two particular models which we are using (pISO and NFW). The state of the dark halo now is almost certainly very different from what it was like before the baryons condensed to form the disc. Based on the present understanding of the formation of the dark halo, it probably formed with a density cusp as seen in almost all N-body simulations (e.g. Navarro et al. 2010). Cusped haloes are however rarely observed in disc galaxies at low redshift (e.g. Oh et al. 2011). Their absence is usually interpreted as the effect of feedback from rapid star formation as the stellar disc is forming (e.g. Brook et al. 2011), which transforms the inner cusps into the approximately flat cores that are observed.

In addition to this major restructuring of the dark haloes, many authors have considered the effect of slow (adiabatic) formation of the disc and bulge on the large scale structure of the dark halo. Blumenthal et al. (1986) proposed a simple method

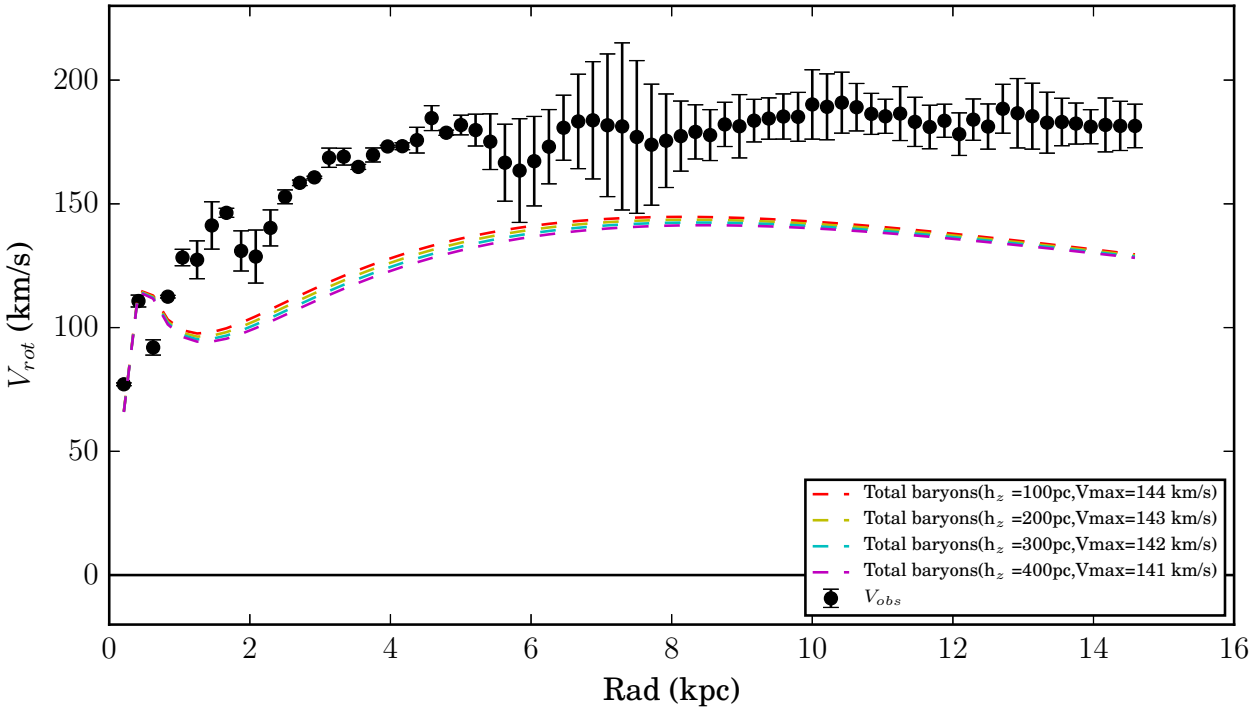

Figure 14. The effect of the scale height on the rotation curve decomposition. The black data points are the observed HI rotation curve from the THINGS survey. The coloured dashed lines are the total baryonic rotation curve assuming scale heights of 100 – 400 pc. A difference of 100 pc in the scale height results in a 1 km s^{-1}change in the peak of the baryonic rotation.

for calculating the restructuring of the dark halo under adiabatic contraction of the disc and bulge, based on the adiabatic invariance of the angular momentum of dark matter particles. Subsequent works have argued that this simple method overestimates the readjustment of the halo relative to calculations in which the other adiabatic invariants are also included (Wilson 2003; Gnedin et al. 2004; Jesseit et al. 2002). Abadi et al. (2010) use N-body simulations and find that the halo contraction is less pronounced than found in earlier simulations, a disagreement which suggests that halo contraction is not solely a function of the initial and final distribution of baryons. Wegg et al. (2016) compared the dark halo rotation curves of the Milky Way obtained from the MOA-II microlensing data (see their Figure 12). They find that the adiabatically contracted halo according to the classical Blumenthal et al. (1986) prescription is inconsistent with the revised MOA-II data at the 1σ level. The prescription of Gnedin et al. (2004) is consistent only if the initial halo has low concentrations (see Wegg et al. 2016 for details).

The evolution of dark haloes is not simple. We have briefly discussed cusp-core transformation, which probably occurs during the strong star formation around $z = 2$ to 3. Adiabatic contraction, if it is significant, is presumably an extended process that goes on throughout the growth of the disc. Furthermore, cosmological simulations indicate that haloes continue to grow by accretion up to the present time, with typically half or more of their mass growth taking place since $z = 1$ (Muñoz-Cuartas et al. 2011). While we can measure the basic parameters of dark haloes at the present time, as described in this paper, we do not see an obvious earlier stage at which one would want to identify a pristine dark halo and estimate its parameters from its present state. We do not therefore attempt to go beyond our initial goal, of determining the decomposition of the rotation curve of galaxies into the contributions from the disc and dark halo at the present time.

The Gipsy task ROTMAS was again used to find the rotation curves for the dark haloes. We ran the models for each of the two dark matter haloes separately, keeping the rotation curves of the total baryonic component fixed. As demonstrated in the previous section, the scale height makes a negligible contribution to the rotation curve decomposition. We therefore fit an exponential with $\Sigma_T(0) = 505 \pm 175$ M$_\odot$pc^{-2} and (dynamical) scale length = 92.7″ along with a scale height = 397.6 pc (this is our adopted scale height for the hot stellar disc). The results from this modelling are presented in Figure 15 (the top panel is for the pISO halo and the bottom panel for the NFW halo). Although the rotation curves for the two haloes have a similar shape, the pISO halo works marginally better in our case with a $\chi^2_{red} = 1.17$ compared to a $\chi^2_{red} = 1.21$ for the NFW halo.

There is a significant negative covariance between the h_{dyn} and the $\sigma_z(0)$. Taking our $\sigma_z(0)$ in units of km s^{-1}and h_{dyn} in units of arcsecs, the cov($\sigma_z(0)$, h_{dyn}) = −118.12. The fractional error on the peak of the baryonic rotation curve can be calculated as:

$$\left(\frac{\Delta \mathrm{V_{baryonic}}}{\mathrm{V_{baryonic}}}\right)^2 = \left(\frac{\Delta\sigma_z(0)}{\sigma_z(0)}\right)^2 + 0.25\left(\frac{\Delta h_{dyn}}{h_{dyn}}\right)^2 + 0.25\left(\frac{\Delta h_z}{h_z}\right)^2 + \frac{\mathrm{cov}(\sigma_z(0), h_{dyn})}{\sigma_z(0).h_{dyn}}$$

where the Δ terms represent the errors on the respective values. The corresponding values for our data are:

$$\left(\frac{\Delta V_{\rm baryonic}}{V_{\rm baryonic}}\right)^2 = 0.018 + 0.005 + 0.012 - 0.017$$

This gives us a 13% error on the peak of the baryonic rotation curve. Therefore, our estimated $V_{\rm baryonic} = 141.0 \pm 18.8$ km s^{-1} and $V_{max} = 180 \pm 9$ km s^{-1}(from our observed rotation curve). Taking into account the covariance between the terms, we find our disc to be maximal with $V_{\rm baryonic} = (0.78 \pm 0.11)V_{max}$. We note that the M/L for the bulge component remains at 0.6 even when the bulge rotation curve was not constrained to this value. The derived parameters of the fitted dark matter rotation curves are presented in Table 7. We note that the scale length derived for the pISO model is rather short for a luminous galaxy such as NGC 628 (Kormendy & Freeman 2016). The error on the total rotational velocity (blue curve in Figure 15) follows from the error on the central surface density described in section 5.

pISO			NFW		
R_C (kpc)	ρ_0 (10^{-3} M$_\odot$pc^{-3})	χ^2_{red}	C	R_{200} (kpc)	χ^2_{red}
0.69 ± 0.09	642.9 ± 159.8	1.17	25.1 ± 2.1	117.2 ± 4.1	1.21

Table 7. The derived parameters of the fitted dark matter haloes from the mass modelling.

The derived dark halo parameters for the pseudo isothermal and NFW models have significant covariance. This is demonstrated using the χ^2 maps of the 2D parameter space as shown in Figure 16. The coloured ellipses in each panel represent the 1σ to 5σ values from inside to outside. The errors quoted in Table 7 are the 1σ values.

For the purpose of the rotation curve analysis shown in Figure 15, we simply needed the radial distribution of the total baryon surface density Σ_T. It may however be of interest for the reader to see how each of the components of Σ_T contributes to the rotation curve. We are able to derive the radial surface density distributions separately for the hot and cold stellar discs, as described in section 9.1.1, although extra errors are introduced in the process. The surface density distribution of the gas is observed directly.

The dynamical scale length derived from Figure 10 refers to the total baryonic surface density of the disc of NGC 628. To demonstrate the contribution of the individual components to the rotation curve, we need to estimate their scale lengths. Figure 17 shows our Σ_D and $\Sigma_{C,*}$ radial distributions from Table 6. Fitting exponential profiles to these distributions gives an estimate of the scale lengths for the hot and cold stellar components as $\sim 65'' \pm 17''$. The errors are relatively large, as we have only five points on each profile. We note that the two stellar components are expected to have equal scale lengths, from the way in which they were derived; see equation 8.

Figure 18 shows the contribution of the various baryonic components to the rotation curve. We stress that this figure is for the purpose of illustration only, and that our adopted parameters for the individual stellar components have large errors, as explained above. In Figure 18 the green dot dashed line represents the rotational velocity of the atomic + molecular gas, using data from the THINGS and HERACLES surveys (Walter et al. 2008; Leroy et al. 2009). The red dot-dashed line is the bulge component. The blue and red dashed line represent the cold and hot stellar disc respectively. The purple curve with error bars is the total baryonic rotational velocity. This is a bit different from the corresponding curve in Figure 15 due to the significant errors involved in deriving the parameters of the hot and cold stellar discs individually.

11 CONCLUSIONS

The disc-(dark halo) degeneracy in spiral galaxies has been an important problem in dark halo studies for several decades. One of the more direct methods of breaking this degeneracy is by measuring the surface mass density of the disc and hence its mass-to-light ratio, using the velocity dispersion and the estimated scale height of the disc. However, it is essential that the measured vertical velocity dispersion and the disc scale height pertain to the same stellar population.

In the disc of a typical star-forming spiral galaxy, the colder young stellar component provides a significant contribution to the number density of kinematical tracers like red giants and planetary nebulae which have stellar progenitors with a wide range of ages. Through its red giants, which are a significant contributor to the integrated light spectra that are used for velocity dispersion measurements, the colder young population can have a substantial influence on the observed vertical velocity dispersion of the disc.

The other observable, the scale height of the disc, is usually measured from red or near-IR surface photometry of edge-on galaxies, away from the central dust layer. The estimated scale heights are then close to the scale heights of the older disc population.

Using integrated light absorption line spectra and velocities for a large sample of PNe in the face-on disc galaxy NGC 628, we show that the velocity distribution of disc stars does indeed include a young kinematically cold population and an older kinematically hotter component. We argue that previous integrated light and PNe studies have underestimated the surface density and M/L ratio of discs because they were not able to account for the contribution from the younger colder disc population in their velocity dispersion analysis.

To estimate the surface density of the disc, using equation 2, we use the velocity dispersion σ_z of the older hotter component of the disc together with the old disc scale height h_z measured from red or near-IR photometry of edge-on spiral galaxies. Together, σ_z and h_z pertain to the same stellar population and act as consistent tracers of the total gravitational field of the baryonic disc (hot + cold stellar disc + gas disc). For NGC 628, this leads to a surface mass density that is ~ 2 times larger than the values derived from previous estimates of disc density from disc velocity dispersions. This factor agrees well with our earlier estimates for the solar neighbourhood (Aniyan et al. 2016), and is large enough to make the difference between concluding that a disc is maximal or sub-maximal.

We find that the observed vertical velocity dispersion of the hotter component follows an exponential radial decrease, as expected for an exponential disc of constant scale height. From the velocity dispersion distribution, we estimate a dynamical scale length and central total surface density for the disc, which are then used in the rotation curve modelling. In the presence of a thin cold layer of gas and young stars with surface density Σ_C, the density distribution of the hot isothermal layer has the form

$$\rho(z) = \frac{\sigma_z^2}{8\pi G h_z^2}\,\mathrm{sech}^2(|z|/2h_z + b)$$

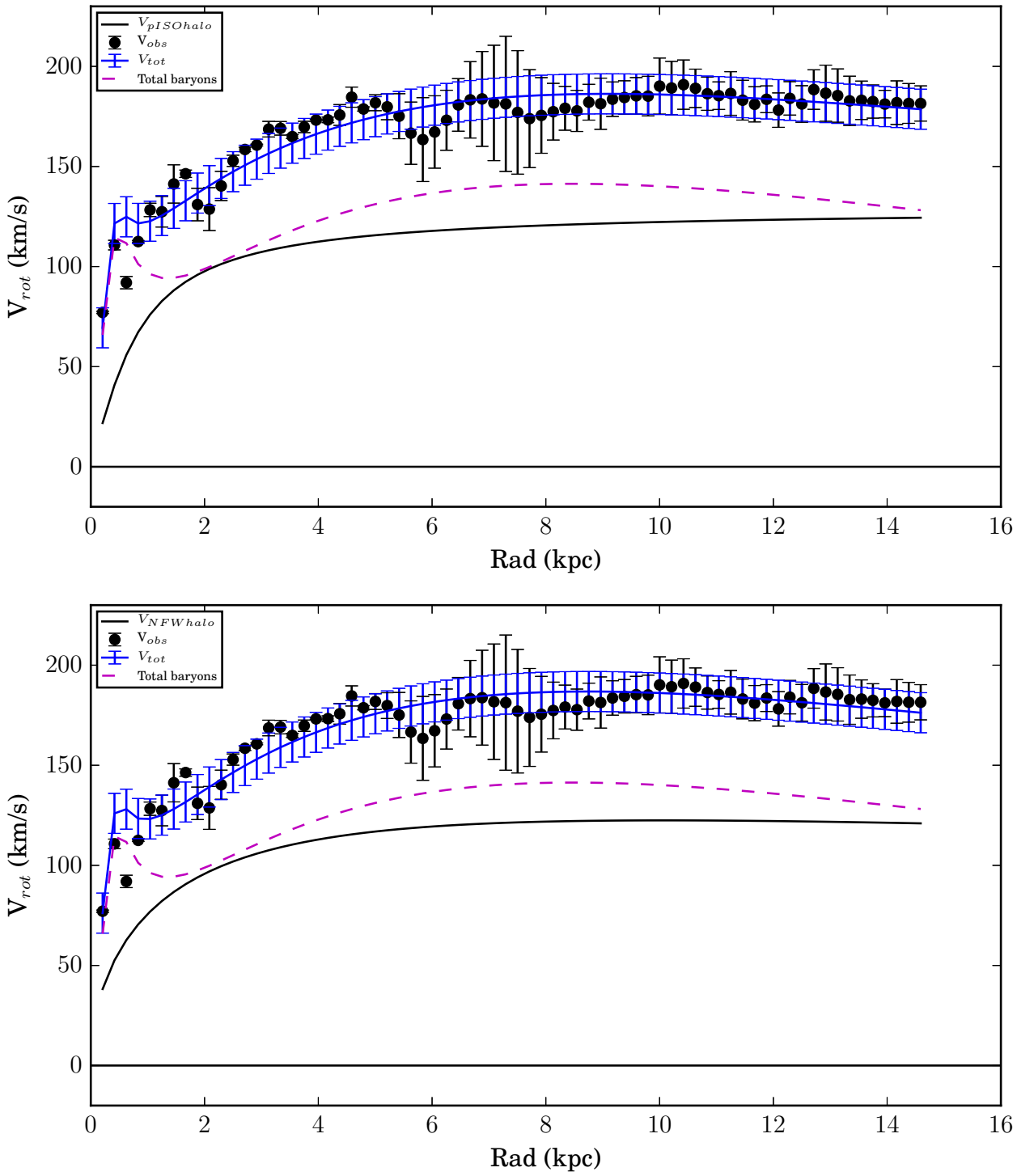

Figure 15. The rotation curve decomposition for NGC 628 by fitting a pISO halo (top panel) and a NFW halo (bottom panel). Observed HI rotation curve is shown as black dots. The magenta line represents the rotational velocity of all the baryons i.e the disc, gas, and the bulge. The black curve shows the rotation of the dark halo. This galaxy is clearly maximal demonstrated by the fact that the baryons are dominant in the inner parts of the galaxy.

where $\tanh(b) = 2\pi G h_z \Sigma_C/\sigma_z^2$. The total surface density is then $\Sigma_T = \Sigma_C + \Sigma_D = \sigma_z^2/2\pi G h_z^2$. We find that the ratio $F_c = \Sigma_{C,*}/\Sigma_D$ appears to be about 12% in the inner regions of of NGC 628, and our calculated M/L for the total stellar component (hot + cold) is approximately constant with radius.

Decomposing the rotation curve of this galaxy, after taking into account the hot and cold stellar components, leads to a maximal disc. The rotation of the baryonic component is ~ 78% of the total rotational velocity of this galaxy.

This is the first report from a larger study of nearby near-

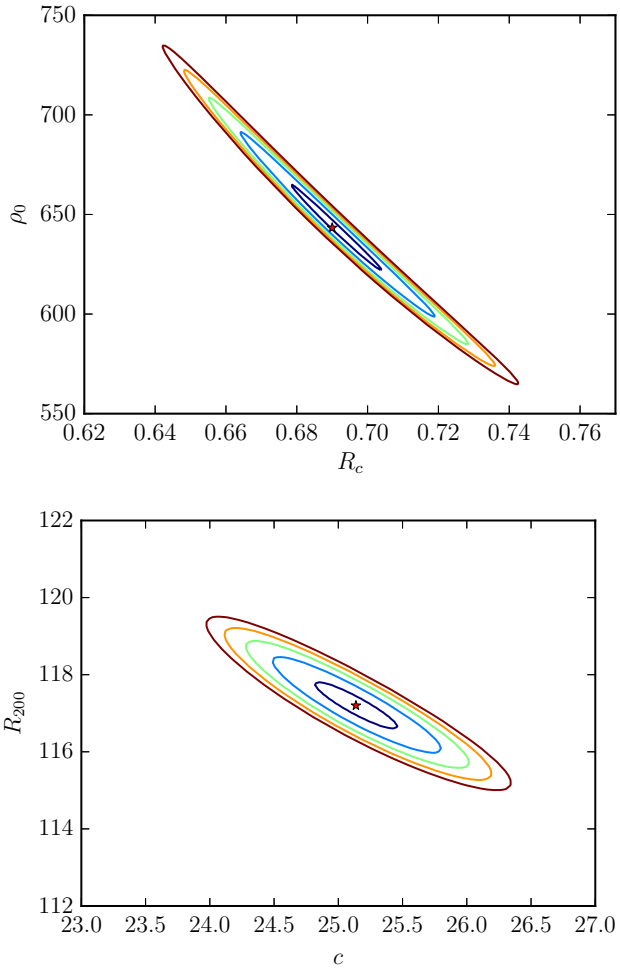

Figure 16. χ^2 map in the two dimensional parameter space for our derived dark halo parameters. The upper panel shows the covariance between the density and radius of the core of the pseudo isothermal model of the dark halo. The lower panel shows the covariance between the virial radius and concentration of the NFW dark halo model. The ellipses represent the $1\sigma - 5\sigma$ values from inside out.

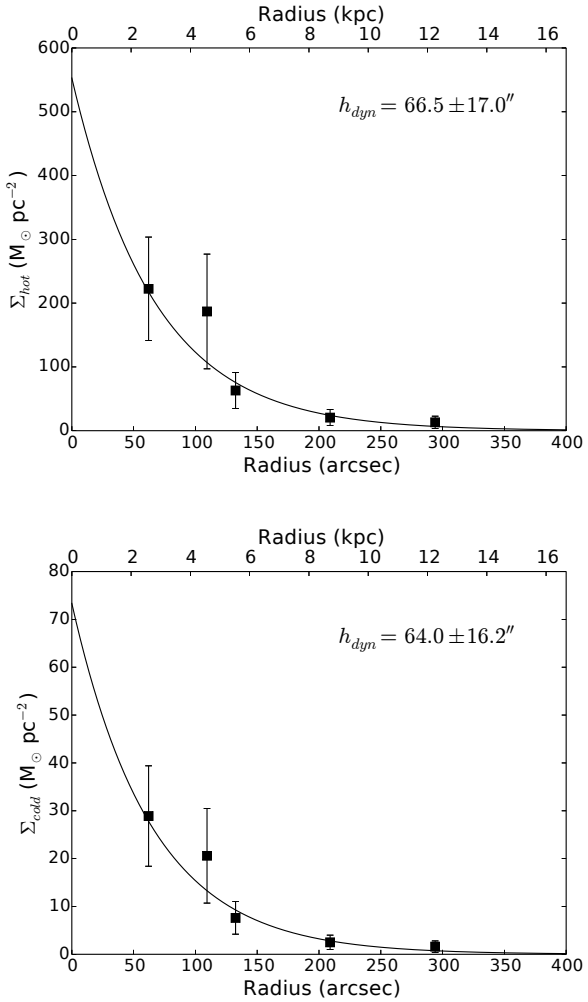

Figure 17. The surface mass density of our hot stellar component (upper panel) and cold stellar component (lower panel) to derive the dynamical scale length.

face-on spirals, using a combination of VIRUS-W data and PN.S data for 5 northern galaxies and data from the WiFeS IFU spectrograph for 3 southern galaxies. The analysis of these galaxies is currently underway.

12 ACKNOWLEDGEMENTS

The authors would like to thank the referee for the very detailed report that improved the quality of this paper. SA would like to thank ESO for the ESO studentship that helped support part of this work. KCF thanks Roberto Saglia, Marc Verheijen and Matt Bershady for helpful discussions on this project. KCF, MA, and OG acknowledge the support of the ARC Discovery Project grant DP150104129. The authors are very grateful to the staff at McDonald Observatory for granting us the observing time and support on the 107″ telescope. The authors would also like to thank the Isaac Newton Group staff on La Palma for supporting the PN.S over the years, and the Swiss National Science Foundation, the Kapteyn Institute, the University of Nottingham, and INAF for the construction and deployment of the Hα arm.

REFERENCES

Abadi M. G., Navarro J. F., Fardal M., Babul A., Steinmetz M., 2010, MNRAS, 407, 435
Aniyan S., Freeman K. C., Gerhard O. E., Arnaboldi M., Flynn C., 2016, MNRAS, 456, 1484
Arnaboldi M., Gerhard O., Aniyan S., Freeman K. C., PN.S collaboration 2017, in prep
Begeman K. G., 1989, A&A, 223, 47
Bershady M. A., Verheijen M. A. W., Swaters R. A., Andersen D. R., Westfall K. B., Martinsson T., 2010a, ApJ, 716, 198
Bershady M. A., Verheijen M. A. W., Westfall K. B., Andersen D. R., Swaters R. A., Martinsson T., 2010b, ApJ, 716, 234
Bershady M. A., Martinsson T. P. K., Verheijen M. A. W., Westfall K. B., Andersen D. R., Swaters R. A., 2011, ApJ, 739, L47
Bienaymé O., 1999, A&A, 341, 86
Bizyaev D., Mitronova S., 2002, A&A, 389, 795
Blumenthal G. R., Faber S. M., Flores R., Primack J. R., 1986, ApJ, 301, 27

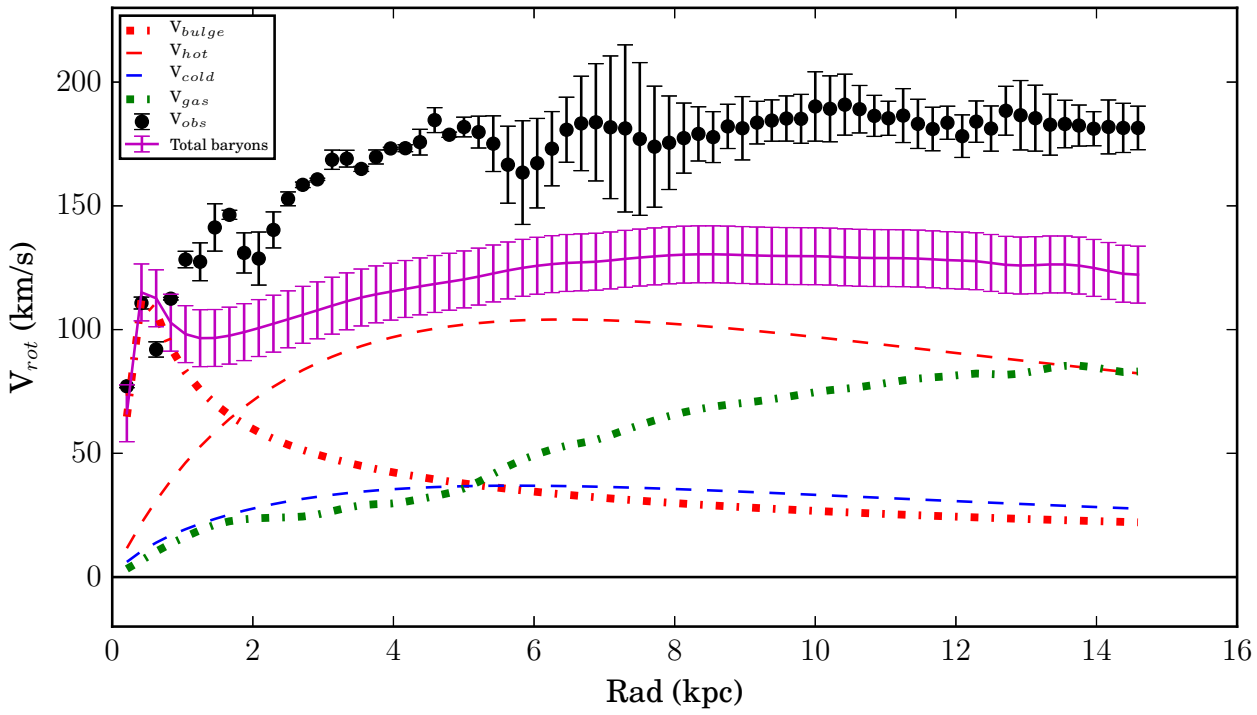

Figure 18. A demonstration of the contributions of the various baryonic components to the rotation velocity. The green dot dashed line represents the rotational velocity of the atomic + molecular gas, using data from the THINGS and HERACLES survey. The red dot dashed line is the bulge component. The blue and red dashed line represent the cold and hot stellar disc respectively. The purple curve is the total baryonic rotational velocity obtained by summing up each component in quadrature.

Bottema R., van der Kruit P. C., Freeman K. C., 1987, A&A, 178, 77
Brook C. B., et al., 2011, MNRAS, 415, 1051
Bruzual G., Charlot S., 2003, MNRAS, 344
Cappellari M., 2017, MNRAS, 466, 798
Cappellari M., Emsellem E., 2004, PASP, 116, 138
Casagrande L., Schönrich R., Asplund M., Cassisi S., Ramírez I., Meléndez J., Bensby T., Feltzing S., 2011, A&A, 530, A138
Coccato L., et al., 2009, MNRAS, 394, 1249
Coccato L., Morelli L., Corsini E. M., Buson L., Pizzella A., Vergani D., Bertola F., 2011, MNRAS, 412, L113
Conroy C., 2013, ARA&A, 51, 393
Conroy C., Gunn J. E., White M., 2009, ApJ, 699, 486
Cortesi A., et al., 2013, A&A, 549, A115
Courteau S., Dutton A. A., 2015, ApJL, 801, L20
Courteau S., et al., 2014, Reviews of Modern Physics, 86, 47
De Grijs R., van der Kruit P. C., 1996, A&AS, 117, 19
De Grijs R., Peletier R. F., van der Kruit P. C., 1997, A&A, 327, 966
Dehnen W., Binney J. J., 1998, MNRAS, 298, 387
Dopita M. A., Jacoby G. H., Vassiliadis E., 1992, ApJ, 389, 27
Douglas N. G., et al., 2007, ApJ, 664, 257
Fabricius M. H., et al., 2012, in Ground-based and Airborne Instrumentation for Astronomy IV. p. 84465K, doi:10.1117/12.925177
Fathi K., Beckman J. E., Zurita A., Relaño M., Knapen J. H., Daigle O., Hernandez O., Carignan C., 2007, A&A, 466, 905
Gilmore G., Reid N., 1983, MNRAS, 202, 1025
Gnedin O. Y., Kravtsov A. V., Klypin A. A., Nagai D., 2004, ApJ, 616, 16
Herrmann K. A., Ciardullo R., 2009a, ApJ, 703, 894
Herrmann K. A., Ciardullo R., 2009b, ApJ, 705, 1686
Herrmann K. A., Ciardullo R., Feldmeier J. J., Vinciguerra M., 2008, ApJ, 683, 630
Iodice E., et al., 2015, A&A, 583, A48
Jeans J. H., 1915, MNRAS, 76, 70
Jesseit R., Naab T., Burkert A., 2002, ApJ, 571, L89
Kormendy J., Freeman K. C., 2016, ApJ, 817, 84
Kregel M., van der Kruit P. C., de Grijs R., 2002, MNRAS, 334, 646
Kregel M., van der Kruit P. C., Freeman K. C., 2005, MNRAS, 358, 503
Leroy A. K., et al., 2009, AJ, 137, 4670
Macciò A. V., Ruchayskiy O., Boyarsky A., Muñoz-Cuartas J. C., 2013, MNRAS, 428, 882
Maraston C., 2005, MNRAS, 362, 799
Meidt S. E., et al., 2012, ApJ, 744, 17
Meidt S. E., et al., 2014, ApJ, 788, 144
Merrett H. R., et al., 2006, MNRAS, 369, 120
Miller Bertolami M. M., 2016, A&A, 588, A25
Möllenhoff C., 2004, A&A, 415, 63
Muñoz-Cuartas J. C., Macciò A. V., Gottlöber S., Dutton A. A., 2011, MNRAS, 411, 584
Muñoz-Mateos J. C., et al., 2013, ApJ, 771, 59
Mulcahy D. D., Beck R., Heald G. H., 2017, A&A, 600, A6
Navarro J. F., Frenk C. S., White S. D. M., 1997, ApJ, 490, 493
Navarro J. F., et al., 2010, MNRAS, 402, 21
Norris M. A., Meidt S., Van de Ven G., Schinnerer E., Groves B., Querejeta M., 2014, ApJ, 797, 55
Oh S.-H., de Blok W. J. G., Walter F., Brinks E., Kennicutt Jr. R. C., 2008, AJ, 136, 2761
Oh S.-H., de Blok W. J. G., Brinks E., Walter F., Kennicutt Jr. R. C., 2011, AJ, 141, 193
Osterbrock D. E., Fulbright J. P., Martel A. R., Keane M. J., Trager S. C., Basri G., 1996, PASP, 108, 277
Ponomareva A., 2017, PhD thesis, Rijksuniversiteit Groningen
Ponomareva A. A., Verheijen M. A. W., Bosma A., 2016, MNRAS,
Ponomareva A. A., Verheijen M. A. W., Peletier R. F., Bosma A., 2017, MNRAS, 469, 2387
Querejeta M., et al., 2015, ApJS, 219, 5
Röck B., Vazdekis A., Peletier R. F., Knapen J. H., Falcón-Barroso J.,

2015, MNRAS, 449, 2853
Salo H., et al., 2015, ApJS, 219, 4
Schlafly E. F., Finkbeiner D. P., 2011, ApJ, 737, 103
Schwarz G., 1978, Annals of Statistics, 6, 461
Shapiro K. L., Gerssen J., van der Marel R. P., 2003, AJ, 126, 2707
Toomre A., 1964, ApJ, 139, 1217
Van Albada T. S., Bahcall J. N., Begeman K., Sancisi R., 1985, ApJ, 295, 305
Van der Hulst J. M., Terlouw J. P., Begeman K. G., Zwitser W., Roelfsema P. R., 1992, in Worrall D. M., Biemesderfer C., Barnes J., eds, Astronomical Society of the Pacific Conference Series Vol. 25, Astronomical Data Analysis Software and Systems I. p. 131
Van der Kruit P. C., 1988, A&A, 192, 117
Van der Kruit P. C., Freeman K. C., 1984, ApJ, 278, 81
Van der Kruit P. C., Freeman K. C., 2011, ARA&A, 49, 301
Van der Kruit P. C., de Grijs R., 1999, A&A, 352, 129
Wainscoat R. J., Freeman K. C., Hyland A. R., 1989, ApJ, 337, 163
Walter F., Brinks E., de Blok W. J. G., Bigiel F., Kennicutt Jr. R. C., Thornley M. D., Leroy A., 2008, AJ, 136, 2563
Wegg C., Gerhard O., Portail M., 2016, MNRAS, 463, 557
Wielen R., 1977, A&A, 60, 263
Wilson G., 2003, PhD thesis, Australian National University
Woolley R. V. D. R., Martin W. L., Sinclair J. E., Penston M. J., Aslan S., 1977, MNRAS, 179, 81
Yoachim P., Dalcanton J. J., 2006, AJ, 131, 226

APPENDIX A: EFFECT OF THE COLD LAYER ON THE EQUILIBRUM OF THE ISOTHERMAL SHEET

Previous studies that looked at calculating the surface mass density of the disc, ignored the gravitational field of the cold layer (gas and young stars). In this Appendix, we estimate the effect of the cold layer on the structure and surface density of the isothermal disc (see Binney & Tremaine II: problems 4.21 & 4.22).

A1 The distribution function for the isothermal disc

The stellar energy is $E = v^2/2 + \Phi$, where v is the stellar velocity and Φ the potential. The distribution function has the form $f(E) \propto \exp(-E/\sigma^2)$ where σ is the stellar velocity dispersion. Write $\Phi = \sigma^2\phi$. The distribution function for the isothermal sheet is

$$f = \frac{\rho_\circ}{\sqrt{2\pi\sigma^2}} \exp\left(-v^2/2\sigma^2 - \phi\right).$$

The velocity distribution is isothermal and everywhere gaussian, and the density is

$$\rho(z) = \rho_\circ \exp(-\phi)$$

where we take $\phi(0) = 0$. Write $z/h_z = \zeta$. The 1D Poisson equation is

$$\frac{d^2\Phi}{dz^2} = 4\pi G\rho$$

or

$$2\,\frac{d^2\phi}{d\zeta^2} = \frac{8\pi G\rho_\circ h_z^2}{\sigma^2}\exp(-\phi)$$

or

$$2\,\frac{d^2\phi}{d\zeta^2} = \exp(-\phi) \tag{A1}$$

for $h_z^2 = \sigma_z^2/(8\pi G\rho_\circ)$. Equation A1 has the solution $\phi = \ln\cosh^2(\zeta/2)$, $d\phi/d\zeta = \tanh(\zeta/2)$, and

$$\rho = \rho_\circ \exp(-\phi) = \rho_\circ\,\mathrm{sech}^2(\zeta/2) = \rho_\circ\,\mathrm{sech}^2(z/2h_z).$$

At large $|z|$, $\rho \to \exp(-|z|/h_z)$. The surface density is $\Sigma = 4\rho_\circ h_z$, and the vertical force is $K_z = -8\pi G\rho_\circ h_z \tanh(z/2h_z)$.

A2 The isothermal sheet in the presence of the cold layer

We model the disc as an isothermal sheet of hot disc population, plus a thin layer of cold disc population (gas and young stars) with surface density Σ_C. The total density is then

$$\rho_D(z) + \Sigma_C\delta(z)$$

where $\rho_D(z)$ is the density distribution of the isothermal sheet in the presence of the extra component. The vertical force and potential for the cold layer are:

$$K_z = -2\pi G\Sigma_C\, z/|z|$$
$$\Phi_C = 2\pi G\Sigma_C.|z|$$

With the extra component, the energy is $E = v^2/2 + \Phi$, where $\Phi = \Phi_D + \Phi_C$ and Φ_D is the potential of the hot isothermal sheet. Write $\Phi = \sigma_z^2\phi$. The distribution function for the isothermal sheet is

$$f_D = \frac{\rho_\circ}{\sqrt{2\pi\sigma^2}} \exp\left(-v^2/2\sigma_z^2 - \phi\right)$$

and

$$\rho_D = \rho_\circ \exp(-\phi). \tag{A2}$$

Write $z/h_z = \zeta$. The 1D Poisson equation for the isothermal sheet is

$$2\,\frac{d^2\phi_D}{d\zeta^2} = \frac{8\pi G\rho_\circ h_z^2}{\sigma_z^2}\exp(-\phi_D - \phi_C)$$

where $\phi_C = 2\pi G\Sigma_C h_z.|\zeta|/\sigma_z^2$. With $\phi = \phi_D + \phi_C$, equation A2 becomes

$$2\,\frac{d^2\phi}{d\zeta^2} = \frac{8\pi G\rho_\circ h_z^2}{\sigma_z^2}\exp(-\phi) \tag{A3}$$

for $|\zeta| > 0$. The solution to equation A3 gives the potential ϕ and the density distribution ρ_D for the isothermal sheet in the presence of the cold layer. We look for a solution of the form

$$\phi = \ln\frac{\cosh^2(|\zeta|/2 + b)}{\cosh^2 b} \tag{A4}$$

such that $\phi(0) = 0$ and $\phi' = \tanh(|\zeta|/2 + b) \to 2\pi G h_z\Sigma_C/\sigma_z^2$ as $\zeta \to 0$. Equation A4 is a solution if

$$\tanh(b) = 2\pi G h_z\Sigma_C/\sigma^2 \tag{A5}$$

and

$$8\pi G\rho_\circ \cosh^2(b)\, h_z^2/\sigma_z^2 = 1. \tag{A6}$$

The density of the isothermal sheet is then

$$\rho_D(\zeta) = \rho_\circ \cosh^2(b)\,\mathrm{sech}^2(|\zeta|/2 + b). \tag{A7}$$

and its surface density is

$$\Sigma_D = \frac{4\rho_\circ h_z}{1 + \tanh(b)}. \tag{A8}$$

A2.1 The surface density of the isothermal disc

At large $|z|$, equation A7 becomes

$$\rho_D \propto \exp(-|z|/h_z)$$

and the photometric scale height is approximately equal to the natural scale parameter h_z defined in equation A6. From equations A6 – A8, we eliminate the parameter $\rho_\circ$. In terms of its surface density Σ_D and the observables Σ_C, h_z and σ_z, the density distribution of the isothermal sheet is

$$\rho(z) = \frac{\sigma_z^2}{8\pi G h_z^2} \operatorname{sech}^2(|\zeta|/2 + b), \tag{A9}$$

the scaling equation A6 becomes

$$\Sigma_T = \Sigma_C + \Sigma_D = \frac{\sigma_z^2}{2\pi G h_z}, \tag{A10}$$

and equation A5 defines the offset parameter b. From equations A5 and A10, b is approximately the surface density fraction $\Sigma_C/(\Sigma_C + \Sigma_D)$ in the cold layer.

A3 Summary

- In the presence of the cold gas layer Σ_C, the isothermal sheet has the form

$$\rho(z) = \frac{\sigma_z^2}{8\pi G h_z^2} \operatorname{sech}^2(|z|/2h_z + b)$$

where $\tanh(b) = 2\pi G h_z \Sigma_C/\sigma_z^2$.
- The total surface density $\Sigma_T = \Sigma_C + \Sigma_D = \sigma_z^2/(2\pi G h_z)$.
- The scale parameter h_z for the isothermal sheet $\approx$ the exponential scale height for the hot disc.
- The radial dependence of $\sigma_z^2(R) \propto \Sigma_T(R)$, if h_z is constant.

MNRAS 000, 1–11 (2017) Preprint 9 February 2018 Compiled using MNRAS LATEX style file v3.0

Climbing to the top of the galactic mass ladder: evidence for frequent prolate-like rotation among the most massive galaxies

Davor Krajnović [1]⋆, Eric Emsellem[2,3], Mark den Brok[4,1], Raffaella Anna Marino[4], Kasper Borello Schmidt[1], Matthias Steinmetz[1] and Peter M. Weilbacher[1]

[1]*Leibniz-Institut für Astrophysik Potsdam (AIP), An der Sternwarte 16, D-14482 Potsdam, Germany*
[2]*ESO, European Southern Observatory, Karl-Schwarzschild Str. 2, 85748 Garching bei Muenchen, Germany*
[3]*Univ Lyon, Univ Lyon 1, ENS de Lyon, CNRS, Centre de Recherche Astrophysique de Lyon UMR 5574, 69230 Saint-Genis Laval, France*
[4]*ETH Zurich, Department of Physics, Wolfgang-Pauli-Str. 27, 8093 Zurich, Switzerland*

Accepted XXX. Received YYY; in original form ZZZ

ABSTRACT

We present the stellar velocity maps of 25 massive galaxies located in dense environments observed with MUSE. Galaxies are selected to be brighter than $M_{\bar{K}}$=-25.7 magnitude, reside in the core of the Shapley Super Cluster or be the brightest galaxy in clusters richer than the Virgo Cluster. We thus targeted galaxies more massive than 10^{12} $M_{\odot}$ and larger than 10 kpc (half-light radius). The velocity maps show a large variety of kinematic features: oblate-like regular rotation, kinematically distinct cores and various types of non-regular rotation. The kinematic misalignment angles show that massive galaxies can be divided into two categories: those with small or negligible misalignment, and those with misalignment consistent with being 90°. Galaxies in this latter group, comprising just under half of our galaxies, have prolate-like rotation (rotation around the major axis). Among the brightest cluster galaxies the incidence of prolate-like rotation is 57 per cent, while for a magnitude limited sub-sample of objects within the Shapley Super Cluster (mostly satellites), 35 per cent of galaxies show prolate-like rotation. Placing our galaxies on the mass - size diagram, we show that they all fall on a branch extending almost an order of magnitude in mass and a factor of 5 in size from the massive end early-type galaxies, previously recognised as associated with major dissipation-less mergers. The presence of galaxies with complex kinematics and, particularly, prolate-like rotators suggests, according to current numerical simulations, that the most massive galaxies grow predominantly through dissipation-less equal-mass mergers.

Key words: galaxies: elliptical and lenticular, cD – galaxies: formation – galaxies: evolution – galaxies: kinematics and dynamics – galaxies: clusters: individual – galaxies: structure

1 INTRODUCTION

The orbital structure is a powerful tracer of the formation processes shaping galaxies. As galaxies acquire gas, accrete satellites or merge with similar size objects, new populations of stars are created and the mass and luminosity distributions evolve. The changes in the gravitational potential have a direct influence on the allowed and realised trajectories, providing for a variety of observed stellar kinematics. As observers, we thus hope to constrain the ingredients (and chronology) which shaped galaxies by probing the spatial variations of the line-of-sight velocity distribution (LOSVD).

Theoretical insights, based on analytical and numerical work, are crucial for the interpretation of the observed stellar kinematics of galaxies (see e.g., de Zeeuw & Franx 1991). In an idealised system with triaxial symmetry, assuming a gravitational potential expressed in a separable form (e.g. Stäckel potentials as introduced by Eddington 1915), there exist a few families of dissipation-less orbits which stars can adopt: box orbits, short-axis tubes, inner and outer long-axis tubes (de Zeeuw 1985). In such systems, symmetry changes, for example between spherical, oblate or prolate axial symmetries, limit the stability of orbital families. de Zeeuw (1985) showed that a purely oblate spheroid should consist of only short-axis tubes, and therefore show a typical streaming *around* its minor axis, unless there is an equal amount of stars on both prograde and retrograde orbits canceling out the net streaming. A prolate spheroid allows only inner and outer long-axis tubes, and streaming *around* the major axis of the galaxy. The argument can also be reversed to state that galaxies with only long axis tubes cannot be oblate and axisymmetric, or even triaxial, and that a galaxy with short axis tubes does not have prolate symmetry.

⋆ E-mail:dkrajnovic@aip.de

The velocity maps of triaxial spheroids, viewed at random angles, can exhibit a rich variety of kinematic features. This is a direct consequence, as pointed out by de Zeeuw & Franx (1991), of the freedom in the direction of the total angular momentum resulting from the orbital mixture, and the momentum vector which can lie anywhere in the plane containing the major and minor axis of the galaxy. This was illustrated by Statler (1991) with models viewed along various orientation angles, and associated with actually observed galaxies with complex kinematics (e.g. NGC 4356 and NGC 5813; van den Bosch et al. 2008; Krajnović et al. 2015, respectively)

Observational studies using long-slits were able to investigate velocity features along selected angles (often along the minor and major photometric axes), and revealed that a majority of galaxies exhibit negligible rotation along their minor photometric axis (e.g. Davies et al. 1983; Davies & Illingworth 1983; Bender et al. 1994), while a few massive elliptical galaxies show more complex rotation indicating the presence of long-axis tubes and significant rotation around their major axis (e.g. Illingworth 1977; Schechter & Gunn 1979; Wagner et al. 1988). A major change in this field came from the proliferation of the integral-field spectrographs (IFS) and their ability to map the distribution of velocities over a significant fraction of the galaxy. The last decade of IFS observations has revealed that the vast majority of galaxies actually has very regular velocity maps within their half light radii (e.g. Emsellem et al. 2004; Krajnović et al. 2011; Houghton et al. 2013; Scott et al. 2014; Fogarty et al. 2015; Falcón-Barroso et al. 2017).

The ATLAS^{3D} project (Cappellari et al. 2011a) addressed this more specifically via a volume limited survey of nearby early-type galaxies, demonstrating that galaxies with complex velocity maps comprise only about 15% of the local population of early-type galaxies (Krajnović et al. 2011), and that the majority is consistent with oblate rotators (notwithstanding the presence of a bar, see Krajnović et al. 2011; Weijmans et al. 2014). The regular and non-regular rotator classes seem to reflect a significant difference in their specific stellar angular momentum content, allowing an empirical division of early-type galaxies into fast and slow rotators (Emsellem et al. 2007, 2011). Krajnović et al. (2008) also emphasised the fact that axisymmetric fast rotators have regular velocity fields which qualitatively resemble those of disks. The internal orbital structure of these galaxies can, however, be complex, as evidenced by the range of photometric properties (e.g. disk-to-bulge ratio) and the common presence of tumbling bars.

There are several caveats which need to be emphasised. Firstly, the intrinsic shape of a galactic system is seldom well defined by a single number, e.g., the apparent ellipticity varies with radius. Along the same lines, the terms ”triaxial” or ”oblate” systems may not even be appropriate when the intrinsic ratios and/or the position angle of the symmetry axes change with distance from the centre: the gravitational potential of a galaxy could smoothly vary from oblate in the centre to strongly triaxial or prolate in the outer part, with the main symmetry axes not even keeping the same orientation. Secondly, ellipsoids are certainly a very rough approximation when it comes to describing the intrinsic shapes of galaxies, as they have overlapping components with different flattenings, varying bulge-to-disk ratios, and often host (tumbling) bars. While the observed kinematics of fast rotators (including also higher moments of the LOSVD, Krajnović et al. 2008, 2011; van de Sande et al. 2017) seem to indicate that their internal orbital structure is dominated by short-axis tube orbits (and streaming around the minor axis), numerical simulations of idealised mergers and those performed within a cosmological context naturally predict the co-existence of multiple orbital families, the central and outer regions often being dominated by box and short-axis tube orbits, respectively (e.g. Jesseit et al. 2005; Hoffman et al. 2010; Röttgers et al. 2014).

The division of galaxies into fast and slow rotators connects also with two dominant channels of galaxy formation (as reviewed in Cappellari 2016). Present spirals and fast rotators are mostly descendants of star forming disks and their evolution is dominated by gas accretion, star formation, bulge growth and eventual quenching. The slow rotators may also start as turbulent star-bursting disks at high redshift (e.g. Dekel et al. 2009; Kereš et al. 2009), or be hosted by haloes with small spin parameters (Lagos et al. 2017), but the late evolution of most slow rotators is dominated by mergers with gas poor galaxies (De Lucia & Blaizot 2007; Dekel et al. 2009; Williams et al. 2011; Kaviraj et al. 2015). The first channel therefore favours regular kinematics and internal orbital structure dominated by short-axis tubes, while the second channel implies dynamically violent redistribution of orbits and the creation of triaxial or prolate-like systems, which include a significant fraction of long-axis tubes. A strong mass dependence has been emphasised, with more massive galaxies being more likely to follow the second channel (Rodriguez-Gomez et al. 2016; Qu et al. 2017).

A clear manifestation of the triaxial nature of galaxies is a non-zero value of the kinematic misalignment angle, Ψ, the angle between the photometric minor axis and the orientation of the apparent angular momentum vector (Franx et al. 1991). In an axisymmetric galaxy, the apparent angular moment coincides with the intrinsic angular momentum and is along the minor axis, hence $\Psi = 0$. Triaxial galaxies can exhibit any value of Ψ, while prolate galaxies with significant rotation would have Ψ closer to 90°. Galaxies with large Ψ exist (Franx et al. 1991; Cappellari et al. 2007; Krajnović et al. 2011; Fogarty et al. 2015; Tsatsi et al. 2017) and are typically more massive than 10^{11} $M_\odot$ (but for dwarf galaxies see e.g. Ho et al. 2012; Ryś et al. 2013). It is, however, not clear if prolate-like systems feature prominently at high mass and if this links preferentially to a specific channel of galaxy evolution.

Galaxies at the top of the mass distribution are intrinsically rare. They are mostly found in dense environments, often as the brightest members of groups or clusters. Brightest cluster galaxies (BCGs) are usual suspects, and are known to have low amplitude or zero rotation (Loubser et al. 2008; Jimmy et al. 2013; Oliva-Altamirano et al. 2017). Still, current surveys of massive galaxies have so far offered little evidence for large Ψ values or clear-cut signatures for strong triaxiality (e.g. Veale et al. 2017b). In this work, we present preliminary results from an observation-based survey, the M3G (MUSE Most Massive Galaxies; PI: Emsellem) project, aimed at mapping the most massive galaxies in the densest galaxy environments at $z \approx 0.045$ with the MUSE/VLT spectrograph (Bacon et al. 2010). We focus on presenting the stellar velocity maps, emphasising the relatively large number of prolate-like systems, i.e., galaxies with rotation *around* the major axis. The orbital distribution of galaxies exhibiting large values of Ψ (and having net rotation around the major axis) are thought to be dominated by long-axis tubes: we will thus refer to such cases as *prolate-like* rotation[1]. However, as mentioned above, and discussed in Section 4,

[1] An alternative name used in the literature is *minor-axis* rotation, as the gradient of the velocities is *along* the major axis, and it should be differentiated from rotation *around* the minor axis present in oblate axisymmetric systems. To avoid any ambiguity, next to the defined prolate-like rotation, we will use the nomenclature from Krajnović et al. (2011), where regular rotation is used for oblate rotators with velocity maps consistent with those

we caution the reader that this does not imply that these are prolate systems. Presenting the complete survey, its data products and subsequent results is beyond the scope of the current publication and will be presented in forthcoming papers.

In Section 2 we briefly report on the observations and the data analysis. We present the main results on the rotational characteristics of the M3G sample in Section 3, which is followed by a discussion in Section 4 and a brief summary of conclusions in Section 5.

2 OBSERVATIONS AND ANALYSIS

In this section we briefly describe the M3G sample of galaxies, the observations and the extraction of the kinematic information. Further details on these aspects will be presented in a following M3G paper (Krajnović et al. in prep.).

2.1 The M3G sample and MUSE observations

The M3G sample comprises 25 early-type galaxies selected to be brighter than -25.7 magnitude in the 2MASS K_s−band and found in the densest environments. We created two sub-samples of galaxies: one consisting of the brightest galaxies in the densest known structure, the core of the Shapley Super Cluster (SSC) (Shapley 1930; Merluzzi et al. 2010, 2015), and the other targeting BCGs in rich clusters. We selected galaxies in the SSC using the 2MASS All Sky Extended Source Catalog (XSC, Jarrett et al. 2000; Skrutskie et al. 2006) centred on the three main clusters near the core of the SSC: Abell 3562, 3558 and 3556 (Abell et al. 1989). This selection yielded 14 galaxies, with 3 being BCGs. The complementary sub-sample of BCGs was defined using a parent sample of clusters richer than the Virgo Cluster and observed with the HST (Laine et al. 2003). We included 11 BCGs residing in clusters with richness larger than 40, where the richness is defined as the number of galaxies with magnitudes between m_3 and $m_3 + 2$ within an Abell radius of the cluster centre (m_3 is the magnitude of the third brightest cluster galaxy). Here we also used the information given in Laine et al. (2003). The full M3G sample therefore consists of 14 galaxies in the SSC, and 14 BCG (three being in the SSC). In this paper we use 2MASS photometry as a reference, but as part of the M3G project, we have collected photometry from other imaging campaigns, which will be described in detail in future papers.

In addition to the visibility requirement that the galaxies are observable from Paranal, we imposed a selection criterion based on the distance and size of the galaxies: these had to be such that the MUSE field-of-view covers up to two effective radii of each target. The effective radii were collected from the XSC catalog, using the `k_r_eff` keyword. The most massive galaxies in the SSC have the right combination of parameters to satisfy this criterion, while the additional 11 BCGs were selected to be at similar redshifts. The galaxies span the redshift range $0.037 < z < 0.054$, with a mean of z=0.046. The redshift of the SSC is assumed to be 0.048 (Metcalfe et al. 1987). Adopting cosmology $H_0 = 70$ km s^{-1} Mpc^{-1}, $\Omega_M = 0.3$, $\Omega_\Lambda = 0.7$, 1″ is 904 pc at the mean redshift of the sample, while this scales changes from 735 to 1050 pc between galaxies (Wright 2006).

The observations of the sample were performed within the MUSE Guaranteed Time Observations (GTO) during ESO Periods 94 - 99 (starting in the fall of 2014 and finishing in the spring of 2017). The observing strategy consisted of combining a short Observing Block (OB) of exposures during better-than-average seeing conditions (< 0.8″) to map the central structures, and a set of OBs with longer exposure times to reach a sufficient signal-to-noise ratio (S/N) at two effective radii. The high spatial (short exposure time) resolution MUSE data will be presented in a forthcoming paper. The total exposure time for each galaxy varied from about 2 to 6 hours. The brightest galaxy in the sample (see Table 1 for details) was mosaiced with 2 × 2 MUSE fields, each observed up to 6h. All individual OBs consisted of four on-target observations and two separate sky fields sandwiched between the on-target exposures. On-target observations were each time rotated by 90° and dithered in order to reduce the systematics introduced by the 24 MUSE spectrographs.

2.2 Data reduction and kinematics extraction

Data reduction was performed as the observations were completed. This means that several versions (from v1.2 to the latest v1.6) of the MUSE data reduction pipeline (Weilbacher et al. 2014) were used. Despite continued improvement of the reduction pipeline, given the brightness of the M3G sample, and the nature of the current study, the differences in the reductions do not affect the results and conclusions presented here. All reductions followed the standard MUSE steps, producing the master calibration files of the bias and flat fields, as well as providing the trace tables, wavelength calibration files and line-spread function for each slice. When available we also used twilight flats. Instrument geometry and astrometry files were provided by the GTO team for each observing run. These calibrations files, as well as the closest in time illumination flats obtained during the night, were applied to the on-target exposures. From separate sky fields we constructed the sky spectra which were associated with the closest in time on-target exposure, and from the observation of a standard star (for each night) we extracted the response function as well as an estimate of the telluric correction. These, together with the line-spread function (LSF) and the astrometric solution, were used during the science post-processing. The final data cubes were obtained by merging all individual exposures. As these were dithered and rotated, a precise alignment scheme was required. This was achieved using stars or unresolved sources, and for a few cases in which the MUSE field-of-view was devoid of such sources, using the surface brightness contours in the central regions. The final cubes have the standard MUSE spatial spaxel of 0.2″×0.2″ and a spectral sampling of 1.25 Å per pixel.

As a first step before extraction of the kinematics, we proceeded to spatially bin each data cube to homogenise the signal-to-noise ratio throughout the field-of-view via the Voronoi binning method (Cappellari & Copin 2003)[2]. We first estimated the S/N of individual spectra from the reduction pipeline propagated noise, masking all stars or satellite galaxies within the field-of-view. Spatial binning is ultimately an iterative process, in which our goal was to achieve relatively small bins beyond one effective radius, but which provide a sufficient signal for extraction of robust kinematics. The quality of the extraction was measured using the signal-to-residual noise ratio (S/rN), where the residual noise is the standard deviation of the difference between the data and the model (as explained below). S/rN was required to be similar to the target S/N in bins at large radii. As the data quality varies between galaxies,

of discs, while non-regular rotation is used for twisted and complex velocity maps.

[2] Available at http://purl.org/cappellari/software

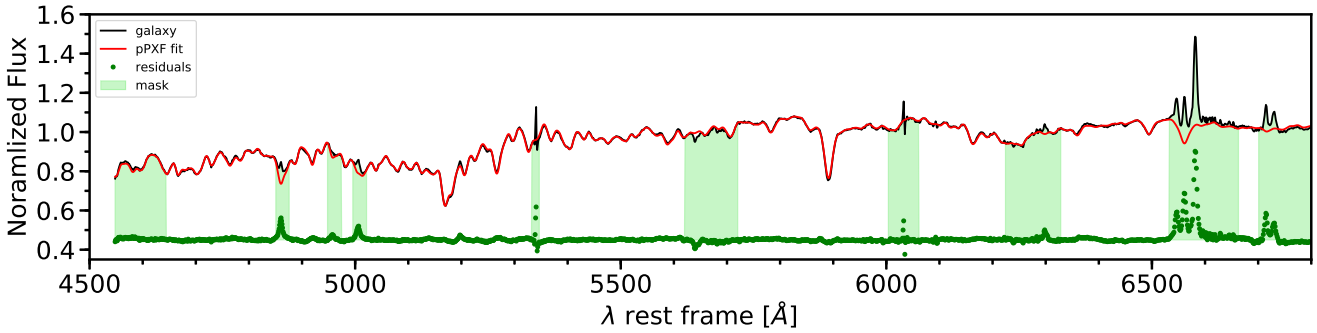

Figure 1. An example of the pPXF fit to a spectrum extracted within an effective radius from PGC047177, which also shows ionised gas emission. The observed spectrum is shown in black and the best fit in red. Green dots are residuals. Light green shaded areas were masked and not fitted. These include the strongest emission-lines expected between 4500 Å and 7000 Å, as well as potential strong sky lines or telluric residuals.

it is possible for some galaxies to have sufficiently small bins in the central regions with S/rN ~ 100, while for some galaxies S/rN ~ 50 is the most that can be achieved for a reasonable bin size. For this work, we set the target S/N required by the Voronoi binning method to 50 for all galaxies. Additionally, before binning we removed all spectra (individual spaxels) with S/N less than 2.5 in the continuum (based on the pipeline estimated noise)[3]. In this way we excluded the spectra at the edge of the MUSE FoV, which essentially do not contain any useful signal and limited the sizes of the outermost bins.

Stellar kinematics were extracted using the pPXF method[4] (Cappellari & Emsellem 2004). Our pPXF set up included an additive polynomial of the 4th order, and we fitted a line-of-sight velocity distribution parametrised by Gauss-Hermit polynomials (van der Marel & Franx 1993; Gerhard 1993) with the mean velocity V, the velocity dispersion σ and the higher order moments h_3 and h_4. We masked all potential emission-lines and a few narrow spectral windows with possible sky-line residuals. Finally, we limited the fit to blue-wards of 7000 Å, to exclude potentially strong telluric and sky residuals. For each galaxy, a pPXF fit was first performed on the spectrum obtained by summing all MUSE spectra within one effective radius (covering an elliptical area equivalent to $\pi \times R_e^2$) and using the full MILES stellar library (Sánchez-Blázquez et al. 2006; Falcón-Barroso et al. 2011) as templates. The MUSE LSF significantly varies with wavelength with a full-width half maximum from 2.85 Å at 5000Å to 2.5 Å at 7000 Å (Guérou et al. 2017). We used the parametrisation of the LSF from Guérou et al. (2017) and convolved the MILES templates to the MUSE LSF (varying with wavelength). Possible emission-lines were masked. As an example, we show the fit to the spectrum extracted within the half-light redius of one of our galaxies in Fig. 1.

This first global pPXF fit provides an optimal set of stellar templates, which we propagate for each individual Voronoi-binned spectrum, using the same pPXF set-up. The quality of the fit was checked via the S/rN of each bin, where the residual Noise was the standard deviation of the difference between the data and the best-fit pPXF model. As outlined above, this S/rN was required to be at least 50 over most of the field-of-view. We extracted up to the 4th Gauss-Hermit coefficient, but in this work we will primarily focus on the mean velocity maps of our 25 galaxies. The velocity dispersion and higher order velocity moments maps, as well as the analysis of the angular momentum will be presented in a future paper. The global velocity dispersion values are given in Table 1.

3 PREVALENCE OF LONG-AXIS ROTATION IN MASSIVE GALAXIES

The velocity maps for the full M3G sample are shown in Fig. 2. The sample is split into BCGs (first 14 maps) and non-BCGs from the SSC. In each subgroup galaxies are plotted in order of decreasing 2MASS K-band absolute luminosity. There are several noteworthy features in these maps, which we interpret within the kinematic classification system of the ATLAS^{3D} survey (Krajnović et al. 2011). To start with, we note that almost all galaxies show some level of rotation. While the maximum velocity amplitudes reached within the two effective radii covered by our MUSE observations are often low ($\approx 30-50$ km/s), only one galaxy, e) PGC 043900, does not show a clear indication for net streaming motion within the field of view. This is somewhat different from the trend expected from the ATLAS^{3D} data (Emsellem et al. 2011; Krajnović et al. 2011), where a few of the most massive systems (about 15 per cent for galaxies more massive than 2×10^{11} M$_\odot$), can be characterised as having no net rotation. Other studies of massive galaxies (e.g. Veale et al. 2017b) also find a large number of galaxies with negligible net rotation. It is likely that, as in the case of NGC 4486 (Emsellem et al. 2014), our MUSE data are of such quality and extent that the rotation is revealed even in systems such as r) PGC 047590, where the amplitude of the rotation is only 30 km/s[5].

The coverage beyond one effective radius helps to determine the net rotation trend, but also reveals changes in the kinematics. This is especially noticeable among BCGs, where the velocity maps change orientation (e.g. b) PGC 048896), or there is a loss of coherent motions (e.g. h) PGC 065588). Non-BCGs, which we will call satellites in this context, do not show such changes. It might be the case that the changes are found at larger radii (as for some lower-

[3] The value of S/N ~ 2.5 was selected as a compromise between removing too many pixels in the outer regions and reducing the size of the outermost bins.

[4] See footnote 2 for software availability.

[5] A similar change of kinematic classification based on higher quality kinematics could happen to NGC 5846, another ATLAS^{3D} "non-rotator" with a hint for prolate-like rotation in the SAURON data.

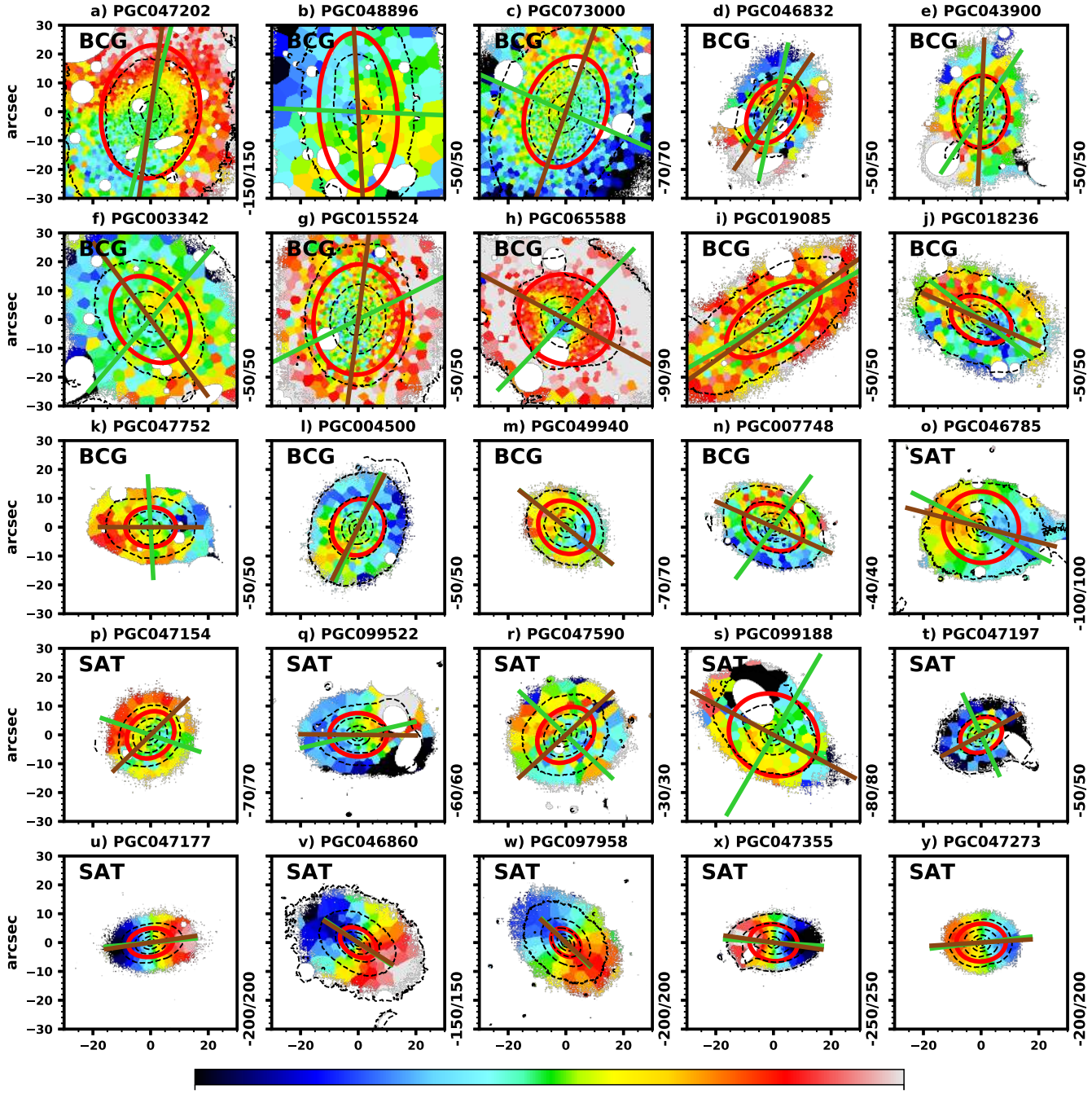

Figure 2. The mean stellar velocity maps of the M3G sample galaxies. Galaxies are divided in two groups, the BCGs and satellites (non-BCGs in the SSC). BCGs are plotted in the first 14 panels starting from the top left, followed by satellites (as indicated with "SAT"). The two groups of galaxies are ordered by decreasing *K*-band absolute magnitude. The values in the lower right corner of each panel indicate the range of the velocities, where the negative are shown with blue and positive with red colours, as indicated by the colourbar. Black dashed contours are isophotes plotted in steps of one magnitude. All velocity maps are approximately $1' \times 1'$ in size. Full red ellipses indicate the size and the orientation of the half-light region, specified by the ellipticity of the galaxy and the semi-major axis length equal to the 2MASS K*s*-band effective radius. Green and brown lines indicate the orientation of the kinematic and the photometric major axes, respectively. Letters in upper right corner of each panel ("PRO", "TRI" and "OBL") indicate broad shape-related categories of the galaxy based on the kinematic misalignment (see Fig. 3 for details). The letters in front of the galaxy names will be used in text for easier location of the object.

mass fast rotators, Arnold et al. 2014), but there is no clear evidence for this within 2 R_e.

Another striking feature is that there are galaxies which show regular rotation, with peak velocity in excess of 200 km/s. These galaxies are in fact among the lower luminosity bin of our set of massive galaxies, and found within the group of satellites. Galaxies that belong to this class are v) PGC046860, u) PGC047177, y) PGC047273, x) PGC047355 and w) PGC097958. Their dynamical masses (see Section 4) are around 10^{12} $M_\odot$, and they are all among the most massive galaxies with regular rotation. Their existence is

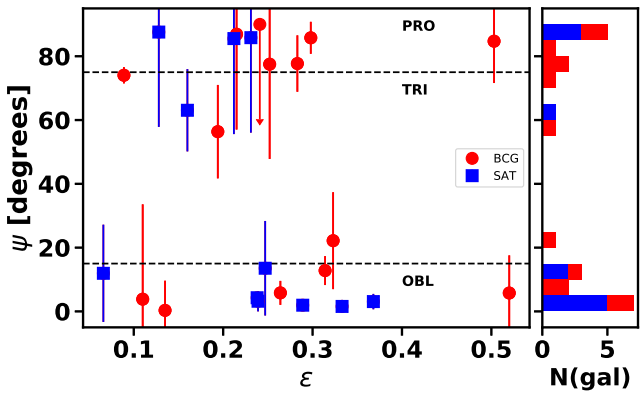

Figure 3. Distribution of the kinematic misalignment angle as a function of ellipticity, both measured within the effective radius of M3G sample galaxies. Red circles show BCGs, while blue squares are non-BCGs in the SSC (we call them satellites or SAT for simplicity). The symbol with an upper limit error bar is PGC 043900, the system with no net rotation and, therefore, no reliable PA_{kin} measurement. Horizontal lines at $\Psi = 15°$ and $75°$ are used to guide the eye for an approximate separation of shapes of galaxies, between mostly oblate (indicated with "OBL"), triaxial ("TRI") and prolate ("PRO"). These divisions are not meant to be rigorous but indicative. Colours on the right-hand side histogram follow the same convention as shown on the main plot and the legend.

expected (e.g. Brough et al. 2007; Loubser et al. 2008; Veale et al. 2017b; Lagos et al. 2017), although their number likely decreases with increasing mass (e.g. Krajnović et al. 2011; Jimmy et al. 2013; Houghton et al. 2013; Veale et al. 2017b; Brough et al. 2017). The fact that these galaxies are not found among BGCs is indicative of their less violent evolution maintaining the regular rotation. However, there is also the case of a) PGC 047202, the largest and the most luminous galaxy in the SSC, and a BCG, which shows high level of rotation, albeit non-regular.

Non-regular rotation is the most common characteristics of the M3G velocity maps. It is especially among BCGs, but it also occurs in non-BCGs. The existence of kinematically distinct cores (KDC), counter-rotation, the radial variation of the kinematic position angle, as well as the analysis of the velocity features beyond the effective radius will be discussed in a future paper. Here we quantify the kinematic misalignment angle Ψ as the difference between the position angle defined by the photometric major axis (PA_{phot}) and the global kinematic position angle (PA_{kin}) approximately within 1 effective radius. We measure PA_{kin} using the method presented in Appendix C of Krajnović et al. (2006)[6], which provides a global orientation of the velocity map. PA_{phot} was measured by calculating the moments of inertia[7] of the surface brightness distribution from the MUSE white-light images (obtained by summing the MUSE cubes along the wavelength dimension). At the same time, the method provides the global ellipticity ϵ. As we used MUSE cubes for both PA_{kin} and PA_{phot}, they were estimated approximately within the same region. In Table 1 we report the measured photometric and kinematic position angles as well as other relevant properties used in this paper.

[6] See footnote 2 for software availability.
[7] The routine can be found within the MGE Package (Cappellari 2002) at http:/www.purl.org/cappellari/

Kinematic and photometric position angles are shown in Fig. 2 as green and brown lines, respectively. Systems with regular rotation have almost overlapping lines, while systems with non-regular rotation often show that the kinematic misalignment angle Ψ is close to 90°. To quantify this, we also present the distribution of Ψ as a function of the galaxy projected ellipticity ϵ for the M3G sample in Fig. 3. We split galaxies into BGCs and satellites and draw two horizontal lines at 15° and 75° to separate oblate, triaxial and prolate geometries.

The most noteworthy characteristic of Fig. 3 is that galaxies seem to group in two regions, one with low and one with high Ψ. Galaxies with $\Psi < 15°$ are generally consistent with having oblate symmetries. Their velocity maps look regular, and all galaxies with high rotation amplitudes are found in this group. In order of rising ellipticity these BCGs are: l) PGC 004500, m) PGC 049940, a) PGC 047202, j) PGC 018236 and i) PGC 019085. Their intrinsic shapes are likely not axisymmetric, as their velocity maps show kinematic twists and are not regular, but the velocity maps are close to aligned with their photometric axes.

Galaxies with Ψ significantly larger than 0 (and lower than 90) cannot be axisymmetric as their net angular momentum is not aligned with one of the principle axes. Very indicative is also that 9 galaxies have $\Psi > 75°$. A closer examination shows rotation *around* the major axis within a large fraction of the half-light radius. These galaxies exhibit prolate-like rotation, as it is defined in Section 1 within a significant part of the MUSE field-of-view. The rotation amplitude is, as in the case of other non-regular rotators, typically small, mostly around 50 km/s or lower, and the observed (luminosity-weighted) rotation has to be supported by the existence of long-axis tube orbits.

There are 4 galaxies with $15° < \Psi < 75°$: h) PGC 065588, p) PGC 047154, g) PGC 015524 and d) PGC 046832 (in order of decreasing Ψ). The first three have similar rotation pattern as other galaxies with prolate-like rotation. Strictly speaking the Ψ values are inconsistent with 90°, but their velocity maps resemble those of galaxies with prolate-like rotation. We will, therefore, also refer to them as having prolate-like rotation. On the other hand, d) PGC 046832 exhibits a very complex velocity map with multiple changes between approaching and receding velocities, but its velocity map does not resemble prolate-like rotation, and its Ψ is significantly smaller than for other galaxies in this group. Therefore, we will not consider it to have prolate-like rotation. Another special case is e) PGC 043900, which does not have any rotation and its Ψ is not well defined. Therefore, it is plotted as an upper limit.

The prolate-like rotation comes in two flavours. It can be present across the full observed field-of-view (approximately 2 effective radii), for example in n) PGC007748, h) PGC065588 and r) PGC047590, but most galaxies have it within a specific area, either outside the central region (but within one effective radius, s) PGC099188), or more typically covering the full half-light radius (e.g. k) PGC047752, f) PGC003342, c) PGC007300 or b) PGC048896). In these cases, the rotation at larger radii either disappears (e.g. t) PGC047197) or there is a change in the kinematic position angle and the rotation is consistent with being around the minor axis (f) PGC003342, c) PGC073000, b) PGC048896). The change in the kinematic position angle is relatively abrupt and occurs over a small radial range. Therefore, such galaxies could even be characterised as having large-scale KDCs, with the central component exhibiting prolate-like rotation. More typical and standard size KDCs are found in a few M3G targets (i) PGC019085 and d) PGC046832), but these will be discussed in more detail in a future

Table 1. General properties of the galaxies.

Name	M_K 2MASS mag	PA_{kin} [degree]	PA_{phot} [degree]	Ψ [degree]	ϵ	σ_e [km/s]	R_e [kpc]	log (M_*) [log($M_\odot$)]	BCG	Fig. 2
(1)	(2)	(3)	(4)	(5)	(6)	(7)	(8)	(9)	(10)	(11)
PGC003342	-26.34	139.2 ± 29.7	36.7 ± 0.3	77.5 ± 29.7	0.25	270.0 ± 1.6	24.5	12.283	1	f)
PGC004500	-25.85	157.3 ± 29.7	153.5 ± 1.4	3.8 ± 29.7	0.11	256.5 ± 1.6	13.2	12.026	1	l)
PGC007748	-25.76	143.7 ± 8.8	66.0 ± 0.8	77.7 ± 8.8	0.28	265.6 ± 1.2	15.9	12.072	1	n)
PGC015524	-26.10	116.5 ± 12.6	172.9 ± 7.5	56.4 ± 14.6	0.19	272.9 ± 1.4	20.7	12.233	1	g)
PGC018236	-25.93	52.9 ± 4.5	65.7 ± 0.5	12.8 ± 4.5	0.31	274.5 ± 1.5	18.3	12.142	1	j)
PGC019085	-26.04	119.5 ± 11.8	125.3 ± 0.3	5.8 ± 11.8	0.52	261.2 ± 1.4	28.4	12.358	1	i)
PGC043900	-26.46	146.7 ± 89.1	177.5 ± 1.7	< 90	0.24	376.7 ± 2.2	25.8	12.539	1	e)
PGC046785	-26.39	63.5 ± 4.0	75.4 ± 14.7	11.9 ± 15.2	0.07	333.9 ± 1.8	18.2	12.464	3	o)
PGC046832	-26.59	167.9 ± 11.8	145.7 ± 9.6	22.2 ± 15.2	0.32	311.9 ± 1.4	21.4	12.359	2	d)
PGC046860	-25.89	56.0 ± 1.8	57.6 ± 1.0	1.6 ± 2.0	0.33	282.8 ± 1.2	13.0	12.038	3	v)
PGC047154	-26.29	71.1 ± 12.9	134.2 ± 0.2	63.1 ± 12.9	0.16	319.5 ± 2.2	16.0	12.254	3	p)
PGC047177	-25.89	95.3 ± 2.0	98.4 ± 1.3	3.1 ± 2.4	0.37	287.3 ± 1.5	15.3	12.104	3	u)
PGC047197	-25.99	24.2 ± 29.7	118.4 ± 2.1	85.8 ± 29.8	0.23	301.7 ± 1.8	14.3	12.136	3	t)
PGC047202	-27.19	166.4 ± 2.8	172.2 ± 2.5	5.8 ± 3.8	0.26	318.9 ± 2.2	39.3	12.668	2	a)
PGC047273	-25.69	96.8 ± 2.3	93.6 ± 2.2	3.2 ± 3.2	0.24	261.3 ± 1.4	18.4	12.064	3	y)
PGC047355	-25.79	86.2 ± 1.0	81.9 ± 1.2	4.3 ± 1.6	0.24	252.9 ± 1.3	14.8	12.026	3	x)
PGC047590	-26.09	46.9 ± 29.7	132.4 ± 3.8	85.5 ± 29.9	0.21	288.8 ± 2.1	16.8	12.254	3	r)
PGC047752	-25.89	3.0 ± 29.7	89.9 ± 3.3	86.9 ± 29.9	0.22	261.0 ± 1.7	21.2	12.073	2	k)
PGC048896	-26.70	87.7 ± 13.1	3.0 ± 0.5	84.7 ± 13.1	0.50	322.0 ± 1.9	34.9	12.611	1	b)
PGC049940	-25.83	51.4 ± 9.1	51.7 ± 1.9	0.3 ± 9.3	0.14	298.6 ± 1.7	12.6	12.078	1	m)
PGC065588	-26.05	136.1 ± 2.3	62.1 ± 1.1	74.0 ± 2.5	0.09	274.0 ± 2.1	22.3	12.309	1	h)
PGC073000	-26.65	66.6 ± 5.0	160.8 ± 0.3	85.8 ± 5.0	0.30	283.6 ± 1.8	30.4	12.450	1	c)
PGC097958	-25.79	45.4 ± 1.5	47.3 ± 0.3	1.9 ± 1.5	0.29	285.9 ± 1.3	9.70	11.972	3	w)
PGC099188	-25.99	149.7 ± 29.7	62.1 ± 1.4	87.6 ± 29.7	0.13	224.2 ± 1.2	26.2	12.198	3	s)
PGC099522	-26.09	102.9 ± 11.1	89.4 ± 9.8	13.5 ± 14.8	0.25	234.6 ± 0.9	19.0	12.036	3	q)

Notes: Column 1: names of galaxies; Column 2: Absolute magnitudes; Column 3: kinematic position angle; Column 4: photometric position angle: Column 5: kinematic misalignment error; Column 6: ellipticity; Column 7: velocity dispersion within the effective radius; Column 8: effective radius based on the `j_r_eff` 2MASS XSC keyword; Column 9: stellar mass; Column 10: galaxy is a BCG - 1, galaxy is a BCG in the SSC - 2, galaxy is a "satellite" in the SSC - 3; Column 11: the letter referring to the position of the object in Fig. 2. Absolute K-band magnitudes are based on the 2MASS K-band total magnitudes and the distance moduli obtained from NED (http://ned.ipac.caltech.edu). The same distance moduli were used to convert sizes to kiloparsecs. Note that while we report actual measurements for the kinematic and photometric position angles, the kinematic misalignment Ψ for PGC043900 is an upper limit, as there is no net streaming in this galaxy. The stellar mass reported in the last column was estimated using columns 7 and 8, and the virial mass estimator from Cappellari et al. (2006).

paper devoted to the analysis of the high spatial resolution MUSE data cubes.

Finally, for a few galaxies there is evidence for a significant change beyond one effective radius in the properties of the velocity maps: regardless of regular or non-regular rotation within the effective radius, the outer parts show no rotation. They are, however, characterised by a spatially symmetric shift of velocities to larger values compared to the systemic velocity of the galaxy. Examples are the BCGs: m) PGC049940, i) PGC019085 and g) PGC015524. Except for stressing that such velocities at larger radii are only found in the BCGs, we will postpone the discussion of these features to a future paper when it will be put in the full context of the kinematics of M3G galaxies.

4 DISCUSSION

In Fig. 4 we place the M3G sample on the mass - size diagram. We indicate the type of observed kinematics with different symbols and colours and also add the galaxies from the ATLAS^{3D} magnitude-limited sample for comparison. Galaxy masses and sizes for ATLAS^{3D} galaxies were obtained from Cappellari et al. (2013b). For M3G objects we used their 2MASS sizes (XSC keyword `j_r_eff`), defining the size as $R_e = 1.61 \times$ `j_r_eff` as in Cappellari (2013). Masses of the sample galaxies were approximated using the virial mass estimator $M_* = 5 \times (R_e \sigma_e^2)/G$ (Cappellari et al. 2006), where σ_e is the effective velocity dispersion extracted from the MUSE data within an ellipse of area equal to $\pi \times R_e^2$.

Using the full M3G sample, up to 44 per cent of galaxies have prolate-like rotation (here we include h) PGC 065588, p) PGC 047154 and g) PGC 015524 with $\Psi > 60°$). The M3G objects located in the SSC form a magnitude-limited subsample within a well defined environment. This subsample contains 5/14 (35 per cent) galaxies with prolate-like rotation (including three BCGs). The fraction of prolate-like rotation is higher among BCGs. In our sample there are 8/14 BCGs with prolate-like rotation, or 57 per cent. A comparison with the ATLAS^{3D} sample indicates that galaxies with prolate-like rotation are mostly found in massive galaxies and that they are typical for dense environments. This can be somewhat quantified using the literature data.

Within the ATLAS^{3D} sample there are six known galaxies with prolate-like rotation (NGC 4261, NGC 4365, NGC 4406, NGC 5485, NGC 5557 and NGC 4486), while Tsatsi et al. (2017) found 8 new systems in the CALIFA sample (LSBCF560-04, NGC0810, NGC2484, NGC4874, NGC5216, NGC6173,

NGC6338, and UGC10695; Falcón-Barroso et al. 2017)[8]. Together with the previously known cases such as NGC1052 (Schechter & Gunn 1979), NGC4589, NGC5982 and NGC7052 (Wagner et al. 1988), this means a total of 17 galaxies with apparent prolate-like rotation were previously known in the nearby universe. The MASSIVE survey (Ma et al. 2014) found 11 galaxies with kinematic misalignment larger than 60°, whereas 7 of those have $\Psi > 75°$ and can therefore be considered to have prolate-like rotation (Ene et al. 2018). These galaxies are: NGC 708, NGC 1060, NGC 2783, NGC 2832, NGC 7265, NGC 7274, and UGC 2783, where all of them except NGC7274 are classified as BCGs or brightest group galaxy (BGG). Combining the M3G sample of galaxies with prolate-like rotation with those from the literature, we see that such rotation typically does not occur for $M_* \lesssim 10^{11}$ $M_\odot$, and that for $M_* \gtrsim 10^{12}$ $M_\odot$ velocity maps with prolate-like rotation correspond to the most populated kinematic category.

Within the M3G sample, the prolate-like rotation is mostly found in BCGs, but is also present in non-BCGs. However, all galaxies in the M3G sample are members of groups or clusters of galaxies. Even when including the literature data, most galaxies with prolate-like rotation have been observed in galaxy clusters or groups. A similar finding is reported by the MASSIVE survey (Ene et al. 2018), where galaxies with prolate-like rotation are almost exclusively found in BCGs/BGGs, and generally misaligned galaxies ($\Psi > 15°$) are rare in the low density environments, but common among the BCGs/BGGs or satellites. As the creation of non-regularly rotating, massive galaxies with low angular momentum (typical hosts for prolate-like rotation) can a priori occur in any environment (e.g. Cappellari et al. 2011b; Veale et al. 2017a), we expect that galaxies with prolate-like rotation, if rare, still exist outside of dense environments. The evidence that this might be so could be seen in recent merger galaxies, such as NGC 1222 (Young et al., submitted) or NGC 7252 (Weaver et al. 2018). These galaxies are in late merging phases, and have not yet fully settled, but show prolate-like rotation of the stellar component. What makes them significantly different from other prolate-like systems, is their richness in atomic and emission-line gas, as well as ongoing star formation, implying that there are multiple ways of creating prolate-like kinematics. Such galaxies seem however rare, as (Barrera-Ballesteros et al. 2015) does not report a significant incidence of large kinematic misalignment in mergers. A survey of massive galaxies across various environments could constrain the dependence of prolate-like rotation on the environment, as well as offer new possible scenarios for their formation.

Numerical simulations suggest that prolate-like rotation may be the outcome of binary mergers for specific orbital configurations (e.g Łokas et al. 2014). For example, major (1:1) dissipationless mergers in the study by Naab & Burkert (2003) exhibit rotation around the minor axis. Furthermore, the orbital structure and the shapes of remnants of major collisionless mergers indicate significant triaxiality and dominance of orbits that support triaxial or prolate shapes (Jesseit et al. 2005, 2009; Röttgers et al. 2014). Numerical simulations of binary (disk) mergers often end up with mildly elongated and low angular momentum remnants, with triaxial shapes and prolate-like rotation (Hernquist 1992; Naab & Burkert 2003; Cox et al. 2006; Hoffman et al. 2010; Bois et al. 2011; Moody et al. 2014). More specifically, Tsatsi et al. (2017) emphasised that a polar merger of gas-free disc galaxies can lead to a prolate-like remnant. Ebrová & Łokas (2015), looking at a broader set of merging configurations, found that radial orbits are more likely to produce prolate-like rotation, other orbital configurations (specific combinations of orbital and disk angular momentum) not being excluded.

Similar results are recovered in numerical simulations set within a cosmological context. Cosmological zoom-in simulations produce galaxies with prolate-like rotation (Naab et al. 2014). The Illustris (Vogelsberger et al. 2014), EAGLE (Schaye et al. 2015) and cosmo-OWLS (Le Brun et al. 2014) numerical simulations find that there is an increasing fraction of (close to) prolate shapes among the most massive galaxies (Velliscig et al. 2015; Li et al. 2016, for EAGLE+cosmo-OWLs and Illustris, respectively). Major mergers seem to be ubiquitous among galaxies with prolate-like rotation (Ebrová & Łokas 2017). Specifically, a late (almost dry) major merger seems to be crucial to decrease the overall angular momentum and imprints the prolate-like rotation. A recent study by Li et al. (2018) on the origin of prolate galaxies in the Illustris simulation, shows that they are formed by late ($z < 1$) major dissipation-less mergers: galaxies might have a number of minor or intermediate mass mergers, but the last and late major merger is the main trigger for the prolate shape. Similarly to the findings from

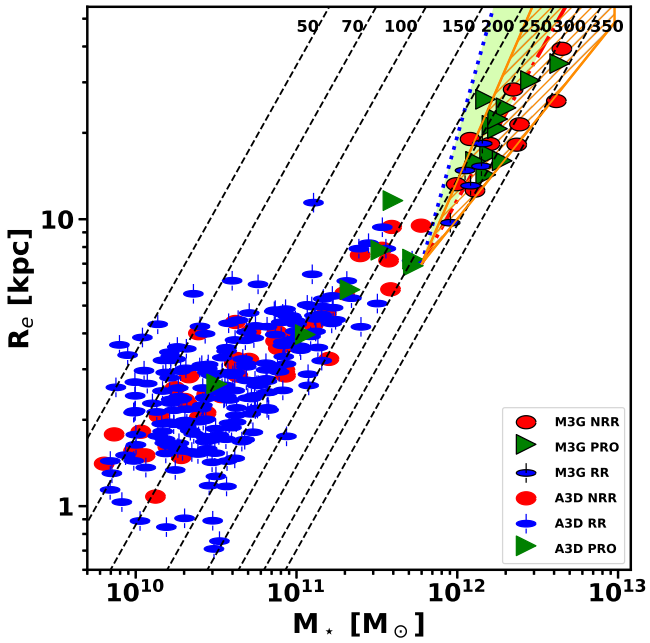

Figure 4. The distribution of the M3G sample on the mass size plane. The M3G sample is shown with symbols that have black edges and dominate the high-mass end. For reference we also show galaxies from the ATLAS^{3D} sample with coloured symbols. The shape and the colour of the symbol is related to the kinematic type as indicated in the legend. The classification is taken from Krajnović et al. (2011) with the following meanings: RR - regular rotation, NRR - non-regular rotation, and PRO - prolate-like rotation (nominally the latter are part of the NRR group, but we highlight them here). Diagonal dashed lines are lines of constant velocity dispersion calculated using the virial mass estimator. The green shaded region shows the expected region where galaxies growing through dissipation-less mergers should lie, assuming major 1:1 mergers (dot-dashed red line) and multiple minor mergers (dotted blue line). The orange hatched region encompasses the mass - size evolution of major merger remnants depending on the merger orbital parameters, as explained in Section 4.

[8] We excluded NGC 5485 as it is already in ATLAS^{3D} sample. UGC10695 is only a candidate for prolate-like rotation.

idealised binary mergers, most mergers leading to prolate-like systems have radially biased orbital configurations. Lower-mass remnants may allow a broader set of possible orbital parameters, mass ratios as well as gas content among the (higher angular momentum) progenitors leading to prolate-like rotation (Ebrová & Łokas 2017).

Prolate-like rotation does not strictly imply that the galaxy has a prolate mass distribution (or potential). This is nicely illustrated with idealised Stäckel potentials, where prolate systems allow only inner and outer long-axis tube orbits (de Zeeuw 1985). Hence prolate galaxies can have velocity maps that either show prolate-like rotation or no-rotation. This is indeed found for the Illustris prolate-like galaxies; about 51% of actually prolate galaxies (using a tri-dimensional account of the mass distribution) show prolate-like rotation while the others have no net rotation (Li et al. 2018), presumably as they contain both prograde and retrograde long-axis tube orbits. Nevertheless, galaxies with prolate-like rotation cannot be oblate spheroids.

Velocity maps of the M3G sample objects with prolate-like rotation show spatial variations, sometimes changing at larger radii to rotation around the major axis. This suggests more complex shapes, supporting various types of orbital families (de Zeeuw & Franx 1991). A classical example of such galaxies is NGC 4365 (Bender 1988), which has a large KDC and outer prolate-like rotation. Its orbital distribution is complex with both short- and long-axis tubes responsible for the formation of the observed (luminosity-weighted) kinematics (van den Bosch et al. 2008). This is also a characteristic of high-mass merger remnants, which often contain a large fraction of box orbits, short- and long-axis tubes, varying relatively to each other with radius (e.g. Röttgers et al. 2014). With such caveats in mind, it is worth assuming for a moment that M3G galaxies with prolate-like rotation are actually significantly triaxial and close to being prolate. Prolate galaxies in the Illustris simulation are found only at masses larger than 3×10^{11} $M_\odot$, and above 10^{12} $M_\odot$ 62 per cent of galaxies are prolate or triaxial, 43 per cent being prolate (Li et al. 2018). This is coincidentally close to our observed fraction of prolate-like systems (44%) within the M3G sample, although we should stress that the M3G sample is not a complete or representative sample.

Notwithstanding the actual frequency and shape of galaxies with prolate-like rotation, they cluster in a special region of the mass - size diagram, as Fig. 4 shows. The M3G sample lies on an extension of the arm-like protuberance arising from the cloud of galaxies at high masses and large sizes. The M3G data extend this arm by almost an order of magnitude in mass and a factor of 5 in size. At masses below 6×10^{11} $M_\odot$ covered by previous surveys, galaxies that were found on this extension were typically old and metal-rich slow rotators characterised by a deficit of light (cores) in their nuclear surface brightness profiles (Emsellem et al. 2011; Cappellari et al. 2013a; Krajnović et al. 2013; McDermid et al. 2015). Specifically, their kinematic properties and the core-like light profiles were used as an indication that the formation of these galaxies was different from other galaxies populating the mass - size plane, which are characterised as star-forming disks, or bulge dominated, oblate and fast rotating early-type galaxies (Cappellari et al. 2013a; Cappellari 2016). The most likely formation process of galaxies populating that extension is through dissipation-less mergers of already massive galaxies: these may provide a way to explain their kinematics, low angular momentum content, cores in light profiles (through binary black hole mergers, e.g. Ebisuzaki et al. 1991; Milosavljević & Merritt 2001) and old stellar populations.

The M3G extension of the arm supports this picture in two additional ways. Firstly, it shows that while these galaxies span a large range in both mass and size, their effective velocity dispersions are not very different, as expected in major dissipation-less mergers (e.g. Hopkins et al. 2009; Bezanson et al. 2009; Naab et al. 2009). Following the argument outlined in Naab et al. (2009), if a massive galaxy grows via equal-mass mergers (of progenitors with similar sizes and/or velocity dispersions), both the mass and the size of the remnant will increase by a factor of 2, while it will follow a line of constant velocity dispersion in Fig. 4. We illustrate this path with a red dot-dashed line, where products of consecutive equal-mass mergers would fall, for example starting with systems of M= 6×10^{11} $M_\odot$ and R_e = 7 kpc, representative of the most massive galaxies in the local Universe. The same increase in mass achieved through multiple minor mergers (with smaller mass, size and velocity dispersion progenitors) would lead to a size increase by a factor of 4, while the velocity dispersions would typically be reduced by a factor of 2. This corresponds to the blue dotted line in Fig. 4, starting from the same main galaxy progenitor (see also fig. 2 in Bezanson et al. 2009).

Equal mass merger simulations show that the relation between the mass and the size of galaxies also depends on the merger parameters, such as the pericentric distance, type of the orbit and its angular momentum (Boylan-Kolchin et al. 2006). This study showed that depending on the merger orbit, the mass - size relations follows $R_e \sim M_*^\alpha$, where $\alpha = 0.7-1.3$. We add this range of possibilities on Fig. 4 as a hatched region, indicating the possible location for massive galaxies after major mergers, and fully encompassing M3G sample galaxies. A caveat in this simple argument is that some of the massive galaxies today will start merging as more compact objects in the early Universe, as is evident from the evolution of the mass - size relation with redshift (van der Wel et al. 2014) and implied by compact size of high redshift quiescent galaxies and their subsequent evolution (e.g. van Dokkum et al. 2008, 2010).

Inevitably the merger history of massive galaxies will be a combination of multiple minor mergers and a small number of major (or even equal) mass mergers (e.g De Lucia & Blaizot 2007; Johansson et al. 2012; Naab et al. 2014). The evidence for such a combination is visible in the differences between the central region (about 1 R_e) and the outskirts, as they often do not share the same kinematics or stellar populations, which will be the topic of future papers. The tightness of the region on the mass - size diagram within which the M3G galaxies lie suggests that the growth of the most massive galaxies ($> 10^{12}$ $M_\odot$) and, in particular, BCGs is dominated by major mergers. This would be consistent with the findings by Li et al. (2018) that also links such massive mergers with prolate-like rotation. Given that more than half of the BCGs in our sample exhibits prolate-like rotation, we speculate that indeed most of these experienced a late major (dry) merger, between two massive (possibly both central) galaxies. A radial bias in the orbital configurations for such mergers leading to an increase fraction of prolate-like rotators may naturally emerge from the preset of phase-space distribution of massive galaxies, also relative to the large-scale structures (West et al. 1995; Niederste-Ostholt et al. 2010; West et al. 2017).

5 CONCLUSIONS

In this work, we report that a large fraction of galaxies more massive than 10^{12} $M_\odot$ show prolate-like rotation. This is shown by the analysis of MUSE data of the magnitude-limited sample of massive galaxies in the Shapley Super Cluster and a matching (in luminos-

ity) sample of BCGs. This M3G sample consists of 25 galaxies, of which 14 are BCGs, 11 are satellites in the SSC and 3 are BCGs in the SSC. We present their stellar velocity maps, and measure their kinematic misalignment angles, showing that 44 per cent of galaxies in the M3G sample have their main rotation *around* their major axes. Selecting only BCGs the fraction increases to 57 per cent, while in a magnitude limited subsample of satellites, prolate-like rotation is detected in 35 per cent of galaxies.

The prolate-like rotation is suggestive of a triaxial or close to prolate intrinsic shape. For most of our galaxies rotation amplitudes are low, but velocity maps typically shows net streaming. These kinematics indicate a violent assembly history, with at least one major dissipation-less merger. The M3G data support a scenario where the final growth of the most massive galaxies is dominated by late dissipation-less merging of similar mass systems. This could be associated with the prevalence of prolate-like rotation in the most massive BCGs and is consistent with the location of these systems within a mass - size diagram, which we extend by almost an order of magnitude in mass and a factor of 5 in size.

The current sample suggests that there is a rather narrow path for climbing the last rung of the galaxy mass ladder, which would be characteristic of dense cluster environments. Answering whether or not such very massive systems require the merging of already central systems would require a more extended studies and a closer look at relevant simulations. The fact that BCGs seem to show an alignment trend with respect to the larger-scale structures may be a interesting avenue to consider, as it would naturally explain a bias in the orbital configuration for equal-mass massive and late mergers. Interestingly enough, prolate-like rotation is also found in lower-mass galaxies (e.g. as seen by the ATLAS^{3D} and the CALIFA surveys, as well in some dwarf galaxies). This further suggests that galaxies with prolate-like rotation should be present in low galactic density regions, while the progenitors may be quite different (i.e. gas-rich).

ACKNOWLEDGEMENTS

We wish to thank Joop Schaye, Michael Maseda and Marijn Franx for useful discussions and the full MUSE GTO team for support during observations and preliminary work on this paper. We thank Chung-Pei Ma and the MASSIVE team for sharing their results on the kinematic misalignment. This research has made use of the NASA/IPAC Extragalactic Database (NED) which is operated by the Jet Propulsion Laboratory, California Institute of Technology, under contract with the National Aeronautics and Space Administration. This research made use of Astropy, a community-developed core Python package for Astronomy (Astropy Collaboration, 2013).

REFERENCES

Abell G. O., Corwin, Jr. H. G., Olowin R. P., 1989, ApJS, 70, 1
Arnold J. A. et al., 2014, ApJ, 791, 80
Bacon R. et al., 2010, in Proc. SPIE, Vol. 7735, Ground-based and Airborne Instrumentation for Astronomy III, p. 773508
Barrera-Ballesteros J. K. et al., 2015, A&A, 582, A21
Bender R., 1988, A&A, 202, L5
Bender R., Saglia R. P., Gerhard O. E., 1994, MNRAS, 269, 785
Bezanson R., van Dokkum P. G., Tal T., Marchesini D., Kriek M., Franx M., Coppi P., 2009, ApJ, 697, 1290
Bois M. et al., 2011, MNRAS, 416, 1654
Boylan-Kolchin M., Ma C.-P., Quataert E., 2006, MNRAS, 369, 1081
Brough S., Proctor R., Forbes D. A., Couch W. J., Collins C. A., Burke D. J., Mann R. G., 2007, MNRAS, 378, 1507
Brough S. et al., 2017, ArXiv e-prints
Cappellari M., 2002, MNRAS, 333, 400
Cappellari M., 2013, ApJ, 778, L2
Cappellari M., 2016, ARA&A, 54, 597
Cappellari M. et al., 2006, MNRAS, 366, 1126
Cappellari M., Copin Y., 2003, MNRAS, 342, 345
Cappellari M., Emsellem E., 2004, PASP, 116, 138
Cappellari M. et al., 2007, MNRAS, 379, 418
Cappellari M. et al., 2011a, MNRAS, 413, 813
Cappellari M. et al., 2011b, MNRAS, 416, 1680
Cappellari M. et al., 2013a, MNRAS, 432, 1862
Cappellari M. et al., 2013b, MNRAS, 432, 1709
Cox T. J., Dutta S. N., Di Matteo T., Hernquist L., Hopkins P. F., Robertson B., Springel V., 2006, ApJ, 650, 791
Davies R. L., Efstathiou G., Fall S. M., Illingworth G., Schechter P. L., 1983, ApJ, 266, 41
Davies R. L., Illingworth G., 1983, ApJ, 266, 516
De Lucia G., Blaizot J., 2007, MNRAS, 375, 2
de Zeeuw P. T., 1985, MNRAS, 216, 273
de Zeeuw T., Franx M., 1991, ARA&A, 29, 239
Dekel A., Sari R., Ceverino D., 2009, ApJ, 703, 785
Ebisuzaki T., Makino J., Okumura S. K., 1991, Nature, 354, 212
Ebrová I., Łokas E. L., 2015, ApJ, 813, 10
Ebrová I., Łokas E. L., 2017, ArXiv e-prints
Eddington A. S., 1915, MNRAS, 76, 37
Emsellem E. et al., 2011, MNRAS, 414, 888
Emsellem E. et al., 2007, MNRAS, 379, 401
Emsellem E. et al., 2004, MNRAS, 352, 721
Emsellem E., Krajnović D., Sarzi M., 2014, MNRAS, 445, L79
Ene I., Ma C.-P., Veale M., Greene J. E., Thomas J., Blakeslee J. P., Walsh J. L., Ito J., 2018, ArXiv e-prints
Falcón-Barroso J. et al., 2017, A&A, 597, A48
Falcón-Barroso J., Sánchez-Blázquez P., Vazdekis A., Ricciardelli E., Cardiel N., Cenarro A. J., Gorgas J., Peletier R. F., 2011, A&A, 532, A95
Fogarty L. M. R. et al., 2015, MNRAS, 454, 2050
Franx M., Illingworth G., de Zeeuw P. T., 1991, ApJ, 383, 112
Gerhard O. E., 1993, MNRAS, 265, 213
Guérou A. et al., 2017, A&A, 608, A5
Hernquist L., 1992, ApJ, 400, 460
Ho N. et al., 2012, ApJ, 758, 124
Hoffman L., Cox T. J., Dutta S., Hernquist L., 2010, ApJ, 723, 818
Hopkins P. F., Hernquist L., Cox T. J., Keres D., Wuyts S., 2009, ApJ, 691, 1424
Houghton R. C. W. et al., 2013, MNRAS, 436, 19
Illingworth G., 1977, ApJ, 218, L43
Jarrett T. H., Chester T., Cutri R., Schneider S., Skrutskie M., Huchra J. P., 2000, AJ, 119, 2498
Jesseit R., Cappellari M., Naab T., Emsellem E., Burkert A., 2009, MNRAS, 397, 1202
Jesseit R., Naab T., Burkert A., 2005, MNRAS, 360, 1185
Jimmy, Tran K.-V., Brough S., Gebhardt K., von der Linden A., Couch W. J., Sharp R., 2013, ApJ, 778, 171
Johansson P. H., Naab T., Ostriker J. P., 2012, ApJ, 754, 115
Kaviraj S., Devriendt J., Dubois Y., Slyz A., Welker C., Pichon C., Peirani S., Le Borgne D., 2015, MNRAS, 452, 2845
Kereš D., Katz N., Fardal M., Davé R., Weinberg D. H., 2009, MNRAS, 395, 160
Krajnović D. et al., 2008, MNRAS, 390, 93
Krajnović D., Cappellari M., de Zeeuw P. T., Copin Y., 2006, MNRAS, 366, 787
Krajnović D. et al., 2011, MNRAS, 414, 2923
Krajnović D. et al., 2013, MNRAS, 433, 2812
Krajnović D. et al., 2015, MNRAS, 452, 2

Lagos C. d. P., Schaye J., Bahe Y., van de Sande J., Kay S., Barnes D., Davis T., Dalla Vecchia C., 2017, ArXiv e-prints
Laine S., van der Marel R. P., Rossa J., Hibbard J. E., Mihos J. C., Böker T., Zabludoff A. I., 2003, AJ, 126, 2717
Le Brun A. M. C., McCarthy I. G., Schaye J., Ponman T. J., 2014, MNRAS, 441, 1270
Li H., Li R., Mao S., Xu D., Long R. J., Emsellem E., 2016, MNRAS, 455, 3680
Li H., Mao S., Emsellem E., Xu D., Springel V., Krajnović D., 2018, MNRAS, 473, 1489
Łokas E. L., Ebrová I., Pino A. d., Semczuk M., 2014, MNRAS, 445, L6
Loubser S. I., Sansom A. E., Sánchez-Blázquez P., Soechting I. K., Bromage G. E., 2008, MNRAS, 391, 1009
Ma C.-P., Greene J. E., McConnell N., Janish R., Blakeslee J. P., Thomas J., Murphy J. D., 2014, ApJ, 795, 158
McDermid R. M. et al., 2015, MNRAS, 448, 3484
Merluzzi P. et al., 2015, MNRAS, 446, 803
Merluzzi P., Mercurio A., Haines C. P., Smith R. J., Busarello G., Lucey J. R., 2010, MNRAS, 402, 753
Metcalfe N., Godwin J. G., Spenser S. D., 1987, MNRAS, 225, 581
Milosavljević M., Merritt D., 2001, ApJ, 563, 34
Moody C. E., Romanowsky A. J., Cox T. J., Novak G. S., Primack J. R., 2014, MNRAS, 444, 1475
Naab T., Burkert A., 2003, ApJ, 597, 893
Naab T., Johansson P. H., Ostriker J. P., 2009, ApJ, 699, L178
Naab T. et al., 2014, MNRAS, 444, 3357
Niederste-Ostholt M., Strauss M. A., Dong F., Koester B. P., McKay T. A., 2010, MNRAS, 405, 2023
Oliva-Altamirano P. et al., 2017, AJ, 153, 89
Qu Y. et al., 2017, MNRAS, 464, 1659
Rodriguez-Gomez V. et al., 2016, MNRAS, 458, 2371
Röttgers B., Naab T., Oser L., 2014, MNRAS, 445, 1065
Ryś A., Falcón-Barroso J., van de Ven G., 2013, MNRAS, 428, 2980
Sánchez-Blázquez P. et al., 2006, MNRAS, 371, 703
Schaye J. et al., 2015, MNRAS, 446, 521
Schechter P. L., Gunn J. E., 1979, ApJ, 229, 472
Scott N., Davies R. L., Houghton R. C. W., Cappellari M., Graham A. W., Pimbblet K. A., 2014, MNRAS, 441, 274
Shapley H., 1930, Harvard College Observatory Bulletin, 874, 9
Skrutskie M. F. et al., 2006, AJ, 131, 1163
Statler T. S., 1991, AJ, 102, 882
Tsatsi A., Lyubenova M., van de Ven G., Chang J., Aguerri J. A. L., Falcón-Barroso J., Macciò A. V., 2017, A&A, 606, A62
van de Sande J. et al., 2017, ApJ, 835, 104
van den Bosch R. C. E., van de Ven G., Verolme E. K., Cappellari M., de Zeeuw P. T., 2008, MNRAS, 385, 647
van der Marel R. P., Franx M., 1993, ApJ, 407, 525
van der Wel A. et al., 2014, ApJ, 788, 28
van Dokkum P. G. et al., 2008, ApJ, 677, L5
van Dokkum P. G. et al., 2010, ApJ, 709, 1018
Veale M., Ma C.-P., Greene J. E., Thomas J., Blakeslee J. P., McConnell N., Walsh J. L., Ito J., 2017a, ArXiv e-prints
Veale M. et al., 2017b, MNRAS, 464, 356
Velliscig M. et al., 2015, MNRAS, 453, 721
Vogelsberger M. et al., 2014, MNRAS, 444, 1518
Wagner S. J., Bender R., Moellenhoff C., 1988, A&A, 195, L5
Weaver J. R. et al., 2018, ArXiv e-prints
Weijmans A.-M. et al., 2014, MNRAS, 444, 3340
Weilbacher P. M., Streicher O., Urrutia T., Pécontal-Rousset A., Jarno A., Bacon R., 2014, in Astronomical Society of the Pacific Conference Series, Vol. 485, Astronomical Data Analysis Software and Systems XXIII, Manset N., Forshay P., eds., p. 451
West M. J., de Propris R., Bremer M. N., Phillipps S., 2017, Nature Astronomy, 1, 0157
West M. J., Jones C., Forman W., 1995, ApJ, 451, L5
Williams R. J., Quadri R. F., Franx M., 2011, ApJ, 738, L25
Wright E. L., 2006, PASP, 118, 1711

This paper has been typeset from a TEX/LATEX file prepared by the author.

ApJ Accepted 6 February 2018
Preprint typeset using LaTeX style emulateapj v. 01/23/15

H I KINEMATICS ALONG THE MINOR AXIS OF M82

Paul Martini[1,2], Adam K. Leroy[1], Jeffrey G. Mangum[3], Alberto Bolatto[4], Katie M. Keating[5], Karin Sandstrom[6], Fabian Walter[7]

ApJ Accepted 6 February 2018

ABSTRACT

M82 is one of the best studied starburst galaxies in the local universe, and is consequently a benchmark for studying star formation feedback at both low and high redshift. We present new VLA H I observations that reveal the cold gas kinematics along the minor axis in unprecedented detail. This includes the detection of H I up to 10 kpc along the minor axis toward the South and beyond 5 kpc to the North. A surprising aspect of these observations is that the line-of-sight H I velocity decreases substantially from about 120 km s^{-1} to 50 km s^{-1} from 1.5 to 10 kpc off the midplane. The velocity profile is not consistent with the H I gas cooling from the hot wind. We demonstrate that the velocity decrease is substantially greater than the deceleration expected from gravitational forces alone. If the H I consists of a continuous population of cold clouds, some additional drag force must be present, and the magnitude of the drag force places a joint constraint on the ratio of the ambient medium to the typical cloud size and density. We also show that the H I kinematics are inconsistent with a simple conical outflow centered on the nucleus, but instead require the more widespread launch of the H I over the ~ 1 kpc extent of the starburst region. Regardless of the launch mechanism for the H I gas, the observed velocity decrease along the minor axis is sufficiently great that the H I may not escape the halo of M82. We estimate the H I outflow rate is much less than 1 M$_\odot$ yr^{-1} at 10 kpc off the midplane.

Keywords: galaxies: individual(M82 – galaxies: ISM – galaxies: starburst – intergalactic medium – ISM: jets and outflows – ISM: molecules

1. INTRODUCTION

Galaxies with substantial star formation rates often have large-scale winds that represent material flowing out of the galaxy along the minor axis (e.g. Heckman et al. 1990; Veilleux et al. 2005). These winds are most likely driven by young, massive stars, which have substantial stellar winds and explode as core-collapse supernovae. The material in these winds can entrain all phases of the interstellar medium, and is expected to be preferentially metal-enriched by the nucleosynthetic products in supernova ejecta. If the material in these winds escapes the galaxy, the winds can enrich the circumgalactic and intergalactic medium (e.g. Borthakur et al. 2013; Werk et al. 2016) and regulate the growth and metal-enrichment histories of galactic disks (e.g. Oppenheimer & Davé 2008; Peeples & Shankar 2011). Observational evidence of the removal of metal-encirched material includes the metallicity of the intergalactic medium, the mass-metallicity relationship, and the sizes and luminosities of galactic disks.

M82 is arguably one of the best-studied galaxies with a starburst-driven wind (Lynds & Sandage 1963). Its two key properties are its proximity at only $D = 3.63$ Mpc (Freedman et al. 1994; Gerke et al. 2011) in the M81 group and that the galaxy is observed nearly edge on, which makes it particularly well-suited to observe the outflow along the minor axis. Studies of this galaxy across the electromagnetic spectrum have detected multiple phases of the wind moving at multiple velocities, ranging from plasma temperatures of $30 - 80$ million Kelvin at X-ray energies (Schaaf et al. 1989; Strickland & Heckman 2009) to warm, ionized gas traced by visible-wavelength features such as Hα (McKeith et al. 1995; Westmoquette et al. 2009) to atomic H I and molecular gas at temperatures of 100 K or less (Seaquist & Clark 2001; Walter et al. 2002; Salak et al. 2013; Leroy et al. 2015).

Observations of visible emission lines along the minor axis showed line splitting in position velocity diagrams (Axon & Taylor 1978; Amirkhanyan et al. 1982), and subsequent Fabry-Perot data exhibited good evidence for a large-scale, biconical outflow (Bland & Tully 1988). The region with double-peaked emission lines begins about 300 pc from the midplane and has been detected to about 1 kpc (Heckman et al. 1990). McKeith et al. (1995) derived an inclination of 80° for the galactic disk, and a cone opening angle of 30° (semi-angle 15°) at > 1 kpc. Their model starts as a cylindrical flow and transitions to a bicone at about 300 pc, and then radially accelerates to a terminal velocity of 600 km s^{-1} on the surface of the bicone. The material inside the bicone is the much hotter fluid observed at X-ray energies and predicted to have a terminal velocity several times greater than the ~ 500 km s^{-1} escape velocity (Strickland & Heckman

[1] Department of Astronomy, The Ohio State University, Columbus, OH 43210, USA, martini.10@osu.edu, leroy.42@osu.edu
[2] Center for Cosmology and Astroparticle Physics, The Ohio State University, Columbus, OH 43210, USA
[3] National Radio Astronomy Observatory, 520 Edgemont Road, Charlottesville, VA 22903, USA
[4] Department of Astronomy, University of Maryland, College Park, MD 20742, USA
[5] Rincon Research Corporation, 101 North Wilmot Road, Suite 101, Tucson, AZ 85711, USA
[6] Department of Physics, University of California, San Diego, CA 92093, USA
[7] Max-Planck-Institute für Astronomie, Königstuhl 17, D-69117 Heidelberg, Germany

2009).

The line of sight velocities of $120-140$ km s^{-1} relative to systemic for the cold atomic and molecular gas traced by H I and CO are substantially slower than the emission traced at shorter wavelengths. The cold gas could be entrained in the hot gas, although simulations suggest that only a small fraction of the cold gas should survive a significant amount of acceleration (Scannapieco & Brüggen 2015; Schneider & Robertson 2017), except perhaps if the clouds are supported by magnetic fields (McCourt et al. 2015). Another possibility is that the winds are driven by radiation pressure through momentum transfer from starlight to dust grains embedded in the gas (Murray et al. 2005, 2010; Andrews & Thompson 2011). Recent hydrodynamic simulations by Zhang et al. (2017) suggest that clouds accelerated by the radiation field last significantly longer than clouds entrained in the hot outflow. Both the atomic and molecular gas show double-peaked lines that suggest the hot, conical outflow is bounded by a sheath of cooler material (Walter et al. 2002). Leroy et al. (2015) conclude that the cold H I and CO help to confine the hot outflow. The best evidence for this connection begins approximately 1.5 kpc from the disk. At these distances the H I and CO exhibit double-peaked profiles indicative of a bicone, a velocity gradient consistent with the outflow, and spatial coincidence with features at other wavelengths (see Figure 16 in Leroy et al. 2015).

In this paper we present new, wide-field H I observations of M82 obtained with the Karl G. Jansky Very Large Array (VLA) combined with previous observations with the 100-m Robert C. Byrd Green Bank Telescope (GBT). These observations show the H I intensity and kinematics over approximately $20' \times 20'$ with a resolution of $24''$. Based on the distance $D = 3.63$ Mpc, 1kpc $\approx 1'$. These observations therefore trace the H I outflow up to a projected distance of 10 kpc along the minor axis. The next section describes our observations in further detail, and the following section presents a mass model for M82. We use this mass model in §4 to explore various explanations for the minor axis kinematics, and summarize our results in §5. Except where otherwise noted, we adopt an inclination of 80° for the disk of M82 (Lynds & Sandage 1963; McKeith et al. 1993).

2. OBSERVATIONS

We observed M82 in the L band with the VLA in the B, C, and D configurations in 2015 and 2016, and combined these data with L band observations from the GBT obtained between 2003 and 2009. The VLA observations were centered on M82 at $\alpha = 9{:}55{:}52.72$, $\delta = +69{:}40{:}45.7$ (J2000), and on-source integration times in the B, C, and D configurations were ~ 378, 294, and 168 minutes, respectively. The GBT observations consist of 40 sessions that include the M81/M82 and NGC2403 galaxy groups. The GBT observations were used to construct an $8.7° \times 21.3°$ map centered at $\alpha = 8{:}40{:}37.0$, $\delta = +69{:}17{:}16$ (J2000) and have a total integration time of approximately 187 hours. This GBT map includes data previously described in Chynoweth et al. (2008, 2009, 2011).

2.1. *VLA Data Processing*

We set the VLA correlator to observe the full, polarized L-band continuum with 1 MHz channels across the full range $\sim 1-2$ GHz. We also configured spectral windows to target the H I and OH lines at higher spectral resolution. For the H I line, which is the focus of this paper, we used 2048 3.906 kHz channels centered on the H I line at the velocity of M82. For the OH lines, we used a slightly coarser channel width of 7.812 kHz. We calibrated the amplitude, bandpass, and phase with measurements of 1331+305 (3C 286; amplitude and bandpass; flux density = 15.0 Jy at 1.4 GHz) and J0921 + 6215 (B-configuration phase; flux density = 1.186±0.003 Jy/beam at 1.55 GHz), and J0841 + 7053 (C- and D-configuration phase; flux density = 3.340 ± 0.018 Jy/beam at 1.57 GHz), respectively, using standard techniques. This observation strategy mirrored that used successfully for THINGS, VLA ANGST, and LITTLE THINGS (Walter et al. 2008; Hunter et al. 2012; Ott et al. 2012). While M82 was extensively observed by the VLA in the 1980s (Yun et al. 1993, 1994), the current observations are more sensitive, have higher velocity resolution, and have much better dynamic range due to upgrades from the early 1990s to late 2000s that improved sensitivity and bandwidth. The later is particularly important, given M82's substantial continuum emission.

As the continuum emission from M82 is quite strong, we self-calibrated all measurements. The reduction in phase residual following self-calibration resulted in a factor of three to five improvement in peak signal-to-noise for all measurements. After self-calibration, we split out the spectral window containing H I, binning the data to have 8s integrations. We identified line free channels from the integrated spectrum of the $u-v$ data. We then fit and subtracted a first order polynomial from each visibility measurement. We combined all of the continuum-subtracted visibility data for all four observations, in the process binning the data to a final channel width of 5 km s^{-1}.

We imaged the data in stages to account for the substantial absorption in the center of M82, . First, we created a high resolution image with Briggs weighting parameter `robust` = 0 and no $u-v$ taper. This image had a beam size of $\sim 5''$. The surface brightness sensitivity of this image was too poor to study the outflow in detail, but yielded a good initial model of the inner part of the galaxy. We cleaned in interactive mode until the maximum residual appeared comparable to the noise in the image. We then imaged the data again, beginning from the model output by the previous run, and this time used `robust` = 0.5 weighting to emphasize surface brightness sensitivity slightly more. Again, we cleaned until the maximum residual was comparable to the noise. Then, starting from the model output by that imaging run, we imaged the data with an $18''$ $u-v$ taper. This dramatically improved the surface brightness sensitivity of the data. Because this step began with the previous, higher-resolution model, we achieved a substantial improvement in surface brightness sensitivity without significant, negative impact due to the strong absorption in the center. We cleaned this image until the maximum residual again resembled the noise of the image and smoothed the output image to have a round, $24''$ beam (FWHM).

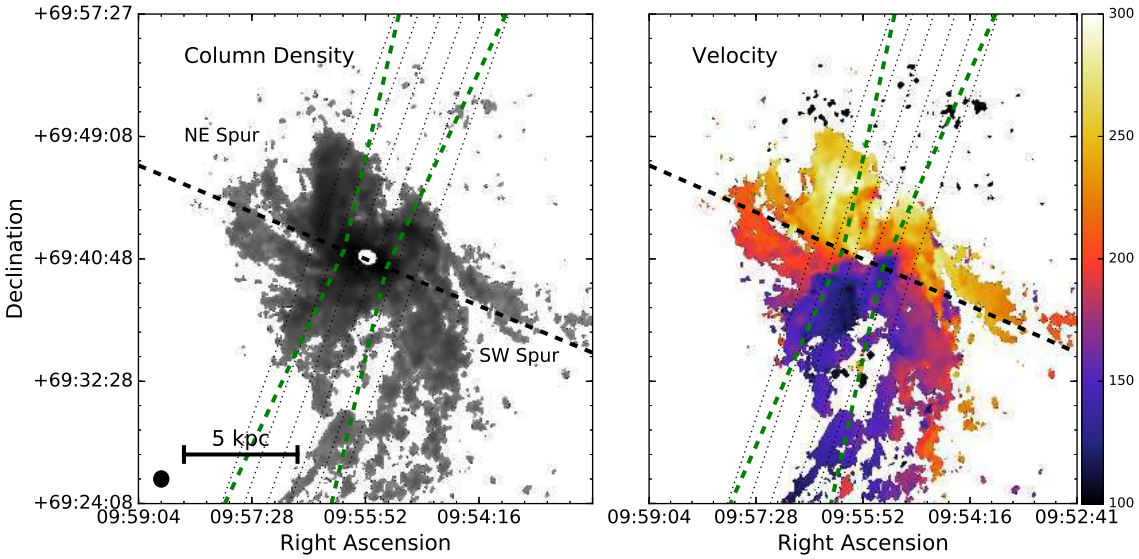

Figure 1. Log of the M82 H I column density (*left*) and velocity field (*right*). The velocity scale in $\mathrm{km\,s^{-1}}$ is shown on the right colorbar. The major axis is oriented at $PA = 67°$ (*black, dashed line*). The outline of our biconical frustum model (*green, dashed line*) is oriented along the minor axis with an opening angle of $\theta = 20°$ (see § 4.2). Also shown are the outlines of various 1 kpc wide slices along the minor axis used to compute position-velocity diagrams and a scale bar with a projected length of 5 kpc. The absence of H I at the center position is because there is H I absorption of the bright continuum source.

2.2. *GBT Data Processing*

The M81/M82 and NGC 2403 area was observed by moving the telescope in declination and sampling every $3'$, with an integration time of 1-3 seconds per sample (the integration time varied with the observation session). Strips of constant declination were spaced by $3'$, and the telescope was moved in right ascension to form a basket weave pattern over the region. The GBT spectrometer was used with a bandwidth of either 12.5 or 50 MHz, depending on the observation session. The combined bandwidth for the final map is 10.5 MHz, and has a velocity range from -890 to $1320\,\mathrm{km\,s^{-1}}$. The typical system temperature for each channel of the dual-polarization receiver was ≈ 20 K.

The GBT data were reduced in the standard manner using the GBTIDL and AIPS data reduction packages. Spectra were smoothed to a channel spacing of 24.4 kHz, corresponding to a velocity resolution of $5.2\,\mathrm{km\,s^{-1}}$. A reference spectrum for each of the nine observation sessions was made from an observation of an emission-free region, usually from the edges of the maps. The reference spectrum was used to perform a (signal-reference)/reference calibration of each pixel. These calibrated spectra were scaled by the system temperature and corrected for atmospheric opacity and GBT efficiency. We adopted the GBT efficiency from equation one of Langston & Turner (2007) for a zenith atmospheric opacity of $\tau_0 = 0.009$. The frequency range observed was relatively free of radio frequency interference (RFI) and less than 0.3% of all spectra were adversely affected. The spectra exhibiting RFI were identified by tabulating the root-mean-square (RMS) noise level in channels free of neutral hydrogen emission. Spectra that showed unusually high noise across many channels were flagged and removed. The observations were then gridded using the AIPS task `SDIMG`, which also averages polarizations. After amplitude calibration and gridding, a 1st-order polynomial was fit to line-free regions of the spectra and subtracted from the gridded spectra using the AIPS task `IMLIN`. The effective angular resolution, determined from maps of 3C286, is $9.15 \pm 0.05'$. To convert to units of flux density, we observed the calibration source 3C286. The calibration from Kelvin to Janskys was derived by mapping 3C286 in the same way that the HI maps were produced, and the scale factor from K/Beam to Jy/Beam is 0.43 ± 0.03. Due to the patchwork nature of the observations, the RMS noise varies considerably across the datacube, ranging between $6-30$ mJy/beam. The average RMS noise in the final data cube is 20 mJy per 24.4 kHz channel.

2.3. *Construction of Combined Data Products*

The VLA-only cube still exhibits "bowling" and other large scale artifacts, in part due to the absence of short and zero spacing data. To deal with this, we combined the VLA cube with the GBT cube. First, we extracted a subcube centered on M82 from the larger M81 GBT survey. We then masked channels dominated by Galactic emission, carried out one additional round of first-order baseline fitting, applied the primary beam taper of the VLA data to the GBT data, and combined the VLA and GBT data with the CASA task `feather`. This combination removed or suppressed most of the large scale artifacts that were present in the VLA-only cube. After the combination, we corrected the cube for the primary beam response of the VLA. The final cube has a channel width of $5\,\mathrm{km\,s^{-1}}$, beam size of $24''$ (FWHM) , and covers the primary beam of the VLA out to its half power point ($\approx 32'$). Before the primary beam correction, the cube had an rms noise of ≈ 0.4 mJy beam^{-1} at this resolution and channel width, equivalent to ≈ 4 K noise for ≈ 1050 K/Jy.

We converted the cube to have units of Kelvin, and also made a version of our H I cube with individual channels in units of column density. To do this we used the 5 km s^{-1} width of each channel and assumed optically

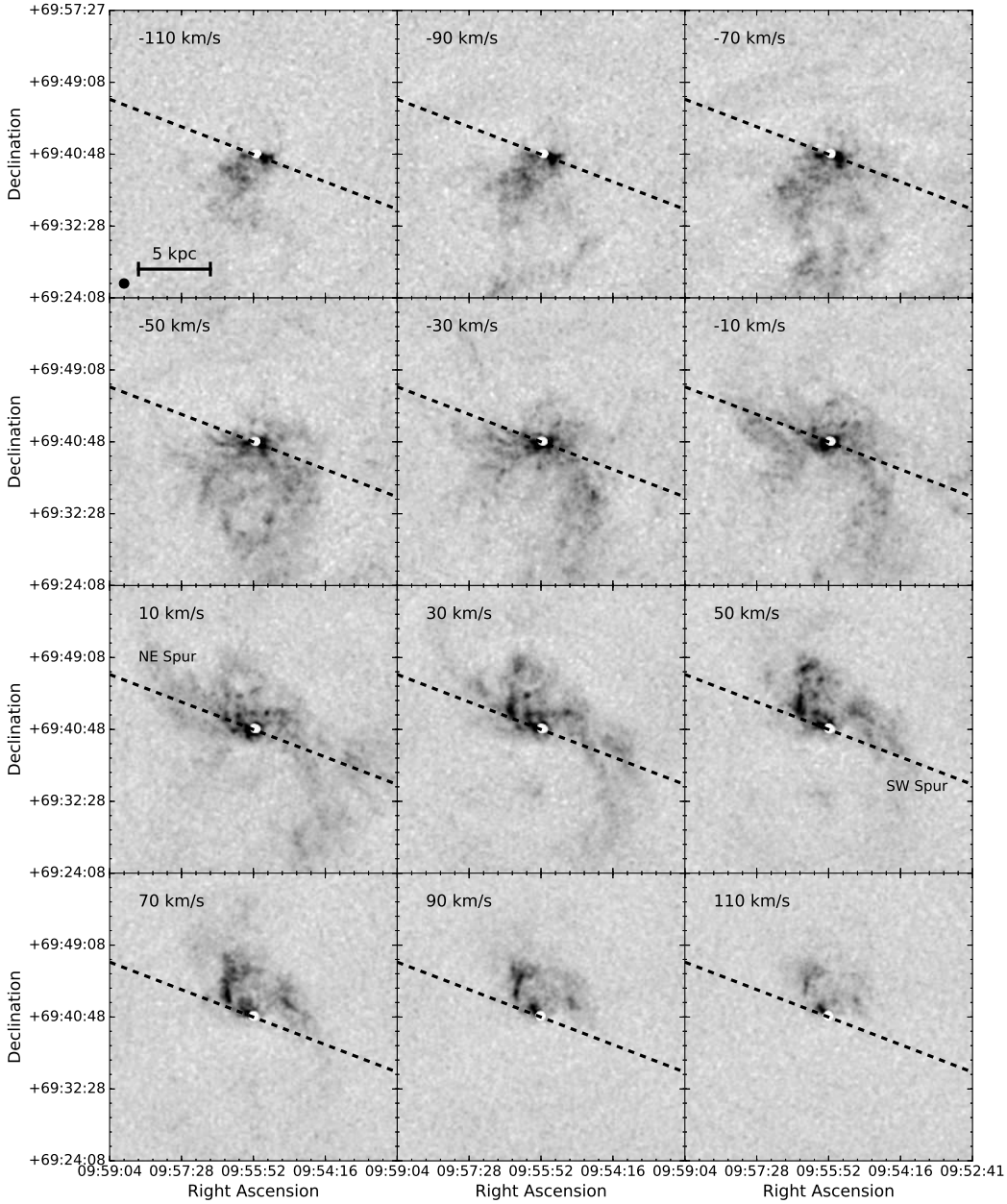

Figure 2. M82 H I intensity in twelve velocity channels after continuum subtraction. The central white area is due to H I absorption toward the center of the galaxy. The velocity for each channel is relative to the systemic velocity of M82. The major axis is oriented at $PA = 67°$ (*black, dashed line*). The projected size of 5 kpc and the 24″ FWHM beam diameter are shown in the upper left panel.

thin H I emission so that $N \approx 1.823 \times 10^{18}\,\mathrm{cm}^{-2}\ I_{HI}$ with I_{HI} in K km s^{-1}. To highlight only bright, positive emission, we also created a mask that included all regions of the cube where the intensity exceeded a signal-to-noise ratio of five over two successive channels. This corresponds to a column density limit of $\approx 7 \times 10^{19}$ cm^2 across a 10 km s^{-1} velocity range. We used this mask to create integrated intensity and intensity-weighted mean velocity maps. Note that most of our analysis focuses on direct analysis of the cubes.

The integrated H I intensity map and velocity field are shown in Figure 1, and channel maps of H I intensity in select velocity channels are shown in Figure 2. The H I intensity map shows substantial H I extending along the major axis for over ±5 kpc. The H I emission to the left (East) shows a significant spur that extends up (North) from the disk starting at about $4 - 5$ kpc. This is the tidal stream seen in previous H I observations (Cottrell 1977; van der Hulst 1979; Appleton et al. 1981; Yun et al. 1993, 1994). This feature is labeled "NE Spur" in Figures 1 and 2. Our data also show some of the extensive pair of streams that extend west of the major axis, and then toward the South (Yun et al. 1993). This feature is labeled "SW Spur" in Figures 1 and 2. The H I emission along the minor axis extends approximately 5 kpc toward the North and 10 kpc toward the South. M82 is to the North of M81, so the southern part of M82 is closer to M81.

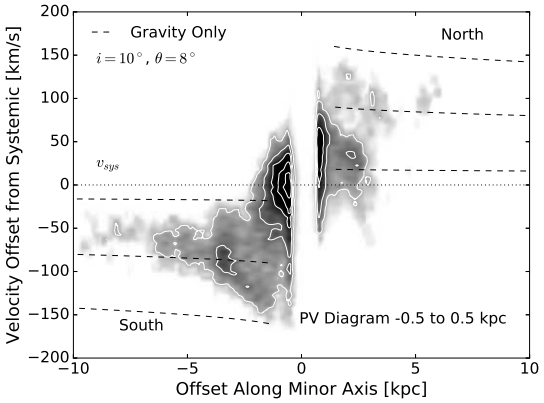

Figure 3. M82 minor axis position-velocity diagram. The grayscale and contours show the integrated H I intensity within ±0.5 kpc along the minor axis as a function of projected distance from the midplane. The velocity field has been shifted to the systemic velocity of 211 km s^{-1} (*dotted line*). H I is clearly detected up to 10 kpc to the South (*left*) and to about 6 kpc to the North (*right*). Also shown are the ballistic velocities for test particles (*dashed lines*) for the mass model presented in §3. Three trajectories are shown in each direction. The central trajectory is aligned with the symmetry axis of a bicone tilted $\theta = 10°$ relative to the plane of the sky, while the other two trajectories are inclined by ±8° relative to the symmetry axis. This simple, ballistic model is not a good match to the data.

The H I velocity field shows some evidence of rotation, similar to the molecular gas (Young & Scoville 1984; Yun et al. 1993; Leroy et al. 2015), although not as regular as the $K-$band stellar rotation curve measured by Greco et al. (2012). The H I rotation curve exhibits several drops in velocity (Sofue et al. 1992), which are most likely due to the influence of the bar (Telesco et al. 1991) and the tidal interaction (Yun et al. 1993). The velocity field along the minor axis has a steep gradient within about 1 kpc, where it decreases rapidly by over 100 km s^{-1} toward the South and increases rapidly by over 100 km s^{-1} toward the North. This spatial extent is where the start of the outflow is observed at other wavelengths (McKeith et al. 1995; Westmoquette et al. 2009). The amplitude of the velocity field then decreases toward the systemic velocity of M82. This is particularly prominent toward the South, where continuous, albeit filamentary, H I is detected out to 10 kpc from the midplane. At this point the velocity has decreased to approximately half the value at 1 kpc. Figure 3 shows a position-velocity diagram along the minor axis within a synthesized slit of width ±0.5 kpc relative to the center of M82. The boundaries of this slit are shown on Figure 1.

3. MASS MODEL

We developed a mass model for M82 based on measurements of the stellar surface photometry, stellar kinematics, and simulations of its interaction history within the M81 group. This model includes a bulge, a disk, and a dark matter halo and was constructed with the `galpy` software package (Bovy 2015). We took the physical length scale of the bulge and disk components from the wide-field, near-infrared surface photometry of Ichikawa et al. (1995). They performed a bulge-disk decomposition and found the bulge light along the major axis is well fit by a de Vaucouleurs $R^{1/4}$ law with an effective radius of 21″ ($K'-$band) to 29″ ($H-$band).

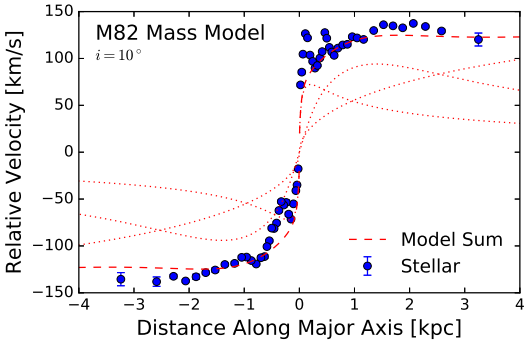

Figure 4. M82 rotation curve model and observations. The data points (with error bars) are the stellar kinematics measured by Greco et al. (2012) with the 2.29μm CO bandhead in the near-infrared $K-$band. The lines show the rotation curve (*dashed*) and three individual components (*dotted*) calculated from the mass model described in §3. The bulge component is the most significant component near the center of the galaxy, the disk dominates out to several kpc, and the halo at larger radii.

We adopt a physical radius of $r_e = 0.36$ kpc for this component, which we model with a Hernquist potential (Hernquist 1990) with $a = 0.2$ kpc (with the relation $a = r_e/1.8153$). Ichikawa et al. (1995) measured an exponential disk scale length of 40″, and we adopt a physical disk of $r_s = 0.6$ kpc. We model the exponential disk with the `galpy` implementation of the Smith et al. (2015) prescription to describe an exponential disk as three Miyamoto-Nagai disks (Miyamoto & Nagai 1975). We set the vertical scale height to $h_z = 0.1$ kpc. This quantity was not calculated by Ichikawa et al. (1995), but the exact choice does not appreciably impact the kinematics above the midplane. Lastly, we model the dark matter halo as a Navarro et al. (1996, NFW) profile. H I observations of the M81 group show long tidal features that are good evidence of past interactions between M81 and M82, as well as between M81 and NGC 3077 (Cottrell 1977; Yun et al. 1993). Oehm et al. (2017) performed a thorough simulation study of various scenarios for the interaction history of the M81 group and placed constraints on the dark matter profiles of the largest members. We adopt their NFW parameters of $R_{200} = 164$ kpc, $\rho_0 = 8.81 \times 10^{-3}$ M$_\odot$ pc^{-3}, and $c = 11.17$.

There are two free parameters in the mass model: the masses of the bulge and disk components. We adjust these parameters until we obtain a reasonably good match to the major axis rotation curve measured by Greco et al. (2012). That rotation curve was measured from the CO 2.29μm bandhead that is prominent in the near-infrared spectra of giant and supergiant stars. This rotation curve is shown in Figure 4, along with the rotation curves of the three mass components. The mass we adopt for the bulge component is 2×10^9 M$_\odot$, although we note that much of this mass may not be in the form of the old stellar population characteristic of classical bulges. One reason is that there is good evidence from stellar spectroscopy that the central light distribution is dominated by young supergiants (Rieke et al. 1993; Förster Schreiber et al. 2001, 2003; Greco et al. 2012), rather than the old stellar population typical of classical bulges. A substantial fraction of the mass in the central region is also in the form of atomic and molecular gas (Young & Scoville 1984; Walter et al.

2002; Leroy et al. 2015). Regardless of the exact form of the mass, this component dominates the rotation curve in the central 0.5 kpc. We normalize the disk component to 8×10^9 $M_\odot$ kpc^{-3}, and this is the most prominent component out to about 2 kpc. The total mass of our model is in good agreement with the total dynamical mass of $\sim 10^{10} M_\odot$ derived by Greco et al. (2012), and the range of $10^{9-10} M_\odot$ derived by previous studies, although those studies analyzed a smaller range of radii (Young & Scoville 1984; Goetz et al. 1990; Sofue et al. 1992).

4. ANALYSIS

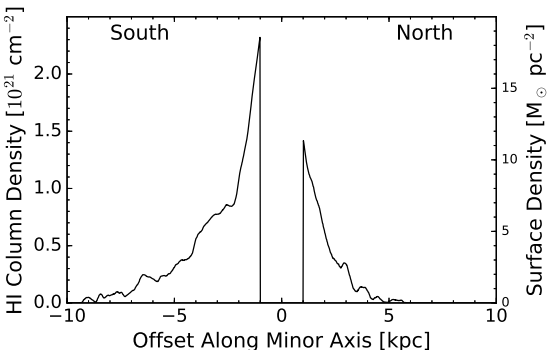

Figure 5. HI column density vs. distance from the midplane in the same ±0.5 kpc region used to construct Figures 3 and 6. The central ±1 kpc is masked as there is significant H I absorption near the midplane. The right axis shows the equivalent surface density of neutral Hydrogen calculated from $8 \times 10^{-21} N_H$.

We detect substantial H I emission along the minor axis out to at least 5 kpc to the North and 10 kpc to the South (Figure 1). The total H I intensity is also greater toward the South than toward the North, and there is more molecular gas and dust to the South (Walter et al. 2002; Leroy et al. 2015). Figure 5 shows the H I column density as a function of distance from the midplane along the minor axis in the same ±0.5 kpc region used to construct Figure 3.

The spatial distribution and kinematics of the H I gas are a poor match to the outflow traced by the hottest gas. Strickland & Stevens (2000) discuss how the hot wind fluid traced by their X-ray observations may accelerate cold clouds by ram pressure. Strickland & Heckman (2009) estimate the terminal velocity of the wind is $v_\infty = 1410 - 2240\,\mathrm{km\,s^{-1}}$, which is greater than the escape velocity of $v_{esc} = 460\,\mathrm{km\,s^{-1}}$ for M82. The minor axis kinematics of the warm, ionized gas traced by Hα and other visible-wavelength lines suggest velocities of $500 - 600\,\mathrm{km\,s^{-1}}$ for an 80° disk inclination (McKeith et al. 1995; Shopbell & Bland-Hawthorn 1998). The velocity of the warm ionized gas is consequently substantially lower than the hot wind fluid, and closer to M82's escape velocity (Heckman et al. 2000). The H I kinematics are similar to the warm, ionized gas, as well as the colder, molecular gas traced by CO (Walter et al. 2002; Leroy et al. 2015). The similar kinematics supports the hypothesis that the warm ionized gas and the cooler atomic and molecular gas are cospatial, but they are not cospatial with the hot wind fluid detected at X-ray energies.

Further evidence that the warm ionized gas and cooler atomic and molecular gas are cospatial comes from measurements of line splitting along the minor axis that suggests both gas phases trace the edge of a bicone that surrounds the higher temperature X-ray fluid. This evidence includes the Fabry-Perot observations of Bland & Tully (1988) and line splitting in longslit spectroscopy. Heckman et al. (1990) used longslit spectroscopy to derive an opening angle of 60° (and angles of $30 - 40$° between the symmetry axis of the cone and the plane of the sky). McKeith et al. (1995) derived a smaller cone opening angle of 30° at > 1 kpc. Line splitting is also observed in the colder gas traced by H I and CO. Leroy et al. (2015) derived a smaller cone opening angle of $13 - 20$° for this cold gas. The velocity spread of the minor axis H I observed in our new observations is more consistent with the smaller opening angle derived by Leroy et al. (2015). A possible explanation for the discrepancy between the measurements from warm, ionized gas and colder atomic gas are that the later measurements were made further from the midplane, where the outflow may be more columnated.

4.1. *Minor Axis Velocity Decrease*

The most remarkable feature of the minor axis H I kinematics is the decrease of the typical velocity amplitude from about $100\,\mathrm{km\,s^{-1}}$ to $50\,\mathrm{km\,s^{-1}}$ over the projected distance range from about 1.5 kpc to 10 kpc (Figure 3). This decline is very obvious along the minor axis toward the South. The kinematics to the North are broadly consistent with this same velocity profile, although the H I intensity is substantially less and the gas is only detected to about 5 kpc in projection.

The velocity amplitude decrease from 1.5 to 10 kpc is not consistent with H I clouds that have been accelerated by the wind and then launched on ballistic trajectories, and consequently demonstrate that an additional force is required. This is because the inferred outflow velocities of these clouds is on order $500 - 600\,\mathrm{km\,s^{-1}}$ (for 80° disk inclination) at a projected height of 1.5 kpc and the mass of M82 is insufficient to slow the clouds by 50% from 1.5 kpc to 10 kpc. This point is illustrated by the dashed lines in Figure 3. The lines show the projected velocity of a test particle calculated with `galpy` and the mass model for M82 developed in §3. The middle line shows the trajectory for a test particle on the symmetry axis of the bicone (at an angle of 10° relative to the plane of the sky) and the other lines show test particles at ±8° on the nominal edges of a cone with a 16° opening angle. The H I kinematics clearly decrease much faster than expected from gravitational forces alone. They are also inconsistent with cooling of the H I gas from the hot wind. H I produced from cooling in a hot wind should have the velocity of the hot wind, which Strickland & Heckman (2009) estimate to be as high as $\sim 2000\,\mathrm{km\,s^{-1}}$. The H I kinematics also demonstrate that the cold H I clouds do not experience continual acceleration, nor even free expansion into the halo of M82.

One possible explanation for this decrease in projected velocity is that the inclination of the bicone is substantially different from the stellar disk, as this would decrease the H I outflow velocity. We find that the H I velocities do diminish by the required amount from $1.5 - 5$ kpc if the symmetry axis of the cone is tilted toward us by

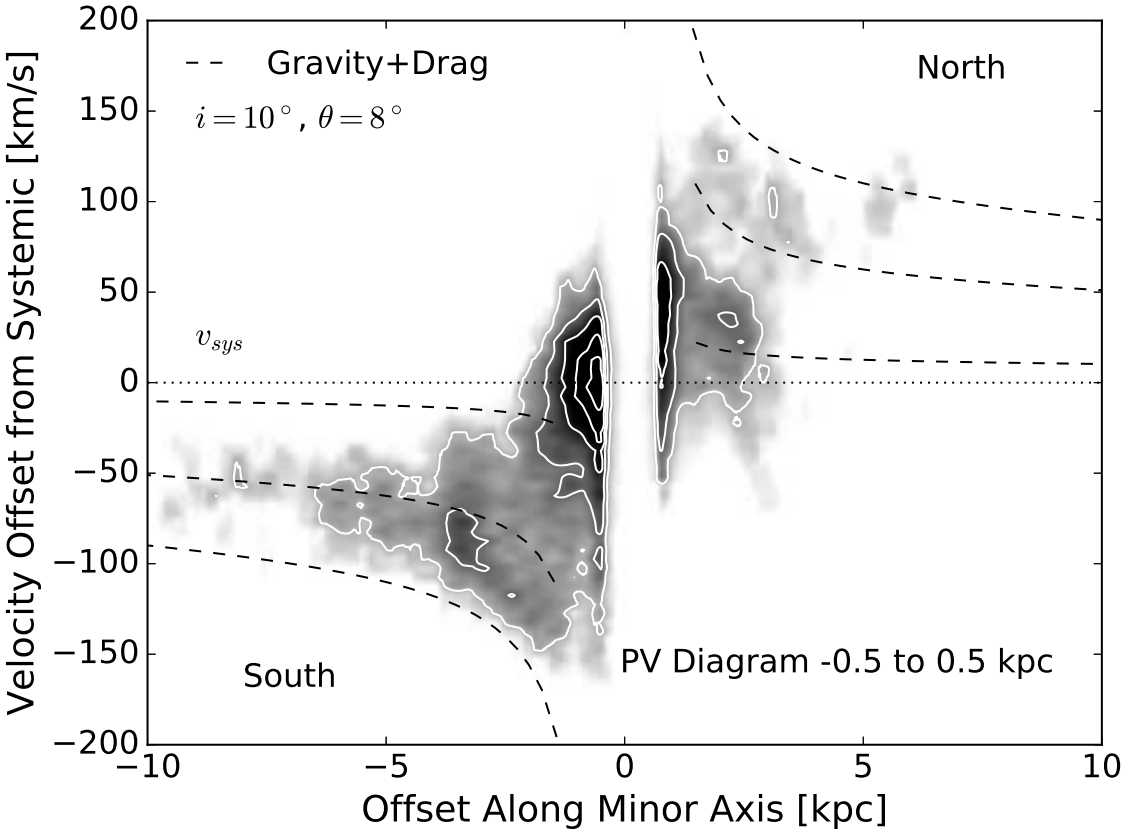

Figure 6. Same as Figure 3 except with a model that includes both gravitational and drag forces on the H I gas.

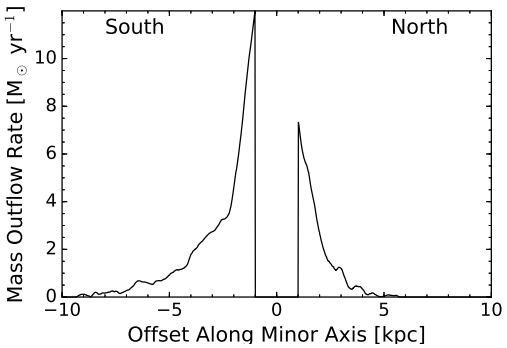

Figure 7. Integrated mass outflow rate within ±0.5 kpc of the minor axis derived from the surface density shown in Figure 5 and the velocity profile of the best-fit model. The central ±1 kpc is masked as there is significant H I absorption near the midplane.

30° relative to the plane of the sky. However, in this case the H I velocities continue to decrease to the systemic velocity, and do not reproduce the relatively flat velocity profile seen from $5-10$ kpc. Other possible explanations include that the H I experiences some additional drag force, the H I does not represent a continuous stream of material, but instead is forming in situ (although not from the hot wind), and that the H I kinematics have been substantially affected by tidal interactions.

If the H I consists of clouds flowing outward along the edge of the bicone, they could experience a drag force if they encounter ambient material outside of the bicone. This material could be halo gas of M82 that is not part of the wind, or tidal material that is approximately stationary relative to the wind. We model the drag force with the drag equation $f_{drag} = C_d \rho_{amb} v^2 A$, where C_d is the drag coefficient, ρ_{amb} is the density of the ambient medium, v is the velocity of the H I relative to this medium, and A is the cross section of a typical H I cloud. We then make the assumption that $C_d \rho_{amb} A \propto r^{-2}$. This would be true if $C_d A$ were constant and $\rho_{amb} \propto r^{-2}$. The coefficient C_d is approximately constant for spheres (of constant cross section A) in a supersonic flow, while $\rho_{amb} \propto r^{-2}$ is characteristic of mass outflow at a constant rate at constant velocity. Based on measurements by Leroy et al. (2015), we expect the density profile is somewhat steeper with $\rho_{amb} \propto r^{-3 \rightarrow -4}$ for the dust and molecular gas[8]. To maintain our assumption in this case would require the drag coefficient to increase with r, which could happen if the Reynolds number decreased with radius. We find that the addition of a drag force with $C_d \rho_{amb} A \propto r^{-2}$ provides a reasonable match to the data. This model is shown in Figure 6.

If the velocity change of the H I gas is due to a drag force imposed by the ambient medium, the non-gravitational deceleration of the test particles that best match the data constrain the product of $C_d \rho_{amb} A_{cl}$. If we assume these are spherical clouds of H I gas with uniform density ρ_{cl} and radius R_{cl}, the non-gravitational

[8] While Leroy et al. (2015) did measure r^{-2} for H I, that is more due to the abundance of tidal material, than because the wind material follows r^{-2}.

deceleration is:

$$\frac{dv}{dt} = \frac{3}{4} C_d \left(\frac{\rho_{amb}}{\rho_{cl}} \right) \frac{v_{cl}^2}{R_{cl}} \quad (1)$$

At 2 kpc from the midplane, the deprojected H I velocity is about $500\,\mathrm{km\,s^{-1}}$ and the best-fit model has a non-gravitational deceleration of $1.8 \times 10^{-7}\mathrm{cm\,s^{-2}}$. For $R_{cl} = 10$ pc, the density ratio is $\sim 0.0044(0.5/C_d)$. If the cloud particle density is $10\,\mathrm{cm^{-3}}$, the ambient medium at 2 kpc from the midplane must be relatively dense with $0.044\,\mathrm{cm^{-3}}$. This is substantially denser than the hot wind, although the wind has much larger velocities so it is unlikely to be the same medium. If drag forces decelerate the H I gas, then the ambient medium responsible for the deceleration must be distinct from the hot wind, and at higher density than the typical hot, coronal gas of galactic halos. This could be due to material stripped out of the disk by the tidal interaction with M81. The tidal interaction may also be the main origin of the decrease in the H I velocity, rather than a drag force due to the ambient medium.

The combination $\rho_{cl} R_{cl}$ in Equation 1 is the column density of the clouds in the outflow. If the majority of the material in the cloud is H I, then this quantity can be measured with H I emission maps or UV/visible absorption line studies with sufficiently high resolution and sensitivity. Such a measurement, combined with the acceleration and the velocity of the clouds, could then be used to solve for the ambient density required to produce the observed deceleration. The angular size of a $\sim 10 - 20$ pc cloud at the distance of M82 is $0.5 - 1''$. This is a challenge for current H I facilities, but may be feasible with UV/visible absorption line studies toward background sources.

Similar to Leroy et al. (2015), we have used the mass distribution and velocity information to derive the mass flux associated with the H I emission. Under the assumption that all of the H I is associated with an outflow, Figure 7 shows the mass flux computed from the product of the mass surface density (Figure 5), the velocity from our outflow model, and the ± 0.5 kpc width of the central region of our position-velocity diagram. The main differences from the calculation and figure shown in Leroy et al. (2015) are that we used a smaller region width (1 kpc, rather than 3 kpc) and we used the velocity profile, rather than a fixed outflow speed of $450\,\mathrm{km\,s^{-1}}$. While the mass flux we have derived near the midplane is lower than in Leroy et al. (2015), largely because of the smaller region width, the mass flux is detected out to about twice the distance from the midplane, although it drops to a fraction of a solar mass per year beyond 4 kpc. This is also approximately the point where the mass flux is comparable to the outflow rate computed by Strickland & Heckman (2009) for the hot gas. This H I outflow rate is about an order of magnitude less than the star formation rate.

The H I velocity decrease along the minor axis may be so substantial that the H I will not escape the halo. At a projected height of 10 kpc, the line of sight velocity has dropped to $50\,\mathrm{km\,s^{-1}}$ relative to the systemic velocity, which corresponds to an inclination-corrected outflow velocity of about $300\,\mathrm{km\,s^{-1}}$. This is sufficiently comparable to the escape velocity of our mass model that the ultimate fate of the gas will depend on assumptions in our model for the drag force on the cold gas, the impact of tidal forces in the M81 group, and the halo model for M82. Within the context of our model, the H I would finally stall at 70–80 kpc after about 500 Myr. The H I gas could consequently form a cold "fountain" as proposed by Leroy et al. (2015), rather than substantially add to the intergalactic medium. We searched in our data for any evidence of material that is falling back, but do not see any. This included a careful inspection of the non-masked data, which has somewhat greater sensitivity, although at the expense of more artifacts.

4.2. *Biconical Frustum*

A simple bicone model is not a good match to the spatial and velocity distribution of the H I gas. Figures 1 and 2 clearly show the H I gas does not have a conical shape. The opening angle derived from line splitting in the cold gas by Leroy et al. (2015) is also smaller than values derived closer to the plane from the warm, ionized gas (Heckman et al. 1990; McKeith et al. 1995), which suggests the cold gas is more columnated. Another argument against a simple bicone is the presence of outflowing material at offset positions parallel to the minor axis. Figure 1 shows five slices parallel to the minor axis that are 1 kpc wide and offset at $+2, +1, 0, -1$, and -2 kpc along the midplane. Figure 8 shows the position velocity at each of those five positions. This figure clearly shows the H I velocity profile observed within ± 0.5 kpc of the minor axis (Center) is also seen in positions offset by as much as ± 2 kpc, albeit at somewhat lower intensity. A simple bicone with an opening angle of 8° (half width) would have no flux within about ± 7 kpc of the major axis in the offset positions at ± 2 kpc. While the intensity at these offset positions could be explained with a larger opening angle, a larger opening angle would also produce a much larger range of velocities at each position that would not be consistent with the observations.

We have consequently compared the data to a biconical frustum, rather than a simple bicone. Since a frustum is a conical shape with the top removed, we use this representation to model the origin of the outflow from a broader region of the disk than the single point of a cone. This shape is a better physical match to the spatial extent of the starburst, yet maintains the relatively narrow range of velocities observed further from the midplane (see Westmoquette et al. 2011, for the application of a frustum to NGC 253). We find that a frustum radius of 1 kpc at the midplane and an opening angle half width of 8° is a reasonable match to the data. The outline of this biconical frustum is shown in Figure 1, and position-velocity diagrams for this model are shown on the right side of Figure 8 at the same five offset positions as the data on the left. The choice of a 1 kpc radius at the midplane was motivated by the physical extent of the starburst region ($\sim$ 500 pc Förster Schreiber et al. 2003), but increased to provide a better match to the observed position-velocity diagrams. The velocity of the gas in the model was calculated at each point based on the radial distance from the center of the model. The velocity includes gravity and drag forces as in Figure 6, and was normalized such that the initial velocity of the gas matches the observed H I kinematics at 1.5 kpc from the midplane. The model does not include any material

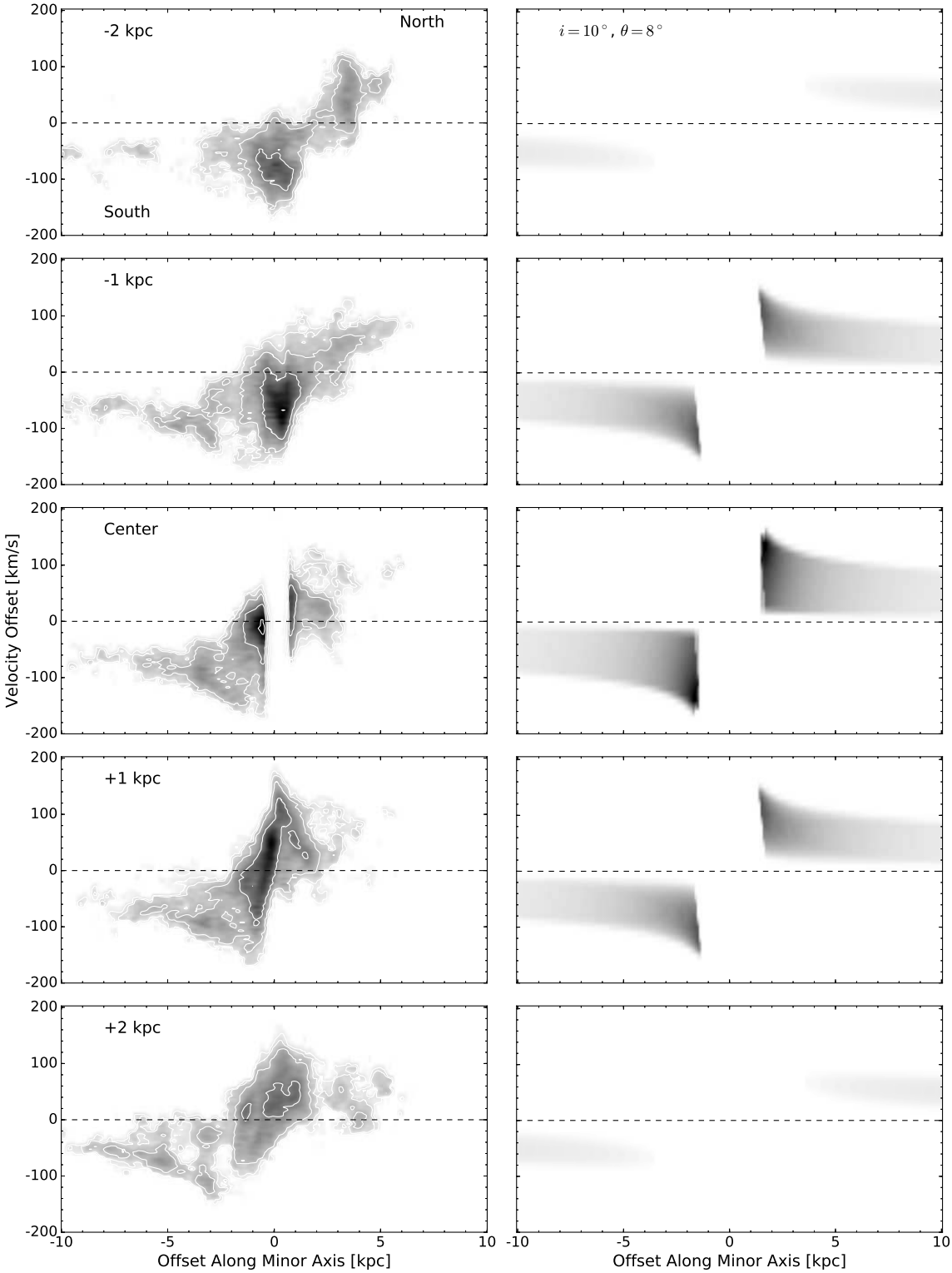

Figure 8. Five position-velocity diagrams offset for the observed H I gas (*left*) and a model biconical frustum outflow with an R=1kpc base on the major axis (*right*). Each row shows a 1 kpc wide slice perpendicular to the major axis. The H I data show the five positions marked in Figure 1, while the model shows the projected position-velocity diagram of a model filled biconical frustum with $i = 10°$ and opening angle $\theta = 8°$ (half width). The model includes both the gravitational deceleration and the drag force shown in Figure 6.

closer than 1.5 kpc from the center, as we assumed this region is substantially affected by the disk kinematics. The main disagreement between the model and data are that the model has a somewhat broader velocity distribution. This could be because our simple model adopts a uniformly filled frustum. The model would better match the data if the material were more concentrated on the symmetry axis, although physically that would be in conflict with the expected location of the hot wind. At larger distances, the density is assumed to decrease as $n \propto r^{-2}$.

4.3. *Alternative Scenarios*

It is also possible that the H I gas does not represent a continuous population of clouds flowing from the disk, but is instead partially or completely produced in situ. In this case, one potential origin is the dissociation of molecular gas. The molecular gas measurements from Leroy et al. (2015) within a few kpc of the midplane show similar kinematics as the atomic gas; however, the mass density of molecular gas is substantially lower than the H I off the midplane, and decreases much more rapidly with distance from M82. Deeper molecular gas observations would help to further test this hypothesis, along with calculations of the disassociation rate.

Another possibility is that the H I gas has radiatively cooled from the hot phase (Wang 1995a,b). The basic physical picture, which was developed in detail by Thompson et al. (2016), starts with cool gas clouds in the disk that are initially accelerated and shredded by the hot wind. The addition of this cloud material then increases the mass loading in the wind, and then this additional mass seeds thermal and radiative instabilities that precipitate cool gas out in the wind at larger distances. Following the wind model of Chevalier & Clegg (1985), a key dimensionless parameter is the mass loading parameter β, which describes the ratio of the mass outflow rate $\dot{M}_W$ in the wind to the star formation rate $\dot{M}_*$, that is $\dot{M}_W = \beta \dot{M}_*$. The radiative cooling requires some minimum mass loading due to the shape of the cooling function. For the case of M82, Hoopes et al. (2003) find weak evidence of cooling on large scales and Strickland & Heckman (2009) estimate a fairly low mass loading factor of $\beta = 0.2 - 0.5$ in the core, although the wind could be strongly mass loaded on larger scales. Thompson et al. (2016) therefore conclude that their model may not apply to M82, and note the additional complication of tidal material. The monotonic decline in the characteristic H I velocity with projected distance also does not seem consistent with radiative cooling because the velocity profile is inconsistent with the inferred velocity profile for the hot wind.

There is some phenomenological similarity between the velocity decrease in M82 on kpc scales and the ionized gas kinematics observed in nearby AGN on scales approximately an order of magnitude smaller. Studies of Seyfert galaxies such as NGC 1068 (Crenshaw & Kraemer 2000), Mrk 3 (Ruiz et al. 2001), and NGC 4151 (Das et al. 2005) are reasonably well matched with constant acceleration to 100-300 pc, followed by constant deceleration to the systemic velocity. Everett & Murray (2007) explored Parker wind models to explain the ~ 100 pc outflows in AGN, but found no self-consistent temperature profile that could explain all of the kinematics. They did note that the generic hydromagnetic winds explored by Matzner & McKee (1999) could explain the acceleration, and there are morphological similarities between that model and the observations of May & Steiner (2017), but it was not clear how to explain the deceleration without interaction with the surrounding medium.

5. SUMMARY

We have presented new VLA observations of the archetypical starburst galaxy M82, and combined them with earlier observations from the GBT. These data trace H I emission out to a projected distance of 10 kpc from the center of the galaxy with an angular resolution of $\approx 24''$. The velocity amplitude to both the North and South decreases from about $140 \rightarrow 50\,\mathrm{km\,s^{-1}}$ over a projected distance of $1.5 \rightarrow 5$ kpc from the midplane. The H I intensity is substantially greater to the South, where H I is detected out to a projected distance of 10 kpc.

These minor axis H I kinematics are not consistent with continual acceleration of the atomic gas from the midplane, nor with gas clouds launched on approximately ballistic trajectories. The H I gas is also three to four times slower than the inferred velocity of the hot superwind fluid traced by X-ray data, and therefore the H I gas is not consistent with material that has cooled from that phase. The H I kinematics are more similar to the molecular and warm, ionized gas that appears to trace the outer sheath of the superwind, although the warm, ionized gas has only been measured closer to the midplane.

We use a new mass model for M82 to demonstrate that an additional force is required to slow the H I gas, and that the observed velocity profile is consistent with drag caused by the ambient environment. This requires that the H I gas is spatially distinct from the hot superwind fluid, and is not just the cool tail of the temperature distribution. The magnitude of the required drag force constrains the density ratio of the clouds and ambient medium, as well as the typical cloud size, which could be tested with future, higher resolution H I observations. The high velocities and density contrast between the outflow and ambient medium would also produce shock-heated gas, which may contribute to the X-ray emission.

One alternate possibility is that the H I gas is not a continuous stream of material flowing from the disk, but rather is partially or completely produced in situ by dissociation of the molecular gas and/or adiabatic cooling of the warm, ionized gas that forms the interface between the superwind and the ambient medium. We disfavor this scenario because it does not naturally explain the systematic decrease in the H I velocities with distance from the midplane, at least not without a similar drag force on that material. There is also a very substantial velocity contrast between the superwind and the other phases. Deeper observations of the molecular and especially the warm ionized gas that extend further from the midplane would help reveal the extent to which that material shares the same kinematic profile as the H I gas.

A final possibility is that the H I along the minor axis is largely tidal debris viewed in projection near the minor axis. Such a superposition would be an unfortunate coincidence, and does not appear consistent with either the symmetric kinematic profile about the midplane or the larger-scale tidal streams of H I. Deeper, wider-field

H I observations, combined with new models of the interactions in the M81 group, could help to quantify the contribution of H I tidal streams, if any, to the H I observed along the minor axis.

The ultimate fate of the H I gas is unclear. Our detection of the velocity decrease along the minor axis, combined with our new mass model for M82, demonstrates that there is likely some additional drag force that slows the cold phase of the wind. This velocity decrease lowers the wind speed to be comparable to the escape velocity from the halo, and thus the ultimate fate of the gas could be fallback onto the disk in a cold fountain on ~ 100 Myr timescales, long-term residence in the circumgalactic medium, or escape into the intergalactic medium. How the gas is distributed among these three scenarios depends on any additional drag forces on the wind at larger distances, details of the halo mass distribution, and the tidal field of the M81 group.

The National Radio Astronomy Observatory is a facility of the National Science Foundation operated under cooperative agreement by Associated Universities, Inc. We thank Todd Thompson for discussions of Galactic winds and outflows. We also thank Norm Murray for his helpful referee report. The work of PM is partially supported by the National Science Foundation under Grant 1615553 and by the Department of Energy under Grant de-sc0015525. The work of AKL is partially supported by the National Science Foundation under Grants No. 1615105, 1615109, and 1653300. ADB acknowledges support from the National Science Foundation grant AST-1412419.

Facilities: VLA, GBT.

REFERENCES

Amirkhanyan, A. S., Gagen-Torn, V. A., & Reshetnikov, V. P. 1982, Astrophysics, 18, 17
Andrews, B. H., & Thompson, T. A. 2011, ApJ, 727, 97
Appleton, P. N., Davies, R. D., & Stephenson, R. J. 1981, MNRAS, 195, 327
Axon, D. J., & Taylor, K. 1978, Nature, 274, 37
Bland, J., & Tully, B. 1988, Nature, 334, 43
Borthakur, S., Heckman, T., Strickland, D., Wild, V., & Schiminovich, D. 2013, ApJ, 768, 18
Bovy, J. 2015, ApJS, 216, 29
Chevalier, R. A., & Clegg, A. W. 1985, Nature, 317, 44
Chynoweth, K. M., Langston, G. I., Yun, M. S., et al. 2008, AJ, 135, 1983
Chynoweth, K. M., Langston, G. I., Holley-Bockelmann, K., & Lockman, F. J. 2009, AJ, 138, 287
Chynoweth, K. M., Langston, G. I., & Holley-Bockelmann, K. 2011, AJ, 141, 9
Coker, C. T., Thompson, T. A., & Martini, P. 2013, ApJ, 778, 79
Cottrell, G. A. 1977, MNRAS, 178, 577
Crenshaw, D. M., & Kraemer, S. B. 2000, ApJL, 532, L101
Das, V., Crenshaw, D. M., Hutchings, J. B., et al. 2005, AJ, 130, 945
Efstathiou, G. 2000, MNRAS, 317, 697
Engelbracht, C. W., Kundurthy, P., Gordon, K. D., et al. 2006, ApJL, 642, L127
Everett, J. E., & Murray, N. 2007, ApJ, 656, 93
Finlator, K., & Davé, R. 2008, MNRAS, 385, 2181
Freedman, W. L., Hughes, S. M., Madore, B. F., et al. 1994, ApJ, 427, 628
Förster Schreiber, N. M., Genzel, R., Lutz, D., Kunze, D., & Sternberg, A. 2001, ApJ, 552, 544
Förster Schreiber, N. M., Genzel, R., Lutz, D., & Sternberg, A. 2003, ApJ, 599, 193
Gerke, J. R., Kochanek, C. S., Prieto, J. L., Stanek, K. Z., & Macri, L. M. 2011, ApJ, 743, 176
Goetz, M., Downes, D., Greve, A., & McKeith, C. D. 1990, A&A, 240, 52
Greco, J. P., Martini, P., & Thompson, T. A. 2012, ApJ, 757, 24
Heckman, T. M., Armus, L., & Miley, G. K. 1990, ApJS, 74, 833
Heckman, T. M., Lehnert, M. D., Strickland, D. K., & Armus, L. 2000, ApJS, 129, 493
Hernquist, L. 1990, ApJ, 356, 359
Hoopes, C. G., Heckman, T. M., Strickland, D. K., & Howk, J. C. 2003, ApJL, 596, L175
Hunter, D. A., Ficut-Vicas, D., Ashley, T., et al. 2012, AJ, 144, 134
Ichikawa, T., Yanagisawa, K., Itoh, N., et al. 1995, AJ, 109, 2038
Langston, G., & Turner, B. 2007, ApJ, 658, 455
Leroy, A. K., Walter, F., Martini, P., et al. 2015, ApJ, 814, 83
Lynds, C. R., & Sandage, A. R. 1963, ApJ, 137, 1005
Matzner, C. D., & McKee, C. F. 1999, ApJL, 526, L109
May, D., & Steiner, J. E. 2017, MNRAS, 469, 994
McCourt, M., O'Leary, R. M., Madigan, A.-M., & Quataert, E. 2015, MNRAS, 449, 2
McKeith, C. D., Castles, J., Greve, A., & Downes, D. 1993, A&A, 272, 98
McKeith, C. D., Greve, A., Downes, D., & Prada, F. 1995, A&A, 293, 703
Miyamoto, M., & Nagai, R. 1975, PASJ, 27, 533
Murray, N., Quataert, E., & Thompson, T. A. 2005, ApJ, 618, 569
Murray, N., Quataert, E., & Thompson, T. A. 2010, ApJ, 709, 191
Navarro, J. F., Frenk, C. S., & White, S. D. M. 1996, ApJ, 462, 563
Oppenheimer, B. D., & Davé, R. 2008, MNRAS, 387, 577
Oehm, W., Thies, I., & Kroupa, P. 2017, MNRAS, 467, 273
Ott, J., Stilp, A. M., Warren, S. R., et al. 2012, AJ, 144, 123
Peeples, M. S., & Shankar, F. 2011, MNRAS, 417, 2962
Rieke, G. H., Loken, K., Rieke, M. J., & Tamblyn, P. 1993, ApJ, 412, 99
Roussel, H., Wilson, C. D., Vigroux, L., et al. 2010, A&A, 518, L66
Ruiz, J. R., Crenshaw, D. M., Kraemer, S. B., et al. 2001, AJ, 122, 2961
Salak, D., Nakai, N., Miyamoto, Y., Yamauchi, A., & Tsuru, T. G. 2013, PASJ, 65, 66
Scannapieco, E., & Brüggen, M. 2015, ApJ, 805, 158
Schaaf, R., Pietsch, W., Biermann, P. L., Kronberg, P. P., & Schmutzler, T. 1989, ApJ, 336, 722
Schneider, E. E., & Robertson, B. E. 2017, ApJ, 834, 144
Seaquist, E. R., & Clark, J. 2001, ApJ, 552, 133
Smith, R., Flynn, C., Candlish, G. N., Fellhauer, M., & Gibson, B. K. 2015, MNRAS, 448, 2934
Shopbell, P. L., & Bland-Hawthorn, J. 1998, ApJ, 493, 129
Sofue, Y., Reuter, H.-P., Krause, M., Wielebinski, R., & Nakai, N. 1992, ApJ, 395, 126
Strickland, D. K., & Stevens, I. R. 2000, MNRAS, 314, 511
Strickland, D. K., & Heckman, T. M. 2009, ApJ, 697, 2030
Telesco, C. M., Joy, M., Dietz, K., Decher, R., & Campins, H. 1991, ApJ, 369, 135
Thompson, T. A., Fabian, A. C., Quataert, E., & Murray, N. 2015, MNRAS, 449, 147
Thompson, T. A., & Krumholz, M. R. 2016, MNRAS, 455, 334
Thompson, T. A., Quataert, E., Zhang, D., & Weinberg, D. H. 2016, MNRAS, 455, 1830
van der Hulst, J. M. 1979, A&A, 75, 97
Veilleux, S., Cecil, G., & Bland-Hawthorn, J. 2005, ARA&A, 43, 769
Veilleux, S., Rupke, D. S. N., & Swaters, R. 2009, ApJL, 700, L149
Walter, F., Weiss, A., & Scoville, N. 2002, ApJL, 580, L21
Walter, F., Brinks, E., de Blok, W. J. G., et al. 2008, AJ, 136, 2563-2647
Wang, B. 1995, ApJL, 444, L17
Wang, B. 1995, ApJ, 444, 590
Werk, J. K., Prochaska, J. X., Cantalupo, S., et al. 2016, ApJ, 833, 54
Westmoquette, M. S., Gallagher, J. S., Smith, L. J., et al. 2009, ApJ, 706, 1571
Westmoquette, M. S., Smith, L. J., & Gallagher, J. S., III 2011, MNRAS, 414, 3719

Young, J. S., & Scoville, N. Z. 1984, ApJ, 287, 153
Yun, M. S., Ho, P. T. P., & Lo, K. Y. 1993, ApJL, 411, L17
Yun, M. S., Ho, P. T. P., & Lo, K. Y. 1994, Nature, 372, 530
Zhang, D., Davis, S. W., Jiang, Y.-F., & Stone, J. M. 2017, arXiv:1708.02946

Draft version February 9, 2018
Typeset using LaTeX **twocolumn** style in AASTeX61

THE DRAGONFLY NEARBY GALAXIES SURVEY. IV. A GIANT STELLAR DISK IN NGC 2841

Jielai Zhang (张洁莱),[1,2,3] Roberto Abraham,[1,2] Pieter van Dokkum,[4] Allison Merritt,[5] and Steven Janssens[1]

[1] *Department of Astronomy and Astrophysics, University of Toronto*
[2] *Dunlap Institute for Astronomy and Astrophysics*
[3] *Canadian Institute for Theoretical Astrophysics*
[4] *Department of Astronomy, Yale University*
[5] *Max Planck Institute For Astronomy*

ABSTRACT

Neutral gas is commonly believed to dominate over stars in the outskirts of galaxies, and investigations of the disk-halo interface are generally considered to be in the domain of radio astronomy. This may simply be a consequence of the fact that deep HI observations typically probe to a lower mass surface density than visible wavelength data. This paper presents low surface brightness optimized visible wavelength observations of the extreme outskirts of the nearby spiral galaxy NGC 2841. We report the discovery of an enormous low-surface brightness stellar disk in this object. When azimuthally averaged, the stellar disk can be traced out to a radius of ∼70 kpc (5 R_{25} or 23 inner disk scale lengths). The structure in the stellar disk traces the morphology of HI emission and extended UV emission. Contrary to expectations, the stellar mass surface density does not fall below that of the gas mass surface density at any radius. In fact, at all radii greater than ∼20 kpc, the ratio of the stellar to gas mass surface density is a constant 3:1. Beyond ∼30 kpc, the low surface brightness stellar disk begins to warp, which may be an indication of a physical connection between the outskirts of the galaxy and infall from the circumgalactic medium. A combination of stellar migration, accretion and in-situ star formation might be responsible for building up the outer stellar disk, but whatever mechanisms formed the outer disk must also explain the constant ratio between stellar and gas mass in the outskirts of this galaxy.

Keywords: galaxies: disks — galaxies: evolution — galaxies: formation — galaxies: individual (NGC 2841) — galaxies: stellar content — galaxies: structure

1. INTRODUCTION

The sizes of galaxy disks and the extent to which they have well-defined edges remain poorly understood. Galaxy sizes are often quantified using R_{25}, the isophotal radius corresponding to $B = 25$ mag arcsec^{-2}, but this is an arbitrary choice. In fact, the literature over the last three decades has produced conflicting views regarding whether there is a true physical edge to galactic stellar disks. Early studies seemed to show a truncation in the surface brightness profiles of disks at radii where star formation is no longer possible due to low gas density (van der Kruit & Searle 1982), but more recent investigations have found examples of galaxy disks where the visible wavelength profile is exponential all the way down to the detection threshold (Bland-Hawthorn et al. 2005; van Dokkum et al. 2014; Vlajic et al. 2011). There is considerable confusion in the literature regarding the relationship between the profile shape and the size of the disk. Most disks fall in one of three classes of surface brightness profile types (Pohlen & Trujillo 2006; Erwin et al. 2008): Type I (up-bending), Type II (down-bending) and Type III (purely exponential). The existence of Type II disks has been pointed to as evidence for physical truncation in disks. However, while the position of the inflection in the profile can certainly be used to define a physical scale for the disk, this scale may not have any relationship to the ultimate edge of the disk (Bland-Hawthorn et al. 2005; Pohlen & Trujillo 2006).

The common view in the literature is that the HI disks of galaxies are considerably larger than their stellar disks. This arises from the observation that HI emission extends much further in radius than the starlight detected in deep images (van der Kruit & Freeman 2011; Elmegreen & Hunter 2017). A rationale for this is the possible existence of a minimum gas density threshold for star formation (Fall & Efstathiou 1980; Kennicutt 1989), although this idea is challenged by the fact that extended UV (XUV) emission is seen in many disks at radii where the disks are known to be globally stable (Leroy et al. 2008). Studies suggest that large scale instability is decoupled from local instability, and the latter may be all that is required to trigger star formation. For example, a study by Dong et al. (2008) analyzed the Toomre stability of individual UV clumps in the outer disk of M83. They found that even though the outer disk is globally Toomre stable, individual UV clumps are consistent with being Toomre unstable. These authors also found that the relationship between gas density and the star-formation rate of the clumps follows a local Kennicutt-Schmidt law. In a related investigation, Bigiel et al. (2010) carried out a combined analysis of the HI and XUV disks of 22 galaxies and found no obvious gas surface density threshold below which star formation is cut off, suggesting that the Kennicutt-Schmidt law extends to arbitrarily low gas surface densities, but with a shallower slope.

On the basis of these considerations, it is far from clear that we have established the true sizes of galactic disks at any wavelength. Absent clear evidence for a physical truncation, the 'size' of a given disk depends mainly on the sensitivity of the observations. This basic fact applies to both the radio and the visible wavelength observations, and relative size comparisons which do not account for the sensitivity of the observations can be rather misleading. For example, it is commonly seen that the gas in galaxies extends much further in single dish observations than it does in interferometric observations, because single dish observations probe down to lower column densities (Koribalski 2016). At visible wavelengths, the faintest surface brightness probed by observations has been stalled at ~ 29.5 mag arcsec^{-2} for several decades (Abraham et al. 2017), with this surface brightness 'floor' set by systematic errors (Slater et al. 2009).

The Dragonfly Telephoto Array (Dragonfly for short) addresses some of these systematic errors and is optimized for low surface brightness observations; see Abraham & van Dokkum (2014) for more details. Dragonfly has demonstrated the capability to routinely reach $\sim$32 mag arcsec^{-2} in azimuthally averaged profiles (van Dokkum et al. 2014; Merritt et al. 2016).

In this paper, we present ultra-deep visible wavelength observations taken with Dragonfly of the spiral galaxy NGC 2841. This galaxy is a particularly clean example of XUV emission in an isolated environment (Afanasiev & Sil'chenko 1999). It is notable for being the archetype for the flocculent class of spiral galaxies. The disk is globally Toomre-stable (Leroy et al. 2008) and it shows no evidence for grand design structure, although near-infrared observations do show some long dark spiral features in its interior (Block et al. 1996). Our aim is to determine if the stellar disk, as traced by visible wavelength light, extends at least as far as the neutral gas mapped by the THINGS survey (Walter et al. 2008), and the XUV emission mapped by GALEX (Thilker et al. 2007). Instead of just comparing sizes of disks in different wavelengths, we will compare mass surface densities up to the sensitivity limit of the respective data sets. Throughout the paper, we assume the distance to NGC 2841 is 14.1 Mpc (Leroy et al. 2008).

In §2 we describe our observations and the specialized reduction techniques we have adopted in order to obtain deep profiles with careful control of systematic errors.

Our results are presented in §3, and our findings are discussed in §4.

2. OBSERVATIONS AND DATA REDUCTION

Broadband images of NGC 2841 were obtained between 2013 and 2016 using Dragonfly as part of the Dragonfly Nearby Galaxy Survey (Merritt et al. 2016). Dragonfly is comprised of multiple lenses with their pointing offset from one another by a few arcminutes. Between 2013 and 2016, the number of lens and camera subsystems on the Array increased from 8 to 24. A total of 3351 ten-minute exposure images of NGC 2841 were obtained in Sloan g and r bands, distributed over the multiple cameras. Sky flats were taken daily at twilight and dawn. Data reduction was carried out using the Dragonfly Pipeline, full details for which can be found in Zhang et al. (2018 in prep). The full-width at half maximum (FWHM) of the final combined NGC 2841 image is 7 arcseconds.

The ultimate limiting factor in low surface brightness observations of nearby galaxies is the wide-angle point-spread function (PSF; Slater et al. 2009; Abraham & van Dokkum 2014; Sandin 2015). The largest-scale component of the PSF is the so-called 'aureole' (Racine 1996; King 1971). In conventional telescopes, the aureole is dominated by scattered light from internal optical components (Bernstein 2007). An important point emphasized in Zhang et al. (2018 in prep) is that this stellar aureole varies on a timescale of minutes, and so its origin is most likely atmospheric. DeVore et al. (2013) suggest that high-atmosphere aerosols (mainly ice crystals) are the culprit. An efficient way to detect the existence of atmospheric conditions which result in prominent stellar aureoles is to monitor the photometric zeropoints of individual exposures and identify those with deviations from the nominal zeropoint for a given camera at a given air mass. In our analysis of data from NGC 2841, exposures with a photometric zeropoint deviant from the nominal zeropoint by more than $\sim$0.1 mag were excluded from the final combined image. Out of the 3351 exposures obtained, 1034 were used. Most of the exposures excluded were taken in obviously marginal weather conditions (e.g., thin clouds). However, $\sim$25% of the exposures were identified as having wider-than-normal wide-angle PSFs only by using the procedure of monitoring the zeropoint values of the exposures.

Sky subtraction was done in two passes. In the first pass, a sky model was fit to the SExtractor (Bertin & Arnouts 1996) background map for each image and subtracted. Sky-subtracted frames were then used to create an average combined image (including both g and r-band data). SExtractor was run on this average combined image to produce a segmentation map. A mask was created by growing the segmentation map with settings to capture sources all the way out to their low surface brightness outer edges. In the second pass, sky models were fit to the SExtractor background map of non-sky-subtracted images again, but this time the mask was input into SExtractor for the creation of the background map. This ensures we do not over subtract the sky by fitting a sky model to ultra-faint galaxy light. After this careful sky subtraction procedure, there were no residual large-scale gradients visible to the eye in an image where non-sky pixels were masked. In order to measure any residual large-scale gradients not obvious by visual inspection, a third order polynomial was fit to a masked image. The peak to peak range of sky background model values are 0.05% the sky value for both the g and r-band images. This was measured on a 57 by 70 arcminute image of NGC 2841, with the long edge aligned in the north-south direction. It is important to note, however, that the regions responsible for the 0.05% variation in sky are all on the edges of the image, and do not overlap with NGC 2841.

The sky background and its error was determined by measuring the flux in elliptical annuli placed around NGC 2841 in each of the g and r-band Dragonfly images. Randomly placed elliptical annuli were used to sample the sky because the error in the sky value depends on the scale over which the sky is measured. For example, the variance in a sample of 10x10 pixel sky boxes will be different to a sample of 100x100 pixel sky boxes. The outer-most data points in the surface brightness profile are the most sensitive to the accuracy of the sky background measurement, therefore, that is the scale on which it is critical to know the sky background error. The shape of the sky sampling "box" was chosen to be an elliptical annulus because that most resembles the shape within which we have to determine the sky for the surface brightness profile. 1000 elliptical annuli were placed randomly in a 30 by 30 arcminute region around NGC 2841. The ellipticity and position angle of the elliptical annuli was fixed to be that of the largest surface brightness profile isophote. The annuli sizes were allowed to randomly vary but not below the size of the largest surface brightness profile isophote. In order to sample the local sky background values, the elliptical annuli were not allowed outside of a 30 by 30 arcminute region around NGC 2841. A mask was created so that no light from any sources was included in the determination of the sky level. First, the segmentation map produced by SExtractor (Bertin & Arnouts 1996) was grown to include the faint outer extents of the sources. For the brightest stars, as well as NGC 2841, the mask was

then grown further until no light was visible from these sources using the histogram stretch option in SAOImage DS9. The average and standard deviation of all the sky value measurements in the 1000 elliptical annuli were used to define the sky value and the error on the sky value, respectively. The mean sky surface brightnesses in g and r band were 21.1 mag arcsec^{-2} in g-band and 20.2 mag arcsec^{-2} in r band. The percentage errors on these sky levels were 0.01% and 0.007%, corresponding to limiting surface brightness levels of 30.9 and 30.6 mag arcsec^{-2} for the g and r-band images, respectively. The error in the sky value is the dominant source of uncertainty in the surface brightness profile at large radii.

The HI map used in comparisons below was taken from The HI Nearby Galaxy Survey (THINGS), made using data from the NRAO Very Large Array (VLA) (Walter et al. 2008). We obtained a far UV (FUV) map of NGC 2841 from the Galaxy Evolution Explorer (GALEX) Nearby Galaxies Survey (Gil de Paz et al. 2007) using the Detailed Anatomy of Galaxies (DAGAL) image repository (Knapen 2015).

3. ANALYSIS AND RESULTS

3.1. *Size of the stellar disk*

Our images of NGC 2841 in g-band and (g-r) color are shown in Figure 1, together with maps of FUV and HI emission. Figure 1's g-band image shows a giant disk extending as far as the HI and XUV emission. This disk is visible out to ∼60 kpc radius, which is ∼4 R_{25} (R_{25} = 14.2 kpc). To guide the eye, three pairs of arrows are marked in Figure 1, colored red, orange, and blue, corresponding to radii of 14.2 kpc (R_{25}), 30 kpc, 60 kpc respectively. The orange arrows (30 kpc) mark the edge of the well-studied inner disk of this commonly-observed galaxy (Block et al. 1996; Leroy et al. 2008; Sil'chenko & Afanasiev 2000; Afanasiev & Sil'chenko 1999). The disk beyond ∼30 kpc appears warped in all three wavelengths. Interestingly, there may be two distinct warped disks, which is most obvious in the (g-r) color and HI images. The peaks of the HI disk correspond to the peaks seen in the XUV and the visible wavelength data, which suggests that, at large radii, stars in this galaxy are mainly in a disk and are not part of a stellar halo.

In order to make g and r-band surface brightness profiles, stars and other sources were masked so that they did not contribute to the low surface brightness outer disk. The method used to create the mask for making the surface brightness profile was similar to that for measuring the sky level. The only difference is that NGC 2841 was removed from the segmentation map used to create the mask and the step to mask NGC 2841 by visual inspection in SAOImage DS9 was not applied. The mask for the bright star to the east of the galaxy (see Figure 1) overlaps with the central bulge of NGC 2841. Based on previous surface brightness profiles created of the inner disk, the bulge is no longer dominant beyond 60 arcseconds (Boroson 1981), so we can safely fit a pure exponential disk to the surface brightness profile beyond 200 arcseconds, and this is where the surface brightness profile in this paper begins. To create the profile, isophotes were fitted using the `iraf.stsdas.isophote.ellipse` routine (Jedrzejewski 1987) in PyRAF[1]. An initial x and y coordinate for the center of the galaxy was input, but the center, position angle and ellipticity of isophotes were allowed to vary. However, beyond a radius of ∼35 kpc, there is no longer enough signal to noise for the ellipse-fitting routine to allow these parameters to vary, and so the ellipse shape is fixed beyond that radius. The routine also extracts the average unmasked pixel value in each isophote. The g and r-band surface brightness profiles of NGC 2841 are shown in Figure 2, where the error bars include random as well as systematic sky-errors.

The visible light in the outskirts of NGC 2841 is clearly part of an extended disk, because the visible wavelength morphology of the galaxy traces the HI and UV disks. A 21-cm kinematic study of the galaxy shows there is a warp in the gas disk (Bosma 1978). Visually, g and r-band light beyond ∼30 kpc is dominated by a warped outer disk, aligned with the HI and the UV star forming disk. The warp is most obvious in the g-r color, and the HI images. As a further indicator of a stellar disk warp, the position angle of the fitted elliptical isophote jumps from -30 ±1.5 degrees clockwise from the y-axis within 30 kpc to -26.5 at 30 kpc. Note, however, that the position angle is not allowed to vary in the ellipse fitting routine beyond ∼35 kpc due to low signal to noise. Because the disk is warped, and because the surface brightness profile appears to up-bend, a two-exponential disk model is most appropriate and this was fit to the galaxy surface brightness profile. The inner and outer disks have scale lengths of 3.1±0.1 kpc and 13±3 kpc, respectively. The two-disk model is shown in Figure 2, with the solid grey line being the sum of the two components. Our measured surface brightness profile extends to ∼70 kpc, which is ∼23 inner disk scale lengths.

3.2. *Is the outer disk light contaminated by scatter from the wide-angle PSF?*

As described in the Introduction, the wide-angle point-spread function can play an important role in

[1] PyRAF are products of the Space Telescope Science Institute, which is operated by AURA for NASA

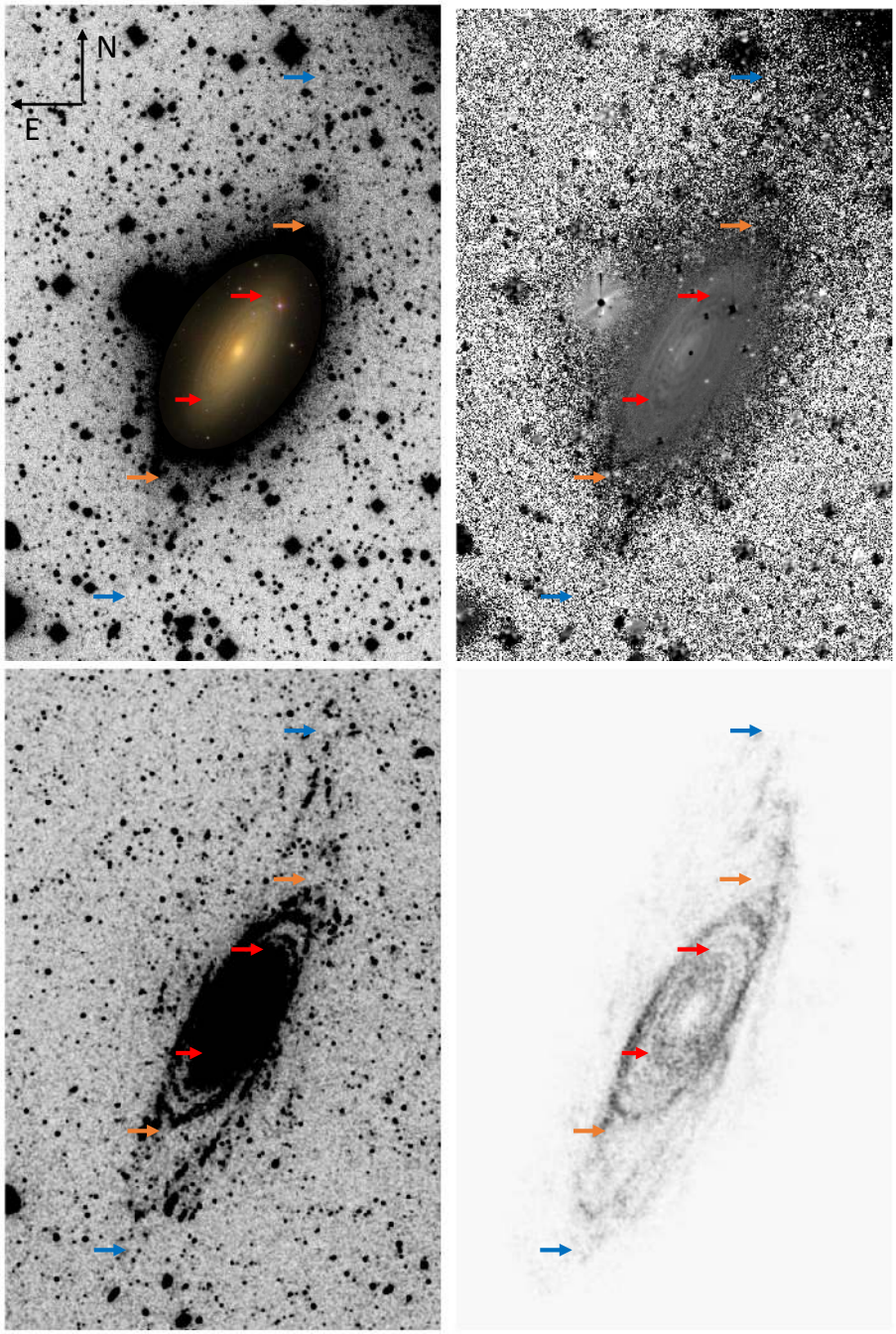

Figure 1. A panchromatic view of NGC 2841. Top left: Dragonfly g-band image. The color image embedded in the center was taken from the Sloan Digital Sky Survey data release 14 skyserver website (Abolfathi et al. 2017). Top right: Dragonfly (g-r) color image. Bottom left: GALEX FUV image. Bottom right: THINGS HI image. The arrows (red, orange, blue) in each image mark the following radii along the galaxy: R_{25} (14.2 kpc), 30 kpc, 60 kpc. The UV, HI gas and visible wavelength emission are traced out to similar radii in the disk of NGC 2841, with the peaks of the visible wavelength disk corresponding to the peaks of the HI and UV emission.

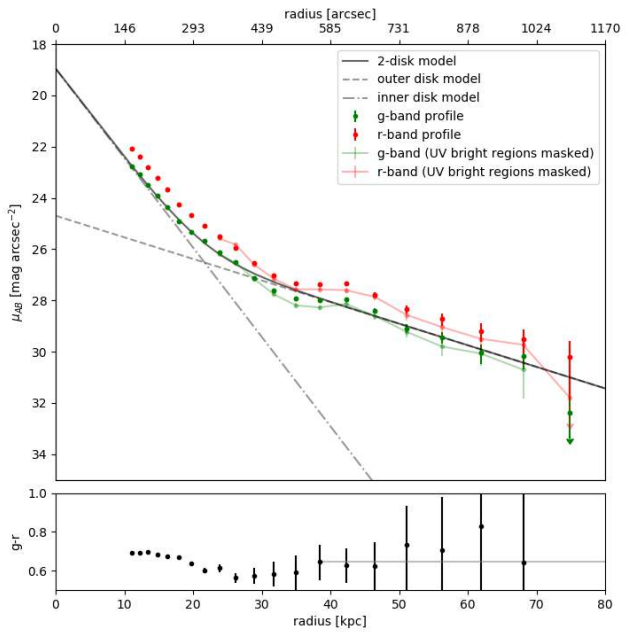

Figure 2. Top: Surface brightness profile of NGC 2841 in Sloan g and r-band. A 2-disk model is fit to the surface brightness profile. The inner and outer disks have disk scale lengths of 3.1±0.1 kpc and 13±3 kpc respectively. Plotted in a lighter shade of green and red with lines connecting the data points is the derived surface brightness profile after masking the UV bright regions. Bottom: The (g-r) color profile. The error bars in both plots include RMS and sky errors.

the measurement of profiles at very low surface brightness levels. Since the visibility of the stellar aureole varies as a function of atmospheric conditions, part of the data reduction pipeline for Dragonfly data rejects science exposures with zeropoints that deviate from a nominal zeropoint by more than ∼0.1 mag. This procedure removes the science exposures most contaminated by scattered light from the PSF. To test the significance of remaining contamination, we convolved a measured PSF with a one-dimensional model galaxy profile similar to NGC 2841 to observe the change in the surface brightness profile at large radii. A bulge central surface brightness of $\mu_0 = 20.1$ and bulge effective radius of $R_e = 0.94$ kpc was used (Boroson 1981) together with the two-disk model found in this paper.

The measured PSF has a radius of 10 arcmin and spans 18 magnitudes in surface brightness. The inner part of the PSF was measured using the brightest unsaturated star in the field. The outer part of the PSF was measured using the brightest saturated star in the field. The IRAF[2] routine `pradprof` was used to compute a radial profile around each star, which was then median binned in the radial direction to remove contamination by other sources. We note that this can only overestimate the PSF compared to the PSF that would be obtained without contamination from other sources.

The outcome of this exercise was that, because of the careful control of systematics in our experimental setup, the surface brightness profile of NGC 2841 remains unaffected by the wide-angle PSF down to at least $\mu = 32$ mag arcsec^{-2}.

3.3. *How is the extended light distributed?*

Is the extended visible wavelength emission from NGC 2841 simply the visible wavelength counterpart of the UV knots identified by GALEX? Or is this light truly distributed at all azimuthal angles around the disk?

To explore whether the visible wavelength light in the outer regions of NGC 2841 is entirely the visible wavelength emission from the UV knots identified by GALEX, we measured the g and r-band surface brightness profiles again after masking out the UV bright regions to see how much signal is left outside of the star forming regions. This surface brightness profile is shown also shown in Figure 2 as line-connected green and red data points for the g and r-band profiles, respectively. While the surface brightness profiles in both g and r-band have dimmed (by $\sim 20\%$ beyond 30 kpc) as a result of this masking, the overall shape and extent of the light profiles remain similar. We therefore conclude that the outer disk light is not simply the visible wavelength counterpart of the UV knots identified by GALEX.

A surface brightness profile averages light from all angles. This means in the low surface brightness galaxy outskirts the profile shape might be dominated by features in a small azimuthal wedge of the galaxy. To see if there is extended galaxy emission at all azimuthal angles, surface brightness profiles for azimuthal wedges were measured and plotted in Figure 3. While there is scatter in the profile in different azimuthal wedges, there is consistently light at all angles, lending further evidence to a smooth underlying disk that is the continuation of disk visible in Figure 1.

3.4. *Mass of stellar disk and comparison to the gas disk*

The stellar and the gas mass surface density profiles of NGC 2841 are shown in Figure 4. The stellar mass sur-

[2] IRAF is distributed by the National Optical Astronomy Observatory, which is operated by the Association of Universities for Research in Astronomy (AURA) under a cooperative agreement with the National Science Foundation.

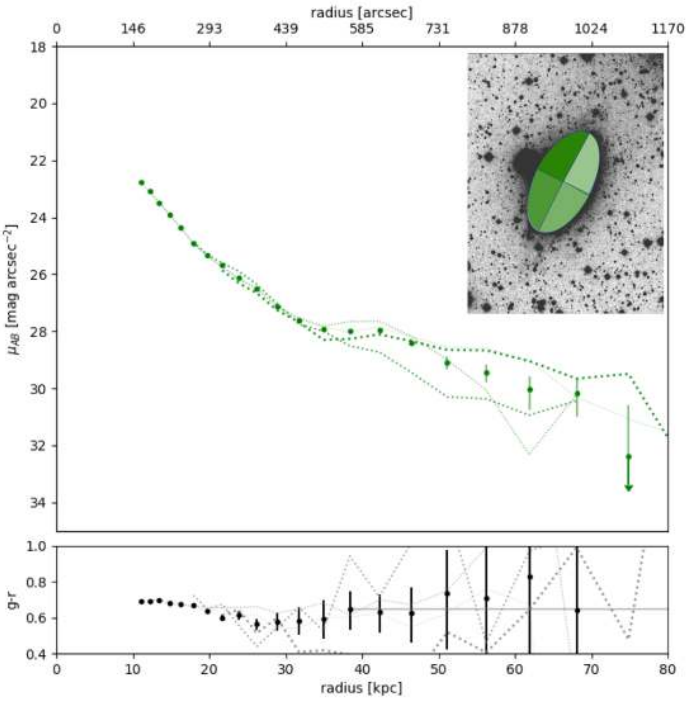

Figure 3. Top: The surface brightness profile of NGC 2841 in the Sloan g filter is shown again in green data points with error bars. Dotted green line profiles are azimuthal wedge g-band profiles. The darkest dotted line corresponds to the darkest green wedge shown in the top right-hand side image, with subsequent lighter shades of green corresponding to other lighter green wedges. Bottom: The (g-r) color profile is shown again in black. Dotted grey lines are the azimuthal wedge color profiles. The darkest grey dotted line corresponds to the darkest green wedge shown in the top right-hand side image, with subsequent lighter shades of grey corresponding to other lighter green wedges. The error bars in both plots include RMS and sky errors and are indicative of error bar size for all azimuthal wedge profiles.

face density was calculated in the same way as described in van Dokkum et al. (2014), using relations given in Bell & de Jong (2001):

$$\begin{aligned}\log_{10}(\rho[\mathrm{M\ pc^{-2}}]) = &-0.4(\mu_g[\mathrm{mag\ arcsec^{-2}}] - \mathrm{DM}) \\ &+1.49(g-r) \\ &+1.64 + \log_{10}(1/C^2) \end{aligned} \quad (1)$$

Using a distance of 14.1 Mpc (Leroy et al. 2008), DM = 30.7 is the distance modulus and C = 0.0684 is the conversion factor from arcsecond to kiloparsecs.

Since the mass density depends on color, we explored the impact of color on the inferred mass density using two different approaches. Densities obtained using both approaches are shown in Figure 4, as error bars and as shaded regions. In the first approach, we used the measured (g-r) color, and its uncertainty, which includes RMS and sky errors in both filters. The uncertainties in the mass measurements using this approach are displayed as error bars and include color and g-band RMS and systematic sky errors. In the outskirts, sky errors dominate. This is the most conservative indication of how well the stellar mass in the outskirts of NGC 2841 can be measured. The second approach, which is plotted as the shaded region in Figure 4, was to use the measured (g-r) color within 40 kpc, and a constant value of 0.65 beyond that. This choice of color is indicated by the grey horizontal line in the lower panel of Figure 2. Our rationale for adopting this constant color is because beyond 50 kpc the measurements of (g-r) color have very large uncertainties due to uncertainties in the sky level in both g and r-band. One can view the shaded region as a potential stellar mass surface density profile if the color in the outer disk remains at a constant 0.65 beyond 40 kpc. The errors indicated by the shaded region in the stellar mass surface density in Figure 4 include both RMS errors and systematic sky-errors in the g-band data.

The gas mass surface density was calculated using equation A1 from Leroy et al. (2008):

$$\Sigma_{\mathrm{gas}}[\mathrm{M_\odot pc^{-2}}] = 0.020 \cos i\ I_{21\mathrm{cm}}\ [\mathrm{K\ km\ s^{-1}}] \quad (2)$$

where $i = 1.29$ is the inclination in radians (Leroy et al. 2008). $I_{21\mathrm{cm}}$ is the 21 cm flux from the THINGS HI map. This gas mass equation includes a factor 1.36 to reflect the presence of helium. The gas mass surface density is plotted in green in Figure 4. Error bars shown account for the RMS scatter in each isophotal annulus. The shaded grey region is where the THINGS HI map and the GALEX FUV map has no detection at their respective sensitivity limits.

To better illustrate the relationship between stellar and gas mass, the ratio of the two is plotted in Figure 4 on the right-hand axis, in red. The ratio of stellar mass to gas mass remains remarkably constant (at 3:1) from just beyond ∼20 kpc, to the limit of the THINGS data. Remarkably, at the sensitivity limit of the THINGS survey and at the current depth of Dragonfly's observations of NGC 2841, there is no radius at which the mass surface density of HI gas begins to dominate over that of the stars. This has been measured out to 50 kpc, or 16 inner disk scale lengths. At radii greater than 50 kpc, the uncertainty in the sky levels of both the g and r Dragonfly images means the stellar mass is not measured with enough precision to conclude it is greater than the gas mass. However, the color in the disk beyond 50 kpc would have to be bluer than (g-r) = 0.3 in order for the stellar mass to drop below that of the gas mass.

3.5. *Timescales*

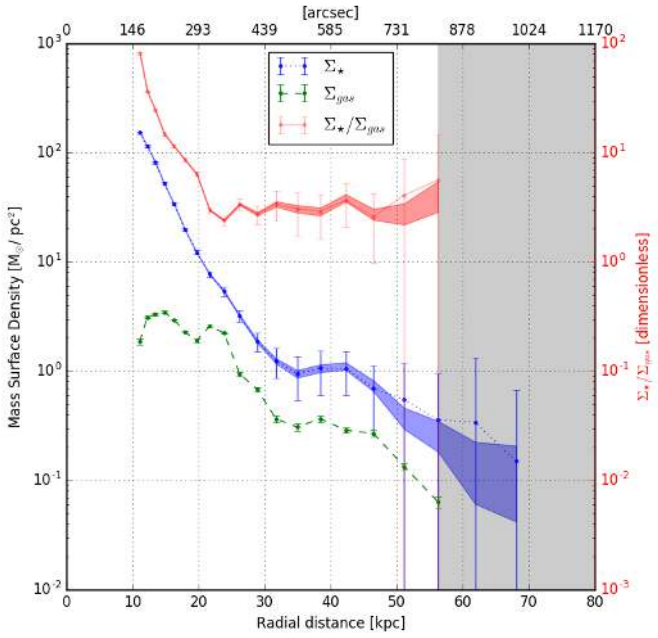

Figure 4. The mass surface density of stars and gas ($\Sigma_\star, \Sigma_{gas}$ [M$_\odot$ pc^{-2}]) and the ratio of the two ($\Sigma_\star/\Sigma_{gas}$) are plotted as a function of radius for NGC 2841. The error bars include the RMS uncertainty and the systematic error due to sky uncertainty in the g-band image and the (g-r) color used to calculate the stellar mass surface density. The shaded profiles assume that the color in the outer disk beyond 40 kpc is a constant. See the text for more details.

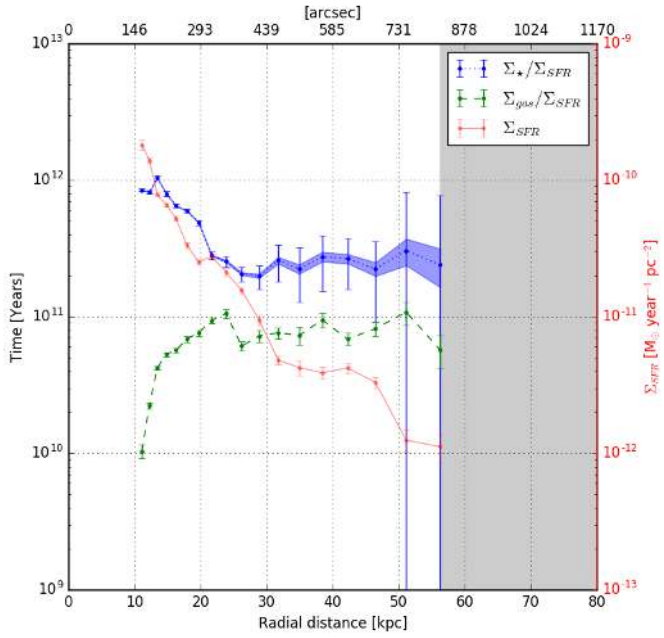

Figure 5. The stellar mass buildup time ($\Sigma_\star/\Sigma_{\rm SFR}$, blue) and gas depletion time ($\Sigma_{\rm gas}/\Sigma_{\rm SFR}$, green) and SFR surface density (black) are shown as a function of radius. The error bars include the RMS uncertainty in the HI, UV, g-band and r-band measurements, as well as the systematic error due to sky uncertainty in the g-band image and the (g-r) color used to calculate the stellar mass surface density.

The gas depletion time ($\Sigma_{\rm gas}/\Sigma_{\rm SFR}$) and the stellar mass buildup time ($\Sigma_\star/\Sigma_{\rm SFR}$) for NGC 2841 are plotted as a function of radius in Figure 5. The star formation rate (SFR) surface density used was obtained from the GALEX FUV image using equation 1 taken from Wilkins et al. (2012):

$$\Sigma_{\rm SFR}[{\rm M}_\odot\ {\rm year}^{-1}\ {\rm pc}^{-2}] = 10^{-34}\ {\rm L}_{\rm FUV}[{\rm ergs\ s}^{-1}\ {\rm Hz}_{-1}\ {\rm kpc}^{-2}]\ {\rm B}_{\rm FUV} \quad (3)$$

where B_{FUV} varies with the slope of the initial mass function (IMF). The value used here is 0.9 ± 0.18, based on the Kennicutt 1983 IMF (Kennicutt 1983). The SFR surface density is also plotted in Figure 5, on the right-hand axis, in red. The SFR and HI mass surface density error bars only includes the RMS scatter in each isophotal annulus. The error bars in $\Sigma_\star/\Sigma_{\rm SFR}$ include fractional errors in $\Sigma_\star$ and $\Sigma_{\rm SFR}$ added in quadrature. For $\Sigma_\star$, the error bars were calculated using two methods in the same way as in Figure 4: the error bars include the g and (g-r) errors while the shaded profile uses a (g-r) color model and only include the g-band errors.

The stellar mass buildup and gas depletion timescales remain constant from beyond ~20 kpc, the same region with a constant 3:1 ratio of stellar to gas mass surface density. The stellar mass buildup time in this region is 250 Gyr and the gas depletion time is on the order of 70 Gyr. Both of these timescales are much longer than the age of the Universe.

4. DISCUSSION

4.1. *The origin of outer disk stars*

The underlying stellar disk in NGC 2841 discovered using Dragonfly is gigantic, reaching beyond the size of the most sensitive HI and UV disk observations to ~70 kpc (~5 R_{25} or ~23 inner disk scale lengths). The surface brightness profile of the galaxy shows an upward bending break at 30 kpc, when the g-band surface brightness is ~28 mag arcsec^{-2}. Similar upward bending (Type I) surface brightness profiles are common at large radii, measured using a combination of photometry and star counts (Barker et al. 2009, 2012; Watkins et al. 2016). Of note is a multi-object spectroscopy study of stars in M31 by Ibata et al. (2005), which traced disk stars out to ~70 kpc. In NGC 2841, the position of the upbend corresponds to the start of a low surface brightness warp in the outer disk. This warp is visible in both g and r-band, THINGS HI and GALEX UV

images. One common assumption is that in the outer disks of galaxies, neutral gas is the dominant baryonic component based on the observation that in general HI disks extend much further than stellar disks (van der Kruit & Freeman 2011; Elmegreen & Hunter 2017). A comparison of the stellar mass to gas mass surface densities shows that for NGC 2841, there is no radius at which the mass surface density of gas begins to dominate over that of the stars. Beyond ∼20 kpc, NGC 2841 also has the interesting property that the stellar to gas mass surface density ratio is a constant 3:1.

A central question is: how did this giant stellar disk form? There are three main ways to populate the outer disk with stars: (1) stellar migration, (2) accretion of stars, and (3) in-situ star formation. Note that one mechanism does not preclude the others. We discuss the merits and weaknesses of each of these possibilities below.

(1) *Stellar Migration:* Sellwood & Binney (2002) showed that transient spiral arms in galaxy disks can scatter stars into orbits at different radii, but allow the stellar orbits to remain circular. Subsequent simulations by Roškar (Roškar et al. 2008a,b) showed that a downward bending (type II) surface brightness profile can be explained by a star formation threshold combined with stellar migration, which can move stars beyond their formation radius. There are several issues with appealing to stellar migration to populate the outer disk of NGC 2841. Firstly, it is unclear whether stellar migration can move so much mass to such a large range of radii beyond 30 kpc. Watkins et al. (2016) has similar concerns with appealing to stellar migration as a means of populating the outer disk of three nearby galaxies, where stars have to be moved several disk scale lengths beyond the extent of spiral arms. Secondly, stellar migration should not create an upwards bending surface brightness profile. Thirdly, the stars, as well as the gas, beyond 30 kpc are in a warped disk, and it is unclear how the migrated stars would end up in such a warped orbit. Perhaps the stars were displaced to large radius long ago and the warp was induced by a later interaction that warped both the stars and the gas.

(2) *Accretion:* In order for accreted stars to build up a co-planar disk, incoming stars need to have a narrow range in angular momenta that matches the existing disk, otherwise simulations show that the accreted stars tend to end up in a bulge or stellar halo (Toomre 1977; Schweizer 1990). In between these extremes lies infall with a slight mismatch in angular momentum, the result of which is a warped disk (Binney 1992). The warp in the disk of NGC 2841 beyond 30 kpc may hint at past accretion onto the disk with a slightly different angular momentum than that of the underlying stellar population. A quarter of a century ago, Binney (1992) noted presciently that: "...it is by no means inconceivable that warps are in direct physical contact with material that is only now joining the galactic system". Since our data for NGC241 extends out to ∼60 kpc, it is tempting to associate the outer warped disk in this system with material that has only recently infallen. If this interpretation is correct, we have reached far enough into the outskirts of NGC 2841 to be probing its circumgalactic environment, and may be witnessing a slightly more evolved part of the cool-flow driven galactic component referred to by Bland-Hawthorn et al. (2017) as the 'proto-disk'.

The total stellar mass in the disk beyond ∼30 kpc (where the warped disk starts to dominate) is $1.4\pm0.2\times10^8$ $M_\odot$. For comparison, the Small Magellanic Cloud has a stellar mass of $\sim7\times10^8$ $M_\odot$ (Dooley et al. 2017). The outer disk could potentially be formed by one or several small accretion events with the angular momenta of incoming dwarf galaxies almost aligned with that of NGC 2841.

The similarity in angular momenta required in this scenario may not be particularly improbable, since it seems that satellites of nearby galaxies can map out organized structures. Well-known examples include the Great Plane of Satellites around M31 (Ibata et al. 2013) and the Vast Polar Orbital structure around the Milky Way Galaxy (Pawlowski et al. 2015). One hypothesis for the existence of these planar structures is accretion along large scale filamentary structures (Ibata et al. 2013). If this is the case, the accreted dwarf galaxies could deposit their gas and stars onto the outer disk, possibly creating a constant stellar mass to gas mass ratio after a few rotations.

(3) *In-Situ Star Formation:* Stars in the outer disk of NGC 2841 clearly trace the distribution of the HI gas. This observation tends to favor a model in which the stars were formed in-situ. However, at the current SFR, it would take ∼200 Gyr to build up the outer disk stellar mass. On the other hand, the global star formation in the Universe was much higher in the past than today, peaking at redshifts of 2-3, with a SFR an order of magnitude greater than today (Madau & Dickinson 2014). At a star-formation rate that is 10 times that of the current SFR in NGC 2841, it would take ∼15 Gyr to build up the outer disk stellar mass. This is only slightly longer than a Hubble time, so such a scenario could be made to work. If in-situ star formation is responsible, then it begs the question of how the outer disk achieved such high levels of star formation in the past. The entire disk is currently Toomre stable and star formation is occurring in UV knots. It is possible

the gas density in the outer disk was higher in the past, but this may not be enough to stimulate sufficient star formation. Cormier et al. (2016) compared a sample of HI-rich galaxies to a control sample and showed that there is no increase in molecular gas mass or SFR in the outer disk in the HI rich sample. The difference was that the HI rich sample was able to able to sustain star formation in the outer disk for a longer period of time. Other studies support this by showing that gas depletion takes longer than a Hubble time and that SFRs and the Toomre stability parameter are not correlated (Bigiel et al. 2010). Semenov et al. (2017) carried out simulations that suggest global gas depletion times are long because only a small fraction of gas is converted into stars before star-forming regions are disrupted. Therefore, gas has to cycle in and out of the star-forming state many times before being turned into stars.

None of the mechanisms described above strike us as unreasonable, so perhaps the most likely scenario is that the outer disk of NGC 2841 is being built up by a combination of multiple mechanisms. For example, cool flow infall of gas which somehow triggers in-situ star-formation. However, one then wonders how these mechanisms conspired together to result in a constant ratio between stellar and gas mass surface density beyond ∼20 kpc.

The present paper reports results for a single galaxy, NGC 2841, the results from which indicate that with experimental setups optimized for low surface brightness imaging, stellar disks can be probed out to radii where the disk starts to warp. This may be an indication we are seeing parts of the disk that encroach upon the circumgalactic medium. Future papers will carry out similar analyses on other galaxies in the Dragonfly Nearby Galaxies survey, four of which have accompanying THINGS HI data. If NGC 2841 is any guide, the key questions for understanding galactic outskirts must now include: what fraction of massive spirals contain enormous underlying stellar disks? Are these disks always more massive than gaseous disks revealed by HI imaging? Is the mass ratio of stars to gas a constant in the outer disk, as seen in NGC 2841? At ultra-low surface brightness levels, do stellar disks always trace HI, and are these disks always warped in a manner consistent with infall? Is the geometry of the warps correlated with the positions of companion galaxies, as would be expected if the warped disk is built up by infall, and companion galaxies trace dark matter filaments? This long list of questions befits the richness of the phenomena being revealed at low surface brightness levels in the outskirts of galaxies. In any case, it seems to us that the key to answering these questions is to approach them in the appropriate panchromatic context, focusing on comparisons of surface mass densities, and not just on arbitrary definitions of the 'sizes' of disks at various wavelengths.

5. ACKNOWLEDGEMENTS

We thank the anonymous referee for a thoughtful and constructive report, which improved the paper. Support from NSERC, NSF grants AST-1312376 and AST-1613582, and from the Dunlap Institute (funded by the David Dunlap Family) is gratefully acknowledged. We thank the staff at New Mexico Skies Observatory for their dedication and support. JZ thanks Rhea-Silvia Remus for useful discussions. Funding for the Sloan Digital Sky Survey IV has been provided by the Alfred P. Sloan Foundation, the U.S. Department of Energy Office of Science, and the Participating Institutions. SDSS-IV acknowledges support and resources from the Center for High-Performance Computing at the University of Utah. The SDSS web site is www.sdss.org.

REFERENCES

Abraham, R. G., et al. 2017, p333, Outskirts of Galaxies, ed. Knapen, J. H. et al. 2017, Springer International Publishing, Cham, Switzerland

Abraham, R. G., & van Dokkum, P. G. 2014, PASP, 126, 55

Afanasiev, V. L., & Sil'chenko, O. K. 1999, AJ, 117, 1725

Barker, et al. 2009, 138, 1469

Barker, et al. 2012, 419, 1489

Bell, E. F., & de Jong, R. S. 2001, ApJ, 550, 212

Bernstein, R. 2007, ApJ, 666, 663

Bigiel, F., Leroy, A., Walter, F., et al. 2010, AJ, 140, 1194

Binney, J. 1992, ARA&A, 30, 51

Bland-Hawthorn, J., Vlajić, M., Freeman, K. C., & Draine, B. T. 2005, ApJ, 629, 239

Bland-Hawthorn, J., Maloney, P., Stephens, A., Zovaro, A. & Popping, A. 2017, ApJ, submitted

Block, D. L., Elmegreen, B. G., & Wainscoat, R. J. 1996, Nature, 381, 674

Boroson, T. 1981, ApJS, 46, 177

Bosma, A. 1978, Ph.D. Thesis

Cormier, D., Bigiel, F., Wang, J., et al. 2016, MNRAS, 463, 1724

DeVore, J. G., Kristl, J. A., & Rappaport, S. A. 2013, Journal of Geophysical Research (Atmospheres), 118, 5679

Knapen, J. H. 2015, IAU Symposium No. 321 (Toledo, Spain)

Dong, H., Calzetti, D., Regan, M., et al. 2008, AJ, 136, 479-497
Dooley, G. A., et al. 2017, MNRAS, 472, 1060
Elmegreen, B. G. & Hunter D. 2017, p115, Outskirts of Galaxies, ed. J.H. Knapen, et al. 2017, Springer International Publishing, Cham, Switzerland
Erwin, P., Pohlen, M., & Beckman, J. E. 2008, AJ, 135, 20
Fall, S. M., & Efstathiou, G. 1980, MNRAS, 193, 189
García-Ruiz, I., Sancisi, R., & Kuijken, K. 2002, A&A, 394, 769
Gil de Paz, A., Boissier, S., Madore, B. F., et al. 2007, ApJS, 173, 185
Ibata, et al. 2005, ApJ, 634, 287
Ibata, et al. 2013, Nature, 493, 62
Jedrzejewski, R. I. 1987, MNRAS, 226, 747
Kennicutt, R. C., Jr. 1983, ApJ, 272, 54
Kennicutt, R. C., Jr. 1989, ApJ, 344, 685
King, I. 1971, PASP, 83, 199K
Koribalski, B.S. 2016, IAU Symposium No. 321 (Toledo, Spain)
Leroy, A. K., Walter, F., Brinks, E., et al. 2008, AJ, 136, 2782
Madau, P., & Dickinson, M. 2014, ARA&A, 52, 415
Merritt, A., van Dokkum, P., Abraham, R., & Zhang, J. 2016, ApJ, 830, 62
Moffat, A.F.J. 1969, A&A, 3, 455
Pohlen, M., & Trujillo, I. 2006, A&A, 454, 759
Pawlowski, M.S., McGaugh1, S.S., & Jerjen, H. 2015, MNRAS, 453, 1047
Racine, R. 1996, PASP, 108, 699
Roškar, R., Debattista, V. P., Stinson, G. S., et al. 2008, ApJL, 675, L65
Roškar, R., Debattista, V. P., Quinn, T. R., Stinson, G. S., & Wadsley, J. 2008, ApJL, 684, L79
Sandin, C. 2015, A&A, 577, A106
Abolfathi, et al. 2017, ApJS, submitted
Sellwood, J. A., & Binney, J. J. 2002, MNRAS, 336, 785
Bertin, E. and Arnouts, S. 1996, A&AS, 117, 393-404
Schweizer, F. 1990, p60, In Dynamics and Interactions of Galaxies, ed. Wielen, R. 1990 Springer, New York
Semenov, V. A., Kravtsov, Andrey V., & Gnedin, N. Y. 2017, ApJ, 845, 133
Sil'chenko, O. K., & Afanasiev, V. L. 2000, A&A, 364, 479
Slater, C. T., Harding, P., & Mihos, J. C. 2009, PASP, 121, 1267
Thilker, D. A., Bianchi, L., Meurer, G., et al. 2007, ApJS, 173, 538
Toomre, A. 1977, p401, In The Evolution of Galaxies and Stellar Populations, ed. Tinsley, B. M., Larson, R. B. 1977
van der Kruit, P. C., & Freeman, K. C. 2011, ARA&A, 49, 301
van der Kruit, P. C., & Searle, L. 1982, A&A, 110, 61
van Dokkum, P. G., Abraham, R., & Merritt, A. 2014, ApJL, 782, L24
Vlajić, M., Bland-Hawthorn, J., & Freeman, K. C. 2011, ApJ, 732, 7
Walter, F., Brinks, E., de Blok, W. J. G., et al. 2008, AJ, 136, 2563-2647
Watkins, A. E., Mihos, J. C., & Harding, P. 2016, ApJ, 826, 59
Wilkins, S. M., Gonzalez-Perez, V., Lacey, C. G., & Baugh, C. M. 2012, MNRAS, 427, 1490
Zhang, J., et al. 2018, in preparation